Bi-electron bound states in single- and double-layer graphene nanostructures

Submitted by Lachlan Leslie Marnham
to the University of Exeter as a thesis
for the degree of Doctor of Philosophy in Physics
in June 2016.

I certify that all material in this thesis which is not my own work has been identified and that no material has previously been submitted and approved for the award of a degree by this or any other university.

Signature: .....

Abstract

The prototypical exciton model of two interacting Dirac particles in graphene was analysed by Sabio *et al*, Phys. Rev. B **81**, 045428 (2010), and it was found that in one of the electron-hole scattering channels the total kinetic energy vanishes, resulting in a singular behaviour [1]. We show that this singularity can be removed by extending the quasiparticle dispersion, thus breaking the symmetry between upper and lower Dirac cones. The dynamics of an electron-electron pair are then mapped onto that of a single particle with negative mass and anisotropic dispersion. We show that the interplay between dispersion and repulsive interaction can result in the formation of bound, Cooper-pair-like, metastable states in double-layered hybrid structures. We analyse these states by calculating their binding energies, decay rates into the free-electron continuum and semiclassical trajectories.

We also analyse the problem of bi-electron pairing with the inclusion of the two dominant many-body effects at zero temperature: screening of the Coulomb interaction by the Dirac sea, and reduction of the available phase space due to Pauli blocking of transitions into the states below the Fermi level. We show that these effects result in strong renormalization of the binding energy, but do not destroy the metastable states. Thus the binding energies are strongly dependent on the chemical potential owing to the combined effects of screening and Pauli blocking. Hence, the quasibound resonances can be tuned by electrostatic doping.

Acknowledgements

None of the work discussed in this thesis would have been possible without the tireless work of my PhD supervisor, Dr. Andrey Shytov, to whom I owe a great deal. In these past four years he has never failed to impress me with the depth of his intuition and the breadth of his knowledge. The ease with which he can answer my naïve questions about condensed matter theory with analogies to what seem, at first, unrelated fields of physics is simply breathtaking. I am also grateful for his mentorship and advice about soft issues like conference preparation, the politics of journal submission and how to navigate the job market.

Secondly, I thank my closest friends for sharing with me what have been the best four years of my life. I am particularly indebted to Aleksandra Kulawska, Charlie Nation, Dimitar Dimov, Ed Peck, Kate Ferguson, James Claughton and Bethany Stuart for their reassurance and advice in stressful times, their love and companionship in good times, and for showing up at my house with food when I ran out of money.

When one begins their first full-scale research project, it is easy to be overwhelmed. I thank my comrades from the 3$^{\text{rd}}$ floor PGR office, in particular Charles Downing, Alex Pearce, Tom Sturges, Claire Woollacott and Vasil Saroka, for sharing this experience with me, answering silly questions of university bureaucracy, pointing me in the direction of new or interesting papers and travelling to conferences with me.

While writing this thesis, I have benefited from some invaluable free software. I thank all of the people who worked to produce the following tools: LaTeX, Python, Inkscape, QtiPlot, Avogadro and GeoGebra.

Finally, I owe all of my accomplishments to the constant support and encouragement of my mother, father and brother, to whom I dedicate this work. I thank them for teaching me the importance of education, and for accepting that I needed to move to the other side of the world to pursue mine. I love them very much for it.

Contents

List of Figures

List of Tables

Introductory notes

We note that Chapters 2, 3 and 4 are based on the papers:

- L.L. Marnham and A.V. Shytov. Metastable electron-electron states in double-layer graphene structures. *Physical Review B*, 92:085409, 2015.
- L.L. Marnham and A.V. Shytov. Bielectrons in the Dirac sea in graphene: the role of many-body effects. arXiv:1512.02953v1, 2015.

Chapter 1

The electronic properties of graphene, an introduction

1.1 Crystal structure and reciprocal lattice

The carbon atom has 6 electrons, with a ground state arranged in the $1s^2 2s^2 2p^2$ configuration depicted in Fig. 1.1. There are two spherical $l = 0$ shells, $1s$ and $2s$, each of which hosts paired electrons. There are also three $l = 1$ orbitals, $2p_x$, $2p_y$ and $2p_z$ which are degenerate and mutually perpendicular. Two of these orbitals are occupied, and the electrons in them will have the same spin to minimize the electron-electron interaction. Naïvely, the carbon atom seems divalent, but when two of them are brought together, it is possible for their orbitals to hybridize in several different ways. One such example is sp^2 hybridization[1].

The $1s$ electrons are close to the nucleus and, therefore, do not contribute to bonding. The second shell ($n = 2$) can, however, restructure itself in such a way as to minimize the energy during bonding. The $2s$, $2p_x$ and $2p_y$ orbitals hybridize into three degenerate sp^2 orbitals (see the cartoon in Fig. 1.2) but the $2p_z$ orbital remains unchanged. The hybridized orbitals lie in plane, with angles of $\frac{2\pi}{3}$ between them to min-

[1]We will employ the language of chemistry here to give a qualitative picture. For a more rigorous treatment, see [2].

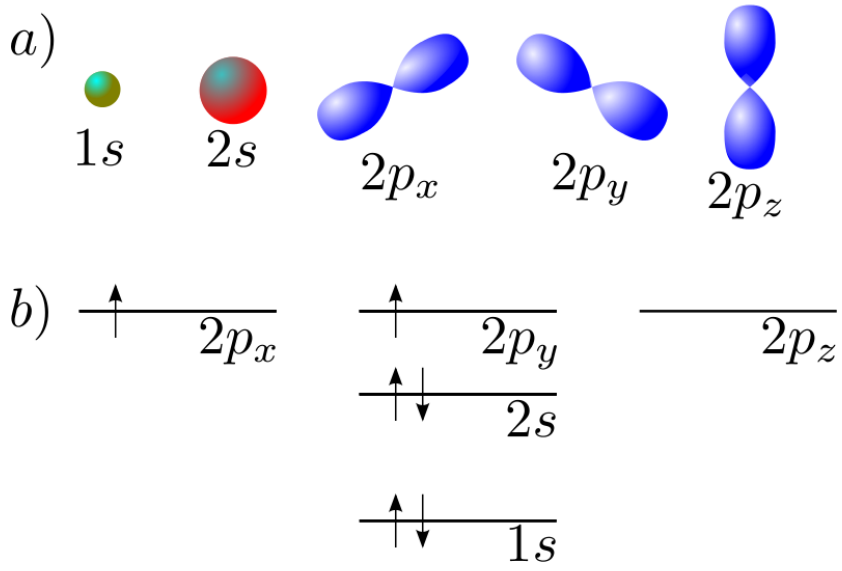

Figure 1.1: The atomic orbitals of carbon in the ground state; configuration $1s^2 2s^2 2p^2$. a) a cartoon of the orbitals, and b) the first few energy levels.

imize their energies. The remaining $2p_z$ orbital is perpendicular to this plane. When two carbon atoms come together, there will be an "end-on" overlap of their respective sp^2 orbitals resulting in a covalent σ bonding molecular orbital, with each atom contributing a single atomic orbital to the bond [3]. There will also be a "side-on" bonding of the atoms' respective $2p_z$ orbitals, thus forming the so-called π molecular orbital. The result of this process is shown in Fig. 1.3 . During this process σ^* and π^* antibonding orbitals are also formed which have higher energies than their bonding counterparts. Following the bonding of the two carbon atoms there will be four leftover sp^2 orbitals which will typically be used to bond to other atoms of another element to form a larger molecule (four hydrogens, in the case of ethylene, for example [3]). In the case of graphite, however, these remaining orbitals are used to bond to other carbon atoms, and so the process continues as a crystal is formed. In this case the process instead forms energy bands with the same titles: π, π^*,σ and σ^*. In the case of the two σ bands, there is a large energy gap and the electrons are tightly localized to maintain the bonds. In the case of the π bands, however, the electrons become dislocated from their atoms, leading to semimetallic behaviour.

If one takes these two bonded carbon atoms, and attempts to tile them into a crystal,

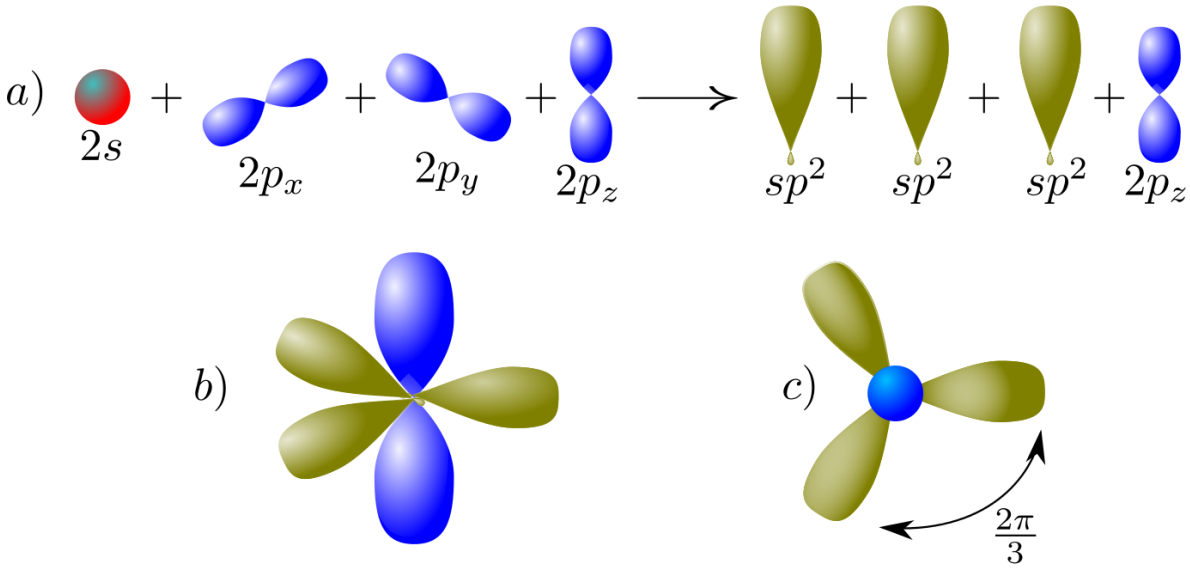

Figure 1.2: a) The sp^2-hybridization of the atomic orbitals of carbon. The result is three, degenerate sp^2 orbitals in-plane and a single $2p$ orbital which is perpendicular to that plane. b) Side view, and c) top view of a single sp^2-hybridized carbon atom (the nucleus and inner-most ($1s$) electronic orbital are not pictured).

the structure will be determined by the lengths of the σ bonds, and the angles between them. The result is the famous honeycomb lattice of graphene, as depicted in Fig. 1.4. Graphene is a two-dimensional (one atom thick) structure, which can be thought of as one of the constituent layers of graphite (the more traditional bulk material which can, equivalently, be thought of as a van der Waals superlattice of graphene layers). The crystal structure of bulk graphite was settled independently by Bernal [4] and Hassel [5] in 1924. Following its isolation, scanning tunnelling microscopy images [6] confirmed that graphene monolayers inherit the honeycomb structure of graphite. Unless otherwise stated, we will deal exclusively with the case of ideal graphene. The lattice symmetry can be broken, for example, by strain or the presence of adatoms, but such cases are outside the scope of this work.

At first glance, one might be tempted to define the generating vectors of the direct lattice as those which point from one atom to each of its nearest neighbours. The lattice is not, however, invariant under translations of these vectors: the honeycomb lattice is not Bravais. If we look at Fig. 1.4, and pretend for a moment that the "blue" atoms

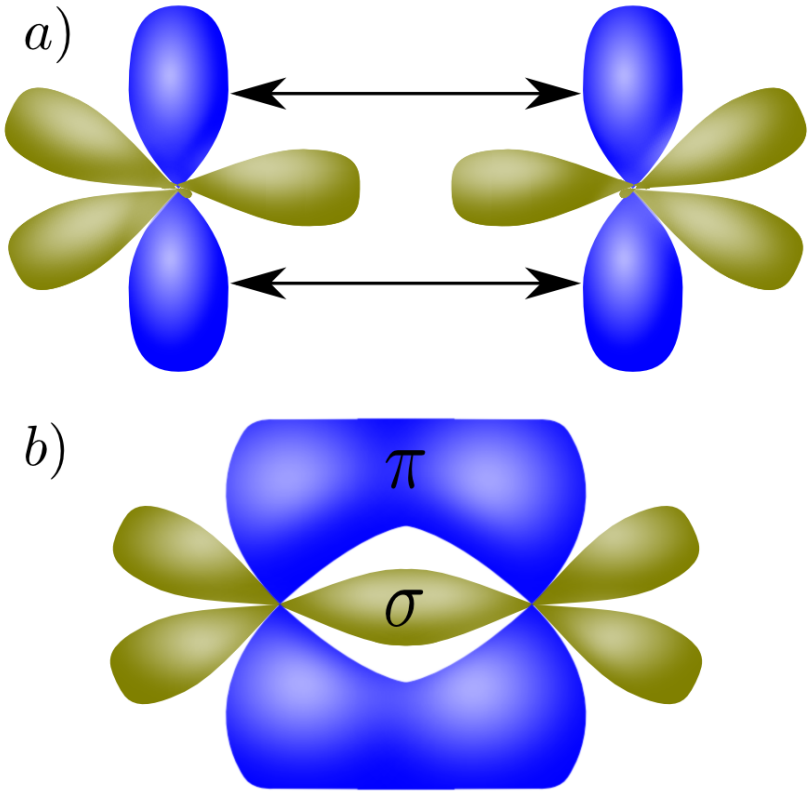

Figure 1.3: a) Before, and b) after sp^2-hybridized bonding of two carbon atoms. The π and σ molecular orbitals are labelled. The nuclei and innermost ($1s$) electronic orbitals are not pictured.

don't exist, we notice that the remaining "red" atoms form a hexagonal lattice, which *is* Bravais. It is therefore convenient to think of graphene as a hexagonal lattice with a two-atom basis. Although the two atoms in the unit cell are both carbon, and are physically equivalent but for their placements in the lattice, we think of them instead as defining two *sublattices* A and B. In Fig. 1.4, the sublattices are coloured differently to make this clear, and the unit cell is shown.

Every atom in graphene shares three σ-bonds with its three neighbours, all of which belong to the opposite sublattice. The primitive lattice vectors should therefore translate an atom in a given sublattice onto that same sublattice, and are given by

$$\boldsymbol{a}_{1,2} = \frac{a}{2}(3, \pm\sqrt{3}), \tag{1.1}$$

where $a = 1.42\text{Å}$ [4, 7] is the distance between neighbouring atoms. The nearest-

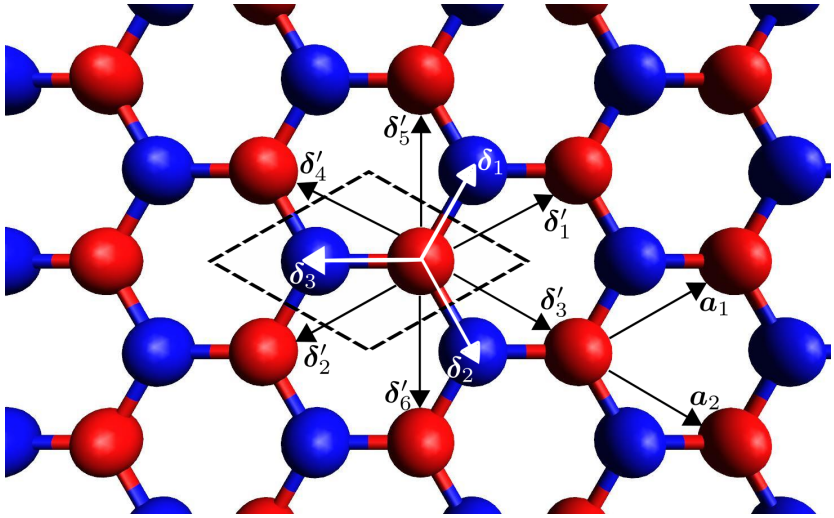

Figure 1.4: The crystal structure of graphene, with sublattices in different colours. The dashed lines enclose the unit cell, which contains a two-atom basis due to the sublattice structure. $\{\boldsymbol{a}_i\}_{i=1,2}$ denote the primitive lattice vectors, $\{\boldsymbol{\delta}_j\}_{j=1,2,3}$ are the nearest-neighbour vectors and $\{\boldsymbol{\delta}'_k\}_{k=1,\ldots,6}$ are the next-nearest-neighbour vectors.

neighbour ($\boldsymbol{\delta}_i$) and next-nearest-neighbour ($\boldsymbol{\delta}'_j$) vectors will, however, prove useful when we develop a tight-binding approach to the single-particle dynamics later. They are given by

$$\begin{aligned} \boldsymbol{\delta}_1 &= \tfrac{a}{2}\left(1,\sqrt{3}\right) & \boldsymbol{\delta}'_{1,2} &= \pm\tfrac{a}{2}\left(3,\sqrt{3}\right) \\ \boldsymbol{\delta}_2 &= \tfrac{a}{2}\left(1,-\sqrt{3}\right) \quad \text{and} & \boldsymbol{\delta}'_{3,4} &= \pm\tfrac{a}{2}\left(3,-\sqrt{3}\right) \\ \boldsymbol{\delta}_3 &= a\left(-1,0\right) & \boldsymbol{\delta}'_{5,6} &= \pm a\left(0,\sqrt{3}\right), \end{aligned} \tag{1.2}$$

all of which are depicted in Fig. 1.4.

The primitive vectors of the reciprocal lattice ($\boldsymbol{b}_i$) are orthogonal to those of the direct lattice by definition: $\boldsymbol{a}_i \cdot \boldsymbol{b}_j = 2\pi\delta_{ij}$. Solving the resulting linear equations gives

$$\boldsymbol{b}_1 = \frac{2\pi}{3a}(1,\sqrt{3}) \quad \text{and} \quad \boldsymbol{b}_2 = \frac{2\pi}{3a}(1,-\sqrt{3}). \tag{1.3}$$

Using these vectors the Brillouin zones can be constructed (the first few zones are given in Fig. 1.5. The first Brillouin zone has several important features, which will be made clear in the following section. Of particular interest are its corners, the so-called

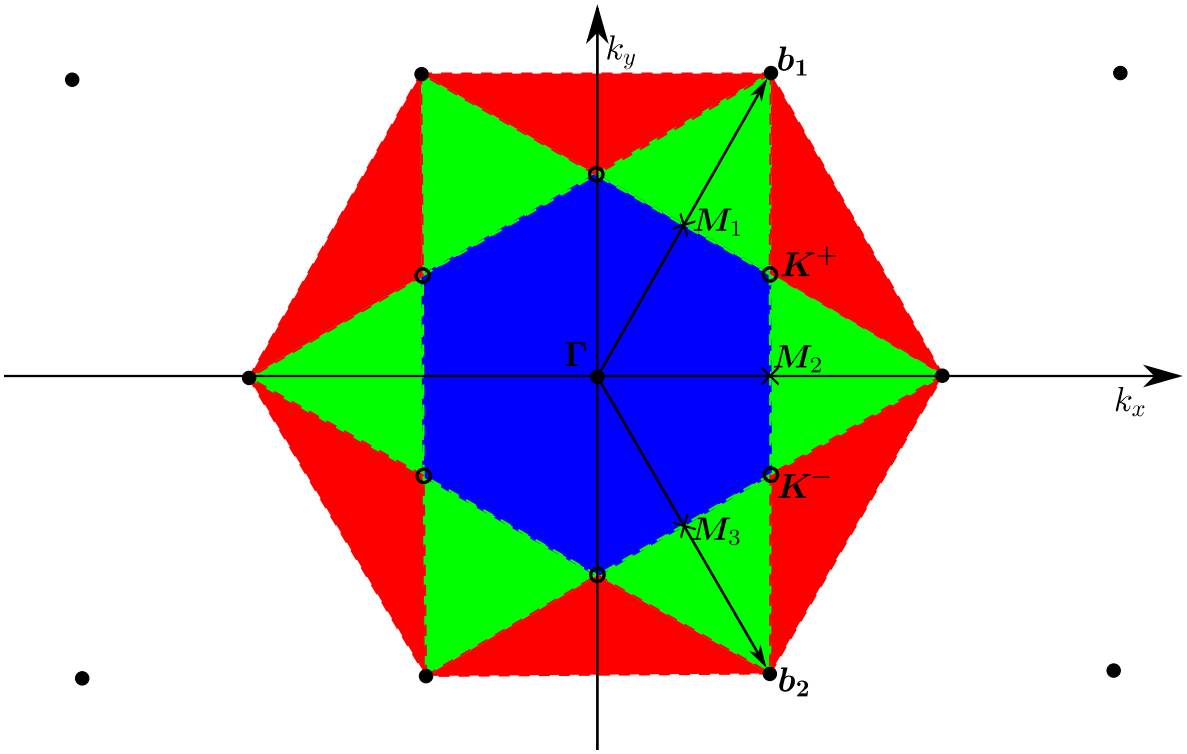

Figure 1.5: The 1st (blue), 2nd (green) and 3rd (red) Brillouin zones of graphene. The first zone has 6 corners (empty circles) which host Dirac valleys, two of which ($\boldsymbol{K}^{\pm}$) are inequivalent. The reciprocal lattice (filled circles) is generated by linear combinations of the form $\{n_1\boldsymbol{b}_1 + n_2\boldsymbol{b}_2 | n_1, n_2 \in \mathbb{Z}\}$.

Dirac points (or charge neutrality points, or valleys). Two[2] of the Dirac points are inequivalent:

$$\boldsymbol{K}^{\pm} = \frac{2\pi}{3a}(1, \pm\frac{1}{\sqrt{3}}), \tag{1.4}$$

and it will be these two which we refer to when we talk about "the Dirac points" from now on, unless stated otherwise.

1.2 Beyond parabolic dispersion in solids

Many of the interesting effects which are observed in graphene can be traced to its unusual band-structure. In the textbook example of free electrons in a solid, one treats

[2]The two inequivalent Dirac points are usually referred to as $\boldsymbol{K}, \boldsymbol{K}'$ or $\boldsymbol{K_1}, \boldsymbol{K_2}$ in the literature. We choose the notation $\boldsymbol{K}^+, \boldsymbol{K}^-$ as a way of making the equations in later chapters more clear.

a Hamiltonian of the following form:

$$\widehat{H} = \frac{\widehat{\boldsymbol{p}}^2}{2m^*}, \tag{1.5}$$

where $\widehat{\boldsymbol{p}}$ is the crystal momentum operator and the effective mass m^* encodes all of the information about the crystal potential, and can be extracted from the curvature of parabolic bands near the band edge. Spin is left out of the picture because it is not entangled with the motion of the particles. Instead, it enters the picture through the Zeeman energy.

An interesting and well-known example of coupling between the spin of a particle and its motion is provided by photons. Photons are spin-1 bosons which, unlike conventional spin-1 particles, have their spin pointing parallel or antiparallel to the direction of propagation. In the classical picture, these two spin projections correspond precisely to the left and right circular polarizations of light (as noted independently by Riemann, Majorana and Oppenheimer, see, e.g., Ref. [8]). When a beam of photons of random relative spin projection (i.e., 'unpolarized light') is incident on the interface between two dielectric media, a certain amount will be reflected and the remainder transmitted. When the angle between incident wavevector and surface normal is equal to the so-called Brewster angle, however, none of the light with electric field polarized in the plane of the wavevector and surface normal will be reflected. Thus, the interface, at the Brewster angle, filters by reflection the incident waves based on their respective polarization. Unlike the numerous common features shared by the different species of waves found in nature (interference, superposition, and so on), the Brewster angle is critically dependent on polarization. It does not occur in the longitudinal modes in gasses and liquids, for example.

One might ask if the spin of an electron can be coupled to its motion in a crystal, and try to find an analogue to the Brewster angle phenomenon in a band theory context. The heterojunction between a pair of semiconductors can host a two-dimensional electron gas (2DEG) with an electric field perpendicular to the plane of the junction. The

resulting spin-orbit interaction (SOI) is described by the Rashba Hamiltonian [9, 10], which takes the form:

$$\widehat{H}_R = \frac{\widehat{\boldsymbol{p}}^2}{2m^*} + \lambda \left[\boldsymbol{\sigma} \times \widehat{\boldsymbol{p}}\right] \cdot \hat{z}, \tag{1.6}$$

where λ is the spin-orbit coupling constant and $\boldsymbol{\sigma} = (\sigma_x, \sigma_y, \sigma_z)$ are the Pauli spin matrices:

$$\sigma_x = \begin{bmatrix} 0 & 1 \\ 1 & 0 \end{bmatrix}, \qquad \sigma_y = \begin{bmatrix} 0 & -i \\ i & 0 \end{bmatrix}, \qquad \sigma_z = \begin{bmatrix} 1 & 0 \\ 0 & -1 \end{bmatrix}. \tag{1.7}$$

This Hamiltonian lifts the spin degeneracy, leading to a momentum-dependent splitting of the energy bands: $E = p^2/2m^* \pm \lambda p$. In the conventional bulk metals and semiconductors, the spin-orbit coupling term is typically weak, comprising only a few percent of the total kinetic energy. Another class of systems in which the spin-orbit interaction plays a dominant role are the topological insulators (TI) [11, 12]. In the bulk of a 3 dimensional TI, the spin-orbit coupling leads to a mass term and resulting energy gap so that the bandstructure is that of a traditional insulator. On the surface, however, spin-orbital coupling dominates over the free-particle contribution to the kinetic energy, and the resulting metallic states are well described by a *massless* Dirac Hamiltonian of the form

$$\widehat{H}_S = v_F \left[\sigma_x \widehat{p}_x + \sigma_y \widehat{p}_y\right], \tag{1.8}$$

where v_F is the Fermi velocity. Further, there has been recent interest in the so-called Weyl semimetals, which are also topologically non-trivial but conducting in the bulk. Low-energy excitations are described by the Weyl Hamiltonian

$$\widehat{H}_W = v_F \boldsymbol{\sigma} \cdot \widehat{\boldsymbol{p}} \tag{1.9}$$

which acts on a pair of spinors of opposite chirality [13, 14].

Undoped graphene is another system in which the dynamics of low-energy excitations are not governed by Eq. (1.5): charge carriers are instead described by the Dirac equation in $2+1$ dimensions with vanishing mass term. Hence charge carriers in graphene are known as massless Dirac fermions, so that electrons in graphene behave as if they have no mass, leading to the observation of exotic "high-energy" phenomena in condensed matter experiments at low temperatures and even room temperature. One example is the phenomenon of Klein tunnelling [15], in which the transmission probability of an electron incident on a tunnelling barrier increases with increasing barrier height. Indeed, Klein tunnelling can be viewed as the electronic analogue of the Brewster angle phenomenon discussed above. Another is atomic collapse [16, 17], in which electron states spiral in toward the nucleus of a heavy atom, as opposed to the usual stable orbits which characterize the familiar Bohr atom.

In Section 1.4, we will show how such pseudo-relativistic physics arises from the single-particle Hamiltonian of graphene, by developing an effective theory which is valid in a small domain of the Brillouin zone near the Dirac points. But first we explain, in the next section, how the Hamiltonian can be derived across the whole Brillouin zone within the tight-binding approximation.

1.3 Tight binding description of the graphene band-structure

The entanglement in graphene is different to those other systems discussed above, which arise due to coupling of the momentum and the true spin. In graphene, the momentum is coupled to the *pseudospin*, an internal degree of freedom which arises due to the sublattice structure. To see how this arises, we derive an effective Hamiltonian within the tight-binding approximation (a calculation first performed by Wallace in 1947 [18]). Explaining the origin of the pseudospin term will be the object of this section, but what

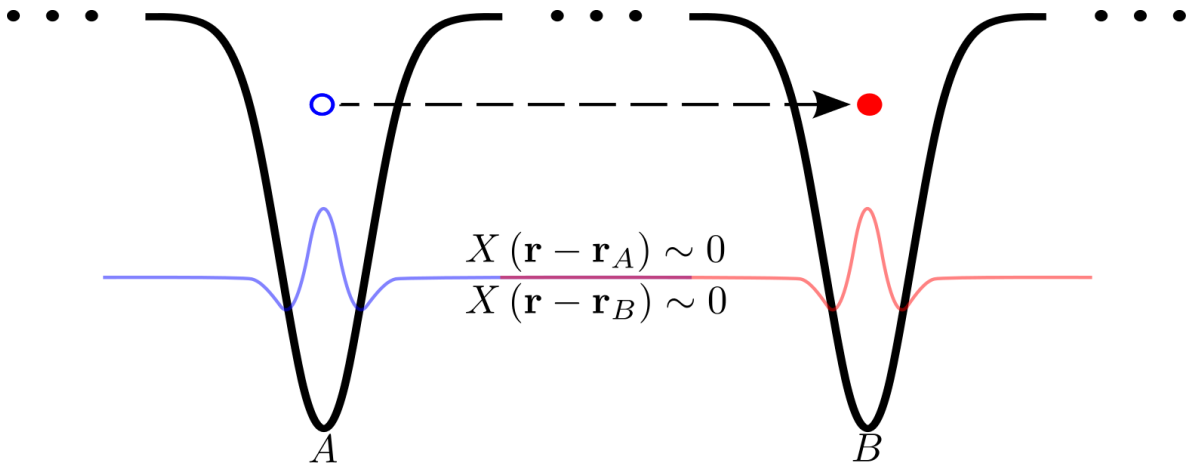

Figure 1.6: Schematic representation of tight binding. Electrons are able to hop from one atom to the next by tunnelling through the atoms' potential well. It is assumed that at any one time, the electron will be deep inside the well, so that its wavefunction decays quickly outside of the vicinity of the atom. Pictured is the shared double-well of two atoms, labelled A and B. Their respective wavefunctions, $X(\boldsymbol{r}-\boldsymbol{r}_A)$ and $X(\boldsymbol{r}-\boldsymbol{r}_B)$, decay quickly to zero in the region between the atoms.

will be really important for us in this thesis are the additional quadratic terms. We will derive the latter in Section 1.6.

The tight-binding approximation relies on the assumption that in the vicinity of any atom in the crystal, the crystal Hamiltonian may be approximated by the Hamiltonian of that atom were it to be isolated and that the relevant wavefunctions are localized (for a discussion see, for example, Ref. [19]). In view of the calculations to follow, we note that these assumptions are equivalent to the following, which we will use more explicitly:

- At any one time, the electron is highly localized to the vicinity of a lattice site and its wavefunction decays quickly elsewhere, and
- electrons are able to move within the lattice from one atom to the next by tunnelling.

These ideas are summarized in Fig. 1.6 for the case of a one-dimensional chain, but their extension to the geometry of graphene is straightforward.

We begin by defining the wavefunction of an electron in the $2p_z$ orbital of an isolated

carbon atom to be $X(\boldsymbol{r}-\boldsymbol{r}_i)$, where $\boldsymbol{r}_i$ labels the position of the i^{th} lattice site. Due to the translational symmetries of the individual sublattices, A and B, each sublattice must host a Bloch wavefunction of the form

$$\begin{aligned}\phi_A(\boldsymbol{r}) &= \frac{1}{\sqrt{N}}\sum_{\boldsymbol{r}_A} e^{i\boldsymbol{k}\cdot\boldsymbol{r}_A} X(\boldsymbol{r}-\boldsymbol{r}_A), \\ \phi_B(\boldsymbol{r}) &= \frac{1}{\sqrt{N}}\sum_{\boldsymbol{r}_B} e^{i\boldsymbol{k}\cdot\boldsymbol{r}_B} X(\boldsymbol{r}-\boldsymbol{r}_B).\end{aligned} \tag{1.10}$$

We say that when an electron is moving only on the sublattice A it is in the state $|A\rangle$, and when it is moving only on the sublattice B it is in the state $|B\rangle$. Under what circumstances are these two states orthogonal? Within the position representation, where the wavefunctions in Eq. (1.10) are given by $\phi_i(\boldsymbol{r}) = \langle \boldsymbol{r}|i\rangle$, we find that:

$$\begin{aligned}\langle A|B\rangle &= \int \phi_A^*(\boldsymbol{r})\phi_B(\boldsymbol{r})d\boldsymbol{r} \\ &= \frac{1}{N}\sum_{\boldsymbol{r}_A,\boldsymbol{r}_B} e^{\boldsymbol{k}\cdot(\boldsymbol{r}_B-\boldsymbol{r}_A)} \int X^*(\boldsymbol{r}-\boldsymbol{r}_A)X(\boldsymbol{r}-\boldsymbol{r}_B)d\boldsymbol{r} \\ &= 0,\end{aligned} \tag{1.11}$$

where the integral vanishes because we have assumed that the wavefunctions on neighbouring carbon atoms do not overlap. It therefore follows that the identity can be resolved in these two states:

$$\sum_{i=A,B} |i\rangle\langle i| = 1. \tag{1.12}$$

The assumptions of the tight-binding approximation have therefore led us to the definition of $\{|A\rangle, |B\rangle\}$ as a basis over which we can expand the states of electrons in graphene, and so we will look for solutions which are a linear combination of the

solutions for each sublattice,

$$|\psi\rangle = \sum_{i=A,B} = \langle i|\psi\rangle|i\rangle \,. \tag{1.13}$$

We insist that an electron in graphene must obey the following time-independent Schrödinger equation:

$$\widehat{H}\,|\psi\rangle = E\,|\psi\rangle\,, \tag{1.14}$$

and will use this, along with the tight binding approximation, to determine a matrix representation of the Hamiltonian $\widehat{H}$ within the aforementioned basis. We construct a system of two coupled equations by pre-multiplying by $\langle A|$ and $\langle B|$, and invoking Eq. (1.13), thus obtaining:

$$\begin{aligned} H_{AA}\psi_A + H_{AB}\psi_B &= E\psi_A, \\ H_{BA}\psi_A + H_{BB}\psi_B &= E\psi_B, \end{aligned} \tag{1.15}$$

where $\psi_i = \langle i|\psi\rangle$ is the probability amplitude for an electron in the energy eigenstate $|\psi\rangle$ to be found on the i^{th} sublattice following a measurement and $\langle i|\widehat{H}|j\rangle = H_{ij}$ is the matrix element of the Hamiltonian matrix between sublattices i, j. We have also used the result of Eq. (1.11). Therefore, within the sublattice space, we will represent the Hamiltonian by a 2×2 matrix, and the eigenfunctions will be represented by the 2 dimensional vector:

$$|\psi\rangle = \begin{bmatrix} \psi_A \\ \\ \psi_B \end{bmatrix} \tag{1.16}$$

For the Hamiltonian to be Hermitian, we require that its matrix representation be equal to its own conjugate transpose: $H_{AB} = H^*_{BA}$. Further, the sublattices are physically equivalent, so that $H_{AA} = H_{BB}$. This allows the simultaneous Eqs. (1.15)

to be solved for the energy:

$$E = H_{AA} \pm |H_{AB}|. \tag{1.17}$$

The on-diagonal elements represent hopping between atoms on the same sublattice:

$$\begin{aligned} H_{AA} &= \frac{1}{N} \sum_{\boldsymbol{r}_A, \boldsymbol{r}'_A} e^{-i\boldsymbol{k}\cdot(\boldsymbol{r}_A - \boldsymbol{r}'_A)} \int X^*(\boldsymbol{r} - \boldsymbol{r}_A) \widehat{H} X(\boldsymbol{r} - \boldsymbol{r}'_A) d\boldsymbol{r}, \\ &= E_0 + \frac{1}{N} \sum_{\boldsymbol{r}_A \neq \boldsymbol{r}'_A} e^{-i\boldsymbol{k}\cdot(\boldsymbol{r}_A - \boldsymbol{r}'_A)} \int X^*(\boldsymbol{r} - \boldsymbol{r}_A) \widehat{H} X(\boldsymbol{r} - \boldsymbol{r}'_A) d\boldsymbol{r}, \end{aligned} \tag{1.18}$$

where E_0 is the energy of an isolated carbon atom. Meanwhile, for the off-diagonal elements:

$$H_{AB} = \frac{1}{N} \sum_{\boldsymbol{r}_A, \boldsymbol{r}_B} e^{-i\boldsymbol{k}\cdot(\boldsymbol{r}_A - \boldsymbol{r}_B)} \int X^*(\boldsymbol{r} - \boldsymbol{r}_A) \widehat{H} X(\boldsymbol{r} - \boldsymbol{r}_B) d\boldsymbol{r}. \tag{1.19}$$

We don't have an analytic form for the wavefunctions $X(\boldsymbol{r})$, so they are absorbed into the so-called hopping parameters. We define the nearest-neighbour-hopping parameter, t, to be proportional to the transition matrix element of the Hamiltonian between the electronic wavefunctions of neighbouring atoms. It has the dimensions of energy, and can be interpreted as a kind of tunnelling amplitude between the atoms:

$$t = -\int X^*(\boldsymbol{r}) \widehat{H} X(\boldsymbol{r} - \boldsymbol{\delta}_i) d\boldsymbol{r}. \tag{1.20}$$

Likewise, the next-nearest-neighbour parameter characterizes hopping between nearby atoms on the same sublattice. It is given the definition:

$$t' = -\int X^*(\boldsymbol{r}) \widehat{H} X(\boldsymbol{r} + \boldsymbol{\delta}'_i) d\boldsymbol{r}. \tag{1.21}$$

We note that the form above was reached by assuming that the "red" atoms in Fig. 1.4 belong to sublattice A, so that the nearest-neighbour hopping vectors δ_i point from

an A atom to a B atom. Upon absorbing the above integrals, for which no analytical solution exists, into the definitions of the parameters t and t', Eqs. (1.18) and (1.19) take the following form:

$$H_{AA} = E_0 - t' \sum_{i=1}^{6} e^{-i\boldsymbol{k}\cdot\boldsymbol{\delta}_i'} = E_0 - t' g(\boldsymbol{k}), \qquad \text{and} \tag{1.22}$$

$$H_{AB} = -t \sum_{i=1}^{3} e^{i\boldsymbol{k}\cdot\boldsymbol{\delta}_i} = -t f(\boldsymbol{k}),$$

where we have defined

$$f(\boldsymbol{k}) = \sum_{i=1}^{3} e^{i\boldsymbol{k}\cdot\boldsymbol{\delta}_i}, \text{ and}$$

$$g(\boldsymbol{k}) = \sum_{i=1}^{6} e^{-i\boldsymbol{k}\cdot\boldsymbol{\delta}_i'}. \tag{1.23}$$

In principle, the Eqs. (1.22) could be written with many more terms to account for hopping between any pair of atoms in the direct lattice (although it would require more hopping parameters). Thankfully, the inclusion of nearest- and next-nearest-neighbour hopping terms is sufficient to capture the most important features of graphene's band structure. In fact, the contribution of same-sublattice hopping is so small at low energies that extracting a value of t' from experiments is non-trivial. Restricting ourselves to the matrix elements above, we are ready to write down a matrix representation of the tight-binding Hamiltonian of electrons in graphene:

$$\widehat{H} = \begin{bmatrix} E_0 - t' g(\boldsymbol{k}) & -t f(\boldsymbol{k}) \\ -t f(\boldsymbol{k})^* & E_0 - t' g(\boldsymbol{k}) \end{bmatrix}. \tag{1.24}$$

The vectors $\boldsymbol{\delta}_i$ and $\boldsymbol{\delta}'_i$ were given previously in Eq. (1.2) and upon their substitution into Eqs. (1.23) we obtain:

$$f(\boldsymbol{k}) = 2\exp\left(\frac{ik_x a}{2}\right)\cos\left(\frac{\sqrt{3}ak_y}{2}\right) + \exp\left(-ik_x a\right), \qquad \text{and}$$
$$g(\boldsymbol{k}) = 4\cos\left(\frac{3ak_x}{2}\right)\cos\left(\frac{\sqrt{3}ak_y}{2}\right) + 2\cos\left(\sqrt{3}ak_y\right). \tag{1.25}$$

The eigenvalues of the Hamiltonian in Eq. (1.24) are therefore given by $E_\pm = E_0 - t'g(\boldsymbol{k}) \pm t|f(\boldsymbol{k})|$, and this band structure has been plotted in Fig. 1.7 (here $\mathbf{k} = 0$ refers to the $\boldsymbol{\Gamma}$-point at the centre of the first Brillouin zone). Of particular interest is the behaviour of the bands near the Dirac points: $\boldsymbol{K}^+$ and $\boldsymbol{K}^-$ (see Eq. (1.4)). Here, we notice that $E_+ = E_-$, so that the single-particle band spectrum of graphene is gapless. We also note the unusual conical shape of the bands near these points, as shown in the inset.

So far our analysis has focussed on the geometry of the graphene crystal. The fact that graphene is composed of carbon atoms enters the discussion through the use of the wavefunctions $X(\boldsymbol{r})$ in the definitions of the hopping parameters in Eqs. (1.20) and (1.21). Since the eigenfunctions of the carbon atom cannot be calculated analytically, the values of t and t' are extracted from experimental results. For the purposes of this thesis, we will use the widely accepted result of $t = 2.8$eV [7, 20]. We note in passing, however, that the nearest-neighbour hopping parameter can be varied by substrate engineering. Two example studies have achieved $t = 2.16$eV and $t = 7.7$eV using copper foil [21] and quartz [20] substrates, respectively. Renormalization can also be achieved by doping close to the Dirac points, with one study reporting $t = 9.26$eV for carrier concentration $n < 10^{10}\text{cm}^{-2}$ [22]. The next-nearest-neighbour hopping parameter does not have an accepted value [7], and an important effect of this uncertainty will be discussed in the following chapters. *Ab initio* calculations [7,23] give the range $0.06\text{eV} \leq t' \leq 0.66\text{eV}$, while cyclotron resonance [24], quantum capacitance [25] and polarization-resolved magnetospectroscopy [26] measurements have produced $t' = 0.12$eV,0.3eV and

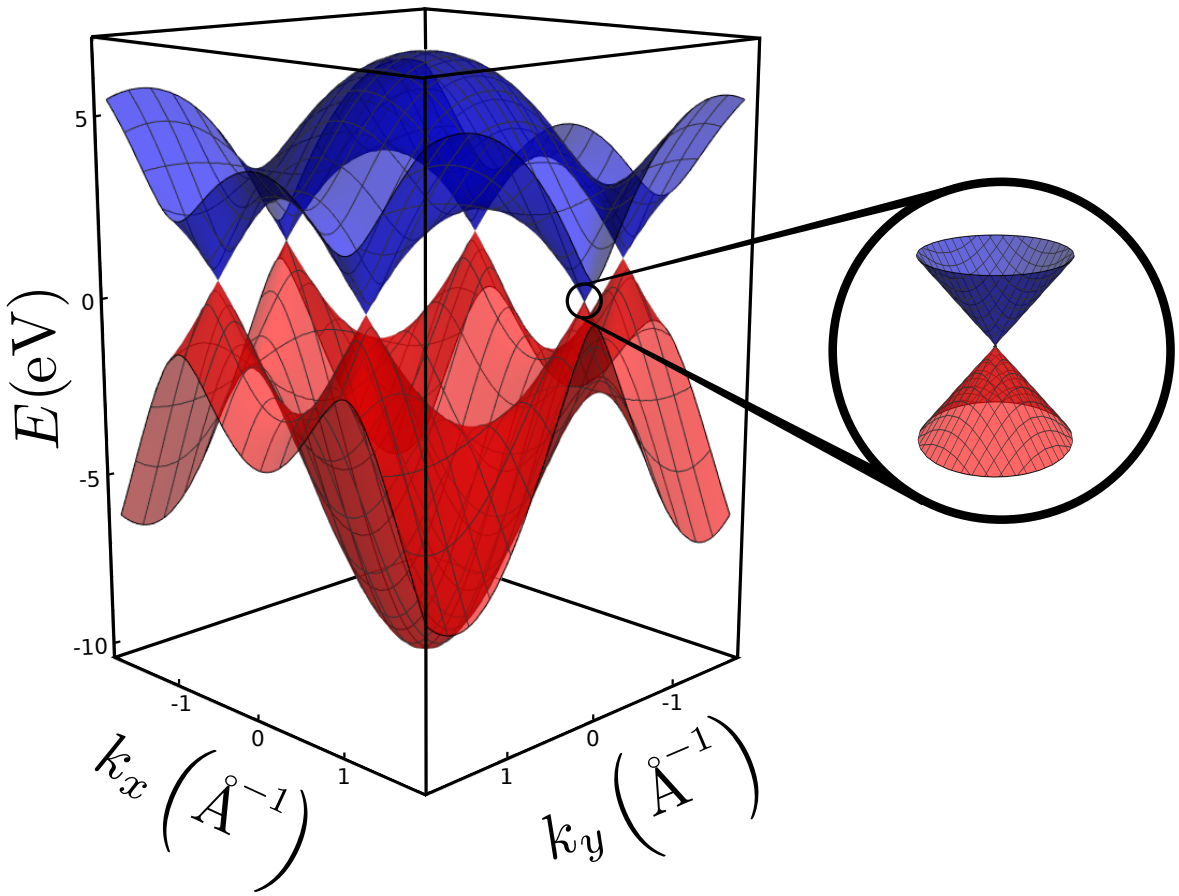

Figure 1.7: The energy spectrum of monolayer graphene. Inset is the conical structure of the bands near one of the Dirac points, which is a good approximation for energies of magnitude $|E| \lesssim 1\text{eV}$. In calculating the energies we have assumed $t = 2.8\text{eV}$ and $t' = 0.3\text{eV}$.

0.4eV respectively.

1.4 The low-energy limit: massless Dirac fermions in graphene

To clarify the emergence of a conical bandstructure (see Fig. 1.7) near the Dirac points, it is useful to look for an effective low-energy matrix representation of the Hamiltonian near the two Dirac points, which is achieved by expanding Eq. (1.24) near $\boldsymbol{K}^{\pm}$. For the time being it will suffice to take this to first order in the momentum as it is this regime for which graphene is most famous. We note in passing that much of the interesting

physics in the following chapters is due to the higher order terms in the Hamiltonian which break the symmetry between upper and lower bands near the Dirac points. Such terms are quadratic in the momentum, and arise due to trigonal warping of the bands and next-nearest-neighbour hopping. For further details, see Section 1.6.

Let us examine at the bandstructure near the $\boldsymbol{K}^{\pm}$-points. We define a small momentum $\boldsymbol{p}$, which is measured relative to the Dirac point, so that $\boldsymbol{p} = \hbar\boldsymbol{k} - \hbar\boldsymbol{K}^{\pm}$, and expand the Hamiltonian near $\boldsymbol{p} = 0$. To first order in $\boldsymbol{p}$, the Hamiltonian takes the form:

$$\begin{aligned}\widehat{H}_{\boldsymbol{K}^{\pm}} &= \begin{bmatrix} 3t' + E_0 & e^{\frac{i4\pi}{3}} v_F \left(ip_x \mp p_y\right) \\ e^{\frac{-i4\pi}{3}} v_F \left(-ip_x \mp p_y\right) & 3t' + E_0 \end{bmatrix} \\ &= \begin{bmatrix} 3t' + E_0 & e^{-\frac{i\pi}{6}} v_F p e^{\pm i\phi_{\boldsymbol{p}}} \\ e^{\frac{i\pi}{6}} v_F p e^{\mp i\phi_{\boldsymbol{p}}} & 3t' + E_0 \end{bmatrix}\end{aligned} \tag{1.26}$$

where $v_F = \frac{3at}{2\hbar} \sim 10^6 \mathrm{ms}^{-1}$ is the Fermi velocity of electrons in graphene, $p = \sqrt{p_x^2 + p_y^2}$ is the magnitude of the momentum and $\phi_{\boldsymbol{p}}$ is the momentum-space polar angle defined by $\tan(\phi_{\boldsymbol{p}}) = \frac{p_y}{p_x}$. The on-diagonal constant terms simply scale the zero-point of the energy, and we will absorb them into the eigenvalues in what follows.

The two Dirac points are separated by a momentum scale of the order of $1/a$, and it is therefore usually sufficient to take them as decoupled. We choose the basis $\psi = [\psi_{+,A}, \psi_{+,B}, \psi_{-,A}, \psi_{-,B}]^T$, in which the effective Hamiltonian takes the block-diagonal form: $\widehat{H} = \mathrm{diag}\left(\widehat{H}_{\boldsymbol{K}^+}, \widehat{H}_{\boldsymbol{K}^-}\right)$. Using the forms of Eq. (1.26), and transforming our coordinate system such that $\phi_{\boldsymbol{p}} \to -\phi_{\boldsymbol{p}} - \frac{\pi}{6}$, we obtain:

$$\widehat{H} = \begin{bmatrix} 0 & e^{i\frac{5\pi}{3}} v_F p e^{-i\phi_{\boldsymbol{p}}} & 0 & 0 \\ e^{-i\frac{5\pi}{3}} v_F p e^{i\phi_{\boldsymbol{p}}} & 0 & 0 & 0 \\ 0 & 0 & 0 & e^{i\frac{5\pi}{3}} v_F p e^{i\phi_{\boldsymbol{p}}} \\ 0 & 0 & e^{-i\frac{5\pi}{3}} v_F p e^{-i\phi_{\boldsymbol{p}}} & 0 \end{bmatrix} \tag{1.27}$$

The phase factors are due to our choice of basis, as is the seeming asymmetry between $\widehat{H}_{\boldsymbol{K}^+}$ and $\widehat{H}_{\boldsymbol{K}^-}$. Let us make the unitary transformation $\widehat{H} \to \widehat{U}\widehat{H}\widehat{U}^\dagger$, where:

$$\widehat{U} = \begin{bmatrix} 1 & 0 & 0 & 0 \\ 0 & e^{i\frac{5\pi}{3}} & 0 & 0 \\ 0 & 0 & 0 & e^{i\frac{5\pi}{3}} \\ 0 & 0 & 1 & 0 \end{bmatrix}. \tag{1.28}$$

In this new basis, which is given by $\psi = \left[\psi_{+,A}, e^{i\frac{5\pi}{3}}\psi_{+,B}, e^{i\frac{5\pi}{3}}\psi_{-,B}, \psi_{-,A}\right]^T$, the effective low-energy Hamiltonian is written:

$$\widehat{H} = \begin{bmatrix} 0 & v_F\left(p_x - ip_y\right) & 0 & 0 \\ v_F\left(p_x + ip_y\right) & 0 & 0 & 0 \\ 0 & 0 & 0 & v_F\left(p_x - ip_y\right) \\ 0 & 0 & v_F\left(p_x + ip_y\right) & 0 \end{bmatrix}. \tag{1.29}$$

To first order, the effective single-particle Hamiltonian is valley-independent, and takes the form:

$$\widehat{H}_{\boldsymbol{K}^\pm} = v_f \boldsymbol{\sigma} \cdot \boldsymbol{p}, \tag{1.30}$$

where $\boldsymbol{\sigma} = (\sigma_x, \sigma_y)$ is a vector of the Pauli spin matrices.

The energy eigenvalues of the Hamiltonian in Eq. (1.30) are given by

$$E_\pm = \pm v_F p, \tag{1.31}$$

irrespective of the valley in question, with corresponding eigenfunctions:

$$|\pm, \phi_{\boldsymbol{p}}\rangle = \frac{1}{\sqrt{2}} \begin{bmatrix} e^{-i\frac{\phi_{\boldsymbol{p}}}{2}} \\ \pm e^{i\frac{\phi_{\boldsymbol{p}}}{2}} \end{bmatrix}, \tag{1.32}$$

which is reminiscent of the mathematical formalism of spin in relativistic quantum mechanics. Indeed, when one studies the problem of a relativistic spin-$\frac{1}{2}$ particle, one treats the Dirac Hamiltonian in $2d$, which is given by

$$\widehat{H} = c\boldsymbol{\sigma} \cdot \boldsymbol{p} + m_0 c^2 \sigma_z \tag{1.33}$$

where m_0 is the rest mass and c is the speed of light in vacuum [27]. For $m_0 = 0$, the above operator is equivalent to the Hamiltonian of electrons in graphene, for which v_F plays the role of a reduced speed of light. For this reason, we say that electrons in graphene are "massless" or, more precisely, "behave *as if* they have zero rest mass".

In the Dirac equation, $\boldsymbol{\sigma}$ arises due to the fundamental spin of the electron (which is represented by the operator $\boldsymbol{S} = \frac{\hbar}{2}\boldsymbol{\sigma}$). In the preceding sections, however, we have not introduced the electron spin into our analysis at all. Instead, $\boldsymbol{\sigma}$ represents the so-called *pseudospin*, an internal degree of freedom reminiscent of the "real" spin, but which arises due to the two inequivalent sublattices discussed earlier (for a discussion, see Ref. [2]). We know that any spinor can be decomposed into a superposition of "spin up" (represented $|\uparrow\rangle$) and "spin down" (represented $|\downarrow\rangle$). Analogously, the Bloch eigenkets we used as our basis are pseudospinors, and it will prove convenient to label them as such in the following chapters:

$$\begin{aligned} |A\rangle &= \begin{bmatrix} 1 \\ 0 \end{bmatrix} \equiv |\uparrow\rangle\,, \qquad \text{and} \\ |B\rangle &= \begin{bmatrix} 0 \\ 1 \end{bmatrix} \equiv |\downarrow\rangle\,. \end{aligned} \tag{1.34}$$

This is true for the $\boldsymbol{K}^+$-point. For the $\boldsymbol{K}^-$ point we instead define $|A\rangle = |\downarrow\rangle$ and $|B\rangle = |\uparrow\rangle$. See Eq. (1.28) and the discussion thereafter.

Angle-resolved photoemission spectroscopy (ARPES) measurements have shown that the conical approximation is robust against changes in the size and shape of single-

grain graphene samples, as well as their orientation with respect to a substrate [21]. We note, however, that the same study showed significant renormalization of the Fermi velocity as a function of sample orientation, with results in the range $0.69 \leq v_F^*/v_F \leq 0.95$ where $v_F = 10^6 \mathrm{ms}^{-1}$.

1.5 Density of states

In this section we calculate another quantity which will prove useful in the chapters to follow: the density of states (DOS). In particular, we are interested in the number of energy states per unit energy per unit area, which is given by:

$$\mathcal{D}(E) = \frac{1}{\Omega} \sum_{\xi} \delta\left(E - E_{\xi}\right), \tag{1.35}$$

where Ω is the area of the sample and we enumerate over all possible states of the system. In particular, $\xi \equiv \{\boldsymbol{k}, \sigma, \tau, s\}$ is the set of all quantum numbers necessary to uniquely define a state in the system. We will restrict our analysis to the phase space near the Dirac points, where the band structure is linear. We know from the previous discussion that within the conical approximation states with different 'real' spin ($\sigma = \uparrow, \downarrow$) and states residing in the two different inequivalent valleys ($\tau = \pm$) have the same effective band-structure. Therefore, four of the terms in the summation Eq. (1.35) are equivalent, leading to a degeneracy of $N = N_\sigma \times N_\tau = 4$. States with different wavevector ($\boldsymbol{k}$) and band index ($s = \pm$) are not degenerate, however, which leads us to the expression:

$$\begin{aligned} \mathcal{D}(E) &= \frac{N}{\Omega} \sum_{\boldsymbol{k}} \left[\delta\left(E - E_+(\boldsymbol{k})\right) + \delta\left(E - E_-(\boldsymbol{k})\right)\right], \\ &= \frac{N}{2\pi} \left[\int_{k>0} \delta\left(E - \hbar v_F k\right) k dk + \int_{k>0} \delta\left(E + \hbar v_F k\right) k dk\right], \end{aligned} \tag{1.36}$$

where we have made the standard replacement $\sum_{\boldsymbol{k}} [\dots] \to \frac{\Omega}{(2\pi)^2} \int [\dots] \, d\boldsymbol{k}$ and carried out the integration over angles. Use of the identity $\delta(\alpha x) = \frac{1}{|\alpha|}\delta(x)$, brings Eq. (1.36) into a simple form:

$$\mathcal{D}(E) = \frac{N}{2\pi\hbar v_F} \left[\int_{k>0} \delta\left(k - \frac{E}{\hbar v_F}\right) k dk + \int_{k>0} \delta\left(k + \frac{E}{\hbar v_F}\right) k dk \right]. \tag{1.37}$$

Let us recall the definition of the Dirac delta function. If the energy E is *positive*, the second integral vanishes because the magnitude of the wavevector is positive definite. On the other hand, if E is *negative*, the first integral vanishes. We can summarize these cases with the aid of the Heaviside step function, $\Theta(\cdot)$, which is equal to unity for positive argument and vanishes elsewhere:

$$\mathcal{D}(E) = \frac{N}{2\pi(\hbar v_F)^2} \left(E\Theta(E) - E\Theta(-E) \right). \tag{1.38}$$

We can write Eq. (1.38) in a more elegant form:

$$\mathcal{D}(E) = \frac{N|E|}{2\pi(\hbar v_F)^2}. \tag{1.39}$$

We showed in the previous section that graphene has two bands, and is gapless. We have defined $E = 0$ to be at the Dirac point, so that the state of zero energy occurs at the point where the bands touch. Turning to Eq. (1.39), we see that $\mathcal{D}(E = 0) = 0$, so that there are no available single-particle states at the Dirac point. Undoped graphene has a full valence band and empty conduction band, so that all states above (below) the Dirac point are unoccupied (occupied). Thus, the DOS at the Fermi level is zero, and graphene is a semimetal.

The single-particle DOS is critically dependant on the dimensionality of the system and the dispersion of the particles within it. To understand this dependence, let us first motivate Eq. (1.39) with a simple scaling argument, which will give us the correct energy behaviour but not the numerical prefactors. The DOS is simply the number

of states per unit energy, per unit area. The bandstructure is a global quantity (it does not depend on the spatial coordinates of the particles) so the area must enter the calculation as a proportionality constant. Therefore, we will not consider it. The spin and valley indices label degenerate degrees of freedom, so those too are trivial. It is useful to consider the domain of k-space bounded by wavevectors k and $k + \Delta k$, which we denote $\Gamma = [k, k + \Delta k]$ as this leads to a convenient restatement of the density of energy states:

$$\mathcal{D}(E) \sim \frac{\text{Number of states within } \Gamma}{\text{Energy range corresponding to } \Gamma} \equiv \frac{N^{(d)}_{\Delta k}}{\Delta E_i}. \tag{1.40}$$

where d is the number of spatial dimensions and $i = l, p$ for linear and parabolic bands, respectively. The wavevector is a discrete quantum number, so that each state has allotted to it some non-vanishing area of k-space. Because the allowed wavevectors are uniformly spaced, that area is a constant for all of the states. Therefore, the number of states which occupy a wavevector domain Γ must scale like the k-space area of a ring of thickness Δk: $N^{(2)}_{\Delta k} \sim k\Delta k$. Because the bands are linear, the energy range corresponding to the domain Γ scales like $\Delta E_l \sim \Delta k$. Thus, from Eq. (1.36), we obtain

$$\mathcal{D}_{l,2}(E) \sim \frac{N^{(2)}_{\Delta k}}{\Delta E_l} \sim k \sim |E|, \tag{1.41}$$

which is the same dependence we found above in Eq. (1.39), where the subscript reminds us that we have dealt with a particle with linear dispersion in 2 dimensions.

Now let us apply this heuristic argument to some other examples. The energy range corresponding to an interval in k-space depends on the dispersion of the particles. At energies very close to $E = 0$, the energy of a particle is less sensitive to small changes in its velocity if it has a parabolic dispersion relation. What is the effect of this on the density of energy states? We saw before that if the bands are linear $\Delta E_l \sim \Delta k$. If the bands are parabolic, however, we instead obtain $\Delta E_p \sim k\Delta k$. Therefore, for a

parabolic particle in 2 dimensions, the density of energy states scales like:

$$\mathcal{D}_{p,2}(E) \sim \frac{N^{(2)}_{\Delta k}}{\Delta E_p} = \text{const.} \tag{1.42}$$

Indeed, the DOS in the $E \to 0$ limit is larger for parabolic bands (as compared to linear ones) regardless of dimensionality. Systems with linear dispersion simply do not host as many low-energy states as those systems with parabolic dispersion because changing the momentum of a particle increases its energy so quickly in that regime. The number of states in some interval of k-space depends on the dimensionality of the system: in 2 dimensions we were concerned with the number of states which occupied a ring of width Δk, but in 3 dimensions we are interested in the volume of a spherical shell of thickness Δk. This leads to the scaling $N^{(3)}_{\Delta k} \sim k^2 \Delta k$. Therefore, for Dirac particles in 3 dimensions, we obtain

$$\mathcal{D}_{l,3}(E) \sim \frac{N^{(3)}_{\Delta k}}{\Delta E_l} \sim k^2 \sim E^2, \tag{1.43}$$

which vanishes faster in the $E \to 0$ limit as does the case of graphene.

Finally, let us discuss the effects of non-linear terms in the bandstructure on the density of energy states. No analytical solution exists which is valid throughout the Brillouin zone when next-nearest-neighbour hopping is taken into account ($t' \neq 0$) [7]. In the absence of such a solution, we provide numerical calculations of the single particle DOS for $t' = 0$ as well as $t' \neq 0$ in Fig. 1.8. Away from charge neutrality, terms which are of higher than first order in the momentum increase the magnitude of the DOS, as compared to the conical approximation. This is the case within the interval $\kappa_- \leq E \leq \kappa_+$, where $\kappa_\pm = -t' \pm t$. At $E = \kappa_\pm$, the DOS exhibits Van Hove singularities which arise due to saddle points in the energy spectrum [28]. These saddle points occur at the so-called $\boldsymbol{M}$-points in graphene, which are situated between the Dirac points at

the Brillouin zone edges. Three of them are inequivalent, and located at:

$$\boldsymbol{M}_1 = \frac{\boldsymbol{b}_1}{2} \quad , \quad \boldsymbol{M}_2 = \frac{\boldsymbol{b}_1 + \boldsymbol{b}_2}{2} \quad , \quad \boldsymbol{M}_3 = \frac{\boldsymbol{b}_2}{2}. \tag{1.44}$$

It was shown by Van Hove [28] that, near $\kappa_\pm$, the DOS is logarithmically singular:

$$\mathcal{D}(E \to \kappa_\pm) \sim \log \left| \frac{1}{1 - \frac{E}{\kappa_\pm}} \right|, \tag{1.45}$$

the finite maxima in Fig. 1.8 are due to computational limitations.

Although the conical approximation, given in Eq. (1.39), underestimates the DOS, we note that it is of the correct order of magnitude in the low energy regime $E \lesssim 1\text{eV}$. Therefore, in the chapters that follow, we will use that quantity in equations which call for the density of energy states (e.g. the dielectric function) despite studying the effects of non-linear terms in the Hamiltonian. We will justify this in the following chapter, when we note that these terms play a crucial role in the kinetic energy of a pair of particles.

1.6 Trigonal warping and electron-hole asymmetry

Graphene has received considerable attention since its discovery due, in large part, to the massless nature of its electron states. This property has lead to the experimental realization of long-proposed relativistic phenomena, such as Klein tunnelling [15] and atomic collapse [16, 17]. Away from the Dirac points, however, the analogy to ultra-relativistic dynamics breaks down in graphene. Let us dwell briefly upon the *differences* between "Dirac particles" in graphene, and true relativistic particles in flat space-times.

A relativistic particle of rest mass m_0 and momentum $\boldsymbol{p}$ in free, flat space-time, has energies given by:

$$E_\pm = \pm\sqrt{m_0^2 c^4 + p^2 c^2}, \tag{1.46}$$

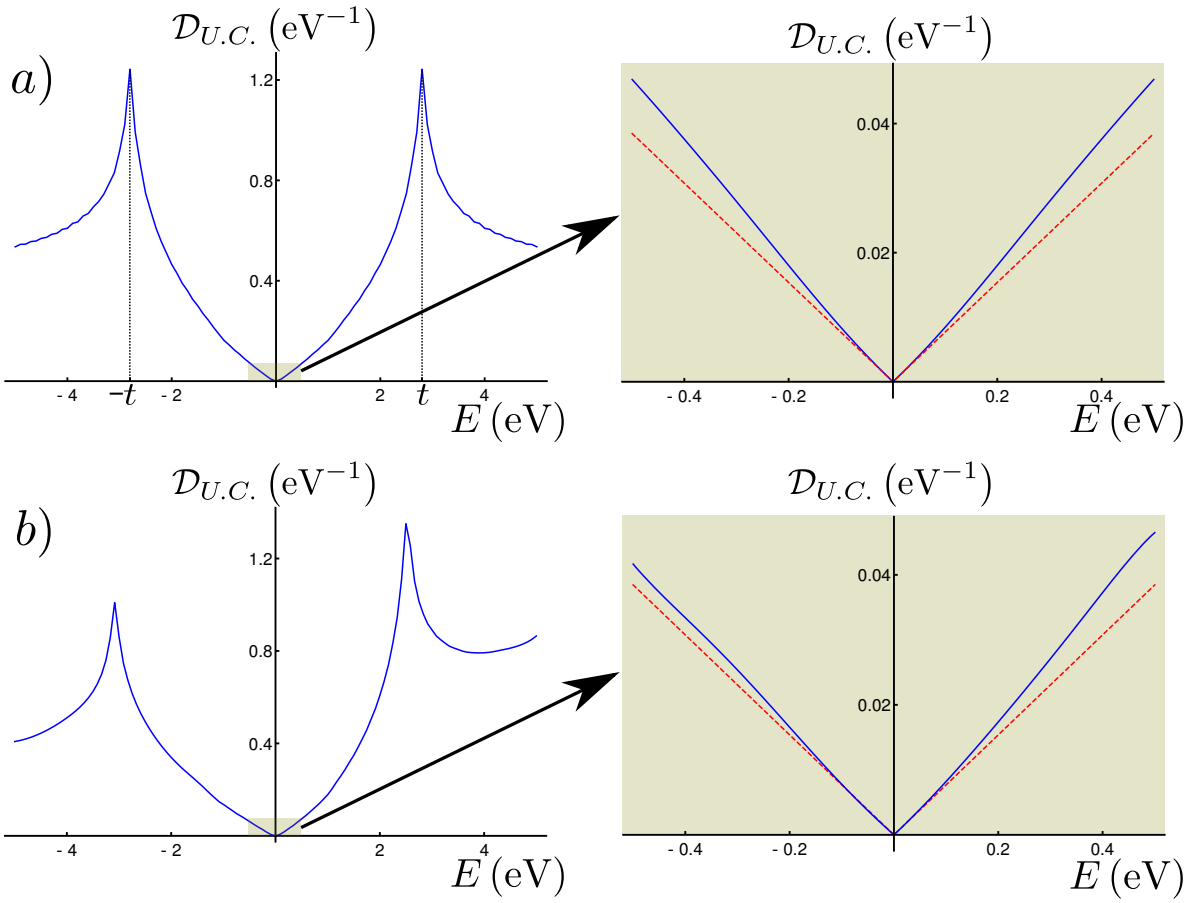

Figure 1.8: The single-particle density of states per unit cell in monolayer graphene, $\mathcal{D}_{U.C.}(E)$, for (a) $t^{'} = 0$ and (b) $t^{'} = 0.3$eV. Insets show the similarity between the numerical results (blue solid lines) generated using the full bandstructure and the low energy approximation (red dashed lines) in the low-energy regime.

where $c = 3 \times 10^8 \mathrm{ms}^{-1}$ is the speed of light in vacuum. Thus, for a particle with zero rest mass, we recover the conical dispersion discussed previously: $E_{\pm} = \pm cp$. This is an exact result for the case of an ultra-relativistic particle, which is not the case for the conical bandstructure of graphene, which we derived in the limit of low energy. Indeed, while for most purposes it is typically accepted that the conical approximation is a good one in graphene for energies in the range $|E| \lesssim 1$eV [7], it is clear from Fig. 1.7 that the bands are curved away from $E = 0$. It is one of the aims of this thesis to explain how that band curvature can result in new and interesting physics, and in this section we introduce the most important non-linear terms in the Hamiltonian and explain their impact on the bandstructure.

In graphene, the Fermi velocity plays the role of an effective speed of light, but is two orders of magnitude lower [7]: $v_F = c/300$. In analogy to the case of ultra-relativistic particles, they behave as if they have no rest mass: $m_0 = 0$. Unlike the true Dirac particles, however, the fermions in graphene are electrons, and do have a rest mass which is hidden in the theory. The Dirac Hamiltonian for ultra-relativistic particles follows from Eq. (1.33) for $m_0 = 0$, and is given by $\widehat{H} = c\boldsymbol{\sigma} \cdot \boldsymbol{p}$, where the Pauli matrices $\boldsymbol{\sigma}$ enter the theory due to the spin-1/2 degree of freedom of the fermions. In graphene, however, spin does not seem to be particularly important. Indeed, spin is a degenerate coordinate in the system. Instead, we have seen that $\boldsymbol{\sigma}$ is a pseudospin: an internal degree of freedom arising due to the two-sublattice basis of the crystal. The negative root in Eq. (1.46) lead Dirac to the concept of antiparticles, which are analogous to vacancies in an an otherwise filled electron continuum at $E < -m_0c^2$. In graphene, the analogous excitations are instead holes, which can be thought of as vacancies in the valance band for $E < 0$ in intrinsic graphene. For hole doped graphene, where the Fermi level is below the neutrality point, electrons can be excited into the valence band and have energies which are negative with respect to the Dirac point but which are still above the Fermi level.

An often overlooked property of the bandstructure of graphene, and one which will lay the foundations for much of this thesis, is the absence of true electron-hole symmetry away from $E = 0$. This symmetry between the upper and lower cones is lifted, e.g., by a small band curvature. We extend the kinetic energy by quadratic terms compatible with the symmetries of the honeycomb lattice (see Refs. [2,29]). We write the single-particle kinetic energy in the form:

$$\begin{aligned} \widehat{H} &= v_F\boldsymbol{\sigma} \cdot \boldsymbol{p} - \alpha p^2 + \tau\mu(p_x + ip_y)^2\sigma_+ + \text{H.c.}, \\ &= \begin{bmatrix} -\alpha p^2 & v_F p e^{-i\phi_{\boldsymbol{p}}} + \tau\mu p^2 e^{2i\phi_{\boldsymbol{p}}} \\ v_F p e^{i\phi_{\boldsymbol{p}}} + \tau\mu p^2 e^{-2i\phi_{\boldsymbol{p}}} & -\alpha p^2 \end{bmatrix}. \end{aligned} \tag{1.47}$$

where $\sigma_+ = \frac{1}{2}(\sigma_x + i\sigma_y)$, $\tau = \pm 1$ for an electron in the $\boldsymbol{K}^{\pm}$ valley and H.c. denotes the Hermitian conjugate of the term preceding it. The second term in Eq. (1.47) is invariant under all two-dimensional rotations, and arises microscopically from contributions due to the hopping of electrons from one atom to its next-nearest-neighbour, giving $\alpha = \frac{9a^2t'}{4\hbar^2}$, where t' is the next-nearest-neighbour hopping parameter [7]. The third term (including H.c.) is invariant under rotations by 120°. This term represents trigonal-warping, and originates from nearest-neighbour hopping, expanded to second order in momentum [2, 7], so that $\mu = \frac{3a^2t}{8\hbar^2}$. It is the only term in the Hamiltonian which is different for the two valleys, due to the factor of τ which determines the sign of the warping. The derivation of the Hamiltonian in Eq. (1.47) follows in the same way as the conical Hamiltonian derived above, with the exception that the expansions of $f(\boldsymbol{k})$ and $g(\boldsymbol{k})$ given in Eqs. (1.25) are carried to second order in $\boldsymbol{p}$ (where, as above, $\boldsymbol{p} = \hbar\boldsymbol{k} - \hbar\boldsymbol{K}^{\pm}$ is a small momentum measured with respect to the Dirac points).

The eigenvalues of Eq. (1.47) give the energies of the two bands:

$$E_{\pm} = -\alpha p^2 \pm v_F p \pm \tau\mu p^2 \cos(3\phi_{\boldsymbol{p}}). \tag{1.48}$$

The presence of the first term breaks the electron hole symmetry (since $E_+ \neq -E_-$) and the final term warps the bands with the $2\pi/3$ rotational symmetry of the lattice. The energy surfaces, equipotential contours and some slices of the bandstructure near the $\boldsymbol{K}^+$-point are given in Fig. 1.9. All of the plots shown would be the same for the case of the $\boldsymbol{K}^-$-point with the exception of those containing trigonal warping due to the valley-symmetry-breaking prefactor of τ in Eq. (1.48). The $\tau = -1$ factor is equivalent to the transformation $\phi_{\boldsymbol{p}} \to \phi_{\boldsymbol{p}} + 2\pi/6$, so that the contours and energy surfaces in Fig. 1.9 are the same at the $\boldsymbol{K}^-$-point, up to a rotation of the momentum space.

In the following chapter, we will show how these nonlinear kinetic energy terms can play a crucial role in the physics of two interacting Dirac particles. Indeed, in the subspace of states annihilated by the operator $\boldsymbol{\sigma}\cdot(\boldsymbol{p}_1 + \boldsymbol{p}_2)$ (so that the conical terms are fully compensated), they are the only remaining terms in the kinetic Hamiltonian.

Because they can be of negative sign, we will show that, in this subspace, a pair of electrons interacting with formally repulsive forces (for example, the Coulomb interaction) can form tightly bound states.

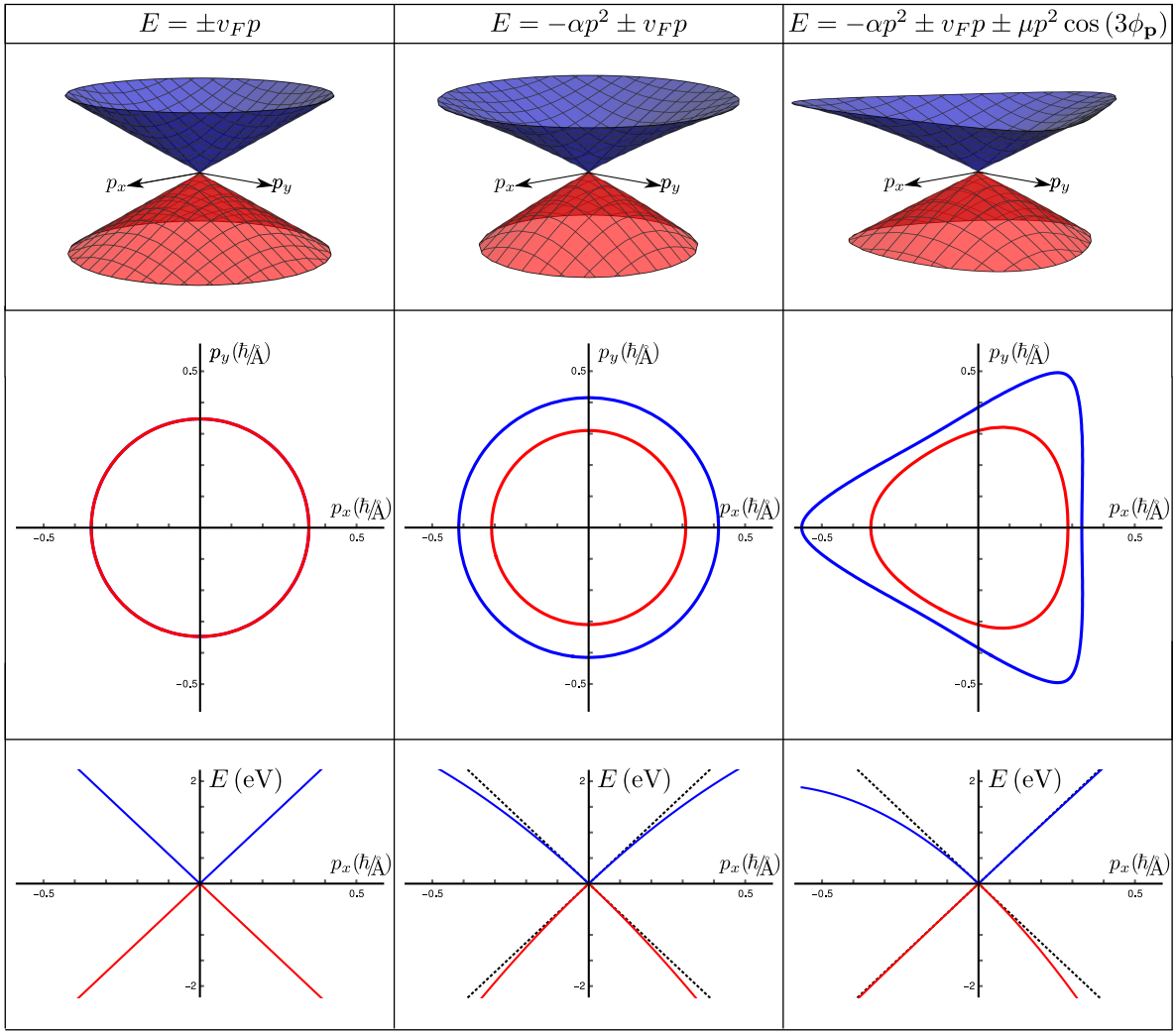

Figure 1.9: Electron-hole symmetry breaking at the $\boldsymbol{K}^+$-point in monolayer graphene. Left column: the conical approximation dispersion. Central column: dispersion including next-nearest-neighbour hopping. Right column: dispersion including next-nearest-neighbour hopping and trigonal warping. From top to bottom: energy surfaces, equipotential contours (at $E = \pm 2\text{eV}$) and a slice of the bandstructure (along $p_y = 0$). In all images, blue (red) surfaces and curves represent the conduction (valence) band, and dotted black lines show the cones for comparison.

Chapter 2

The two-body problem

2.1 Motivation

In this chapter, we study the two-body problem of a pair of interacting electrons in graphene. We will show that, subject to certain constraints on the parameters of the single-particle Hamiltonian, it is possible for the electrons to become tightly bound despite the formally repulsive Coulomb interaction between them. We will neglect some of the relevant many-body aspects of the problem (in particular, Pauli blocking and interaction screening), so as to treat the simplest possible system and illuminate the most important aspects of the pairing. Additionally, we will examine the semi-classical trajectories of the pairs, and estimate their lifetimes.

Recent experiments with high-quality samples suggest the existence of non-trivial correlated phases in graphene. In the Coulomb drag measurements of Ref. [30], for example, anomalous peaks in the drag resistivity were observed when both layers were tuned to charge neutrality (where the drag is expected to be a minimum). In finite magnetic field, the drag changed the sign, an effect tentatively linked to an analogous case in traditional semiconductor double-wells, which could be explained by the formation of an excitonic condensate. In the case of zero magnetic field, however, an enhancement of the drag resistivity is noted, and is explained by anticorrelated electron hole puddles in the two layers. Therefore, this experiment does not provide evidence of the zero-field

condensate predicted theoretically [31–33]. Indeed, that has not been observed [30,34]. This has provoked significant interest in the archetypical two-body problem [1,35–38].

In previous studies of the two-body problem in graphene [1,35], the interacting pair has been composed of Dirac quasiparticles each with linear dispersion, in monolayer graphene. In this approximation, there is an electron-hole symmetry which causes the two interacting particles to have equal and opposite kinetic energies: $E_i = \pm v_F p_i$ (as discussed in Section 1.4), where $i = 1, 2$ is the particle number.

Let us relabel the momentum of particle 1, relative to the Dirac point, to be $\boldsymbol{p}_1 \equiv \boldsymbol{p}$. By defining the total momentum of the pair, $\boldsymbol{K} = \boldsymbol{p}_1 + \boldsymbol{p}_2$, we can similarly re-write the momentum of particle 2: $\boldsymbol{p}_2 \equiv \boldsymbol{K} - \boldsymbol{p}$. In the regime where the centre of mass of the pair has no momentum ($\boldsymbol{K} = 0$), the dynamics lead to a vanishing of the kinetic energy. The two-particle quantum states can therefore be divided into dispersing (contributions for states where $E \neq 0$) and non-dispersing (those where $E = 0$) sectors (see Fig. 2.1 and the discussion below for further details). This can be understood as the addition or compensation of single-particle energies for particles in upper and lower bands. For the example of two electrons in the upper cone $E_1 + E_2 = v_F p + v_F p = 2v_F p$, but if they were in opposite cones $E_1 + E_2 = v_F p - v_F p = 0$. The states with $E = 0$ can be formed for any value of the momentum (within the limitations of the model). Thus, in the non-dispersing sector, there is an infinitely high degeneracy due to an infinite choice of possible momenta of the constituent particles. The contributions of such states were disregarded in previous works [1, 35], but we will show that their inclusion leads to anomalous electron pairing when one looks beyond the conical approximation.

Sabio *et al* treated the case of an interacting electron-hole pair in graphene, with a Hamiltonian corresponding to the low energy approximation with linear momentum terms and nearest-neighbour hopping [1]:

$$H = v_F \boldsymbol{\sigma}_1 \cdot \boldsymbol{p}_1 + v_F \boldsymbol{\sigma}_2 \cdot \boldsymbol{p}_2 + V(r) \tag{2.1}$$

Due to the chiral nature of Dirac fermions in graphene, the relative and centre of mass coordinates of the pair do not decouple, and the problem is non-trivial when approached analytically, allowing solutions for only certain circumstances. Most importantly, the calculations were for the most part performed for the case of an exciton with zero total kinetic energy (the centre of mass momentum $\boldsymbol{K} = 0$, and $\boldsymbol{p}_1 = -\boldsymbol{p}_2$). It was shown that in this regime some of the components of the Hamiltonian decouple, leading to non-analytic (delta function-like) properties of the wavefunctions. In addition, there was shown to be a class of zero-energy states which were non-normalizable, and these states were consequently dismissed from further analysis entirely.

Is it entirely physical to neglect the states in the non-dispersing sector due to their non-normalizability? To answer this question, let us consider the eigenvalues of Eq. (1.48). It is clear that, in the single-particle low-energy regime, the quadratic terms which arise due to next-nearest-neighbour hopping and trigonal warping vanish faster than those which are linear in the momentum. The conical approximation to the band-structure is only *exact*, however, precisely at the Dirac points. In that limit, one might then argue that it is physical to neglect the non-normalizable two-particle states within the non-dispersing sector. Recall, however, that the DOS vanishes at the Dirac points, so there is no phase space to support such states. One must then turn to the regime of small (but finite) single particle energies. In the non-dispersing sector, however, the conical picture is not a good approximation: because linear terms are fully compensated for two electrons in opposite cones and with opposite momenta ($\boldsymbol{K} = 0$), the quadratic terms of Eq. (1.48) become *more* important than the linear ones.

Let us examine the way in which higher order terms can at times reveal important physics hidden by the conical approximation. The effect of dispersion on the excitonic physics can be seen if one considers Dirac particles interacting via the Coulomb potential, which scales as $V(r) \sim -\frac{Ze^2}{\epsilon r}$. In the conical approximation, the kinetic energy scales as $v_F p \sim \frac{\hbar v_F}{r}$ due to the uncertainty principle. In the case of a single particle interacting with a static charge, Dirac vacuum reconstruction occurs when the potential

energy dominates over kinetic energy [16]: $\frac{Ze^2}{\epsilon} > \frac{\hbar v_F}{2}$. In the case of two carriers, however, a doubling of the relative velocity effectively doubles the critical charge for which collapse is possible [1]: $Z_C \gtrsim 2$. This renders the strongly-interacting regime irrelevant for electron-hole physics. For a weaker, quadratic dispersion ($p^2 \sim \frac{\hbar^2}{r^2}$), however, bound states can form for arbitrarily small interaction strength. For this reason, the previously neglected contribution of non-dispersing states [1, 35] can be important for understanding the two-particle physics of graphene. To this end, the two-body problem was re-analyzed by Mahmoodian *et al* with the inclusion of trigonal-warping terms which preserve the symmetry between the two cones but do not lead to non-zero kinetic energy when the total momentum of the pair is zero [36]. In this thesis we introduce quadratic momentum terms due to next-nearest-neighbour hopping which were ignored by Ref. [36] and show that this leads to the finite kinetic energy necessary for bound state formation. In particular, we will show that this leads to a new class of states which exist regardless of the orientation in momentum space (and cannot arise due to trigonal terms alone due to sign-indefinite kinetic energy). The formation of pairs of particles in the same valley is allowed for the model we consider here, which was not the case for the electron-hole case in Ref. [36].

In this chapter, we show that Cooper-pair-like states can be formed in the subspace of non-dispersing two-particle states. The dynamics in this sector is governed by quadratic terms in the single-particle dispersion. We have already seen in Section 1.6 that two such contributions are possible: an isotropic term due to next-nearest-neighbour hopping, $\epsilon_I \propto p^2$, and an anisotropic term due to trigonal-warping, $\epsilon_A \propto p^2 \sin(3\phi_{\boldsymbol{p}})$, where $\phi_{\boldsymbol{p}}$ is the polar angle in momentum space defined by $\tan(\phi_{\boldsymbol{p}}) = \frac{p_y}{p_x}$. We show that, depending upon the relative magnitudes of these two terms, two regimes are possible. When the isotropic contribution dominates, bound states can be formed; otherwise it is possible to form non-dispersing quasibound states (which can leak into the continuum). We calculate the binding energies of such states numerically, for a double-layer configuration, and discuss the decay rate due to coupling to the contin-

uum of dispersing states. In order to gain an intuition for the pairing, we also discuss the semi-classical equations of motion, and resultant trajectories, of the pairs.

2.2 Effective Hamiltonian

We begin by analyzing the kinetic energy of two Dirac quasiparticles in graphene. We have seen already that electrons in graphene can reside on two sublattices (A and B), so that they are to be described by a two-component Dirac spinor, and that the internal degree of freedom arising due to the presence of the sublattices is known as pseudospin. In the low-energy approximation, the Dirac spinors for the two valleys, $\boldsymbol{K}^+$ and $\boldsymbol{K}^-$, can be treated as fully independent. We define these spinors as $\psi_{\boldsymbol{K}^+} = \left[\psi^A_{\boldsymbol{K}^+}, \psi^B_{\boldsymbol{K}^+}\right]^T$ and $\psi_{\boldsymbol{K}^-} = \left[\psi^B_{\boldsymbol{K}^-}, \psi^A_{\boldsymbol{K}^-}\right]^T$, where A and B label the probability amplitudes for the two sublattices. In the conical approximation, the dynamics of a single particle is governed by the Hamiltonian $\widehat{H}_i = v_F \boldsymbol{\sigma}_i \cdot \boldsymbol{p}_i$, where the subscript labels the particle.

To understand the behaviour of a pair of particles in the conical regime in graphene, we begin by neglecting the electron-electron interactions and focus on the kinetic energy of the pair. The Hamiltonian $\widehat{H}_1$ of particle 1 is expressed in the pseudospin basis $\{|\uparrow_1\rangle, |\downarrow_1\rangle\}$ (see Eq. (1.34) and preceding discussion) which spans the space $\mathcal{H}_1$. Similarly, the kinetic energy of particle 2 is determined by $\widehat{H}_2$ which acts on the space $\mathcal{H}_2$ in the basis $\{|\uparrow_2\rangle, |\downarrow_2\rangle\}$. The two-particle states live in the tensor product space defined by $\mathcal{H} = \mathcal{H}_1 \otimes \mathcal{H}_2$. We choose to work with the Schmidt basis, which is akin to taking ordered pairs of the pseudospins of constituent particles: $\{|\uparrow\uparrow\rangle, |\uparrow\downarrow\rangle, |\downarrow\uparrow\rangle, |\downarrow\downarrow\rangle\}$, where, e.g., $|\uparrow\downarrow\rangle = |\uparrow_1\rangle \bigotimes |\downarrow_2\rangle$. Within this formalism, the pair is governed by the dispersion arising from the relative motion of its constituent particles, represented by $\widehat{H}_L = \widehat{H}_1 \oplus \widehat{H}_2 = v_F \boldsymbol{\sigma}_1 \cdot \hat{\boldsymbol{p}}_1 + v_F \boldsymbol{\sigma}_2 \cdot \hat{\boldsymbol{p}}_2$, where $\boldsymbol{\sigma}_i$ is the pseudospin operator, subscripts denote the particle number and $\hat{\boldsymbol{p}}_i$ is a small momentum measured with respect to the $\boldsymbol{K}^+$- or $\boldsymbol{K}^-$-point. For clarity, we have written the pseudospin operators in compact form ($\boldsymbol{\sigma}_1 \equiv \boldsymbol{\sigma}_1 \otimes \sigma_{0,2}$ and $\boldsymbol{\sigma}_2 \equiv \sigma_{0,1} \otimes \boldsymbol{\sigma}_2$) because they act on the single particle

subspaces. We focus on states with zero total momentum, such that $\boldsymbol{p} = \boldsymbol{p}_1 = -\boldsymbol{p}_2$. The eigenstates of $\widehat{H_L}$ are given by:

$$\begin{aligned}
|1, \phi_{\boldsymbol{p}}\rangle &= \frac{1}{\sqrt{2}}\left[e^{-i\phi_{\boldsymbol{p}}}|\uparrow\uparrow\rangle + e^{i\phi_{\boldsymbol{p}}}|\downarrow\downarrow\rangle\right], \\
|2, \phi_{\boldsymbol{p}}\rangle &= \frac{1}{\sqrt{2}}\left[|\uparrow\downarrow\rangle + |\downarrow\uparrow\rangle\right], \\
|3, \phi_{\boldsymbol{p}}\rangle &= \frac{1}{2}e^{i\phi_{\boldsymbol{p}}}|\downarrow\downarrow\rangle - \frac{1}{2}e^{-i\phi_{\boldsymbol{p}}}|\uparrow\uparrow\rangle + \frac{1}{2}\left[|\uparrow\downarrow\rangle - |\downarrow\uparrow\rangle\right], \\
|4, \phi_{\boldsymbol{p}}\rangle &= \frac{1}{2}e^{-i\phi_{\boldsymbol{p}}}|\uparrow\uparrow\rangle - \frac{1}{2}e^{i\phi_{\boldsymbol{p}}}|\downarrow\downarrow\rangle + \frac{1}{2}\left[|\uparrow\downarrow\rangle - |\downarrow\uparrow\rangle\right].
\end{aligned} \tag{2.2}$$

The states in Eq. (2.2) have corresponding eigenvalues $E_{1,2} = 0$ and $E_{3,4} = \pm 2v_F p$. Thus, the subspace spanned by $|1, \phi_{\boldsymbol{p}}\rangle$ and $|2, \phi_{\boldsymbol{p}}\rangle$ from Eq. (2.2) is the *non-dispersing sector*. Such states are formed by electron quasiparticles in opposite cones, with the same magnitude of momentum, so that the relative velocity of the pair vanishes. Thus, for the remainder of this work, we will call states with configuration $|1, \phi_{\boldsymbol{p}}\rangle$ the *ortho-states* and those with configuration $|2, \phi_{\boldsymbol{p}}\rangle$ the *para-states*, in analogy with the states of positronium. Similarly, the subspace spanned by $|3, \phi_{\boldsymbol{p}}\rangle$ and $|4, \phi_{\boldsymbol{p}}\rangle$ forms the *dispersing sector*, in which the velocities are opposite. In the absence of interactions, all states in the non-dispersing sector are infinitely degenerate. We note that this degeneracy is lifted if the symmetry between the upper and lower cones is broken, e.g., by a small band curvature, as was explained in Chapter 1.

Let us recall the form of the single-particle kinetic energy which includes the effects of trigonal warping and next-nearest-neighbour hopping:

$$\widehat{H}_i = v_F \boldsymbol{\sigma}_i \cdot \boldsymbol{p}_i - \alpha p_i^2 + \tau_i \mu (p_{x,i} + i p_{y,i})^2 \sigma_{+,i} + \text{H.c.}, \tag{2.3}$$

which is the same as Eq. (1.47), with the inclusion of the subscript i which labels the particle. Although the quadratic terms are small in the limit $p \to 0$, we have seen that they are particularly important for particles in opposite cones (since $E_{1,2} = 0$ in the non-dispersing sector). Thus, our aim is to study the effects of these terms on the states in the subspace spanned by the ortho- and para-states: $\{|1, \phi_{\boldsymbol{p}}\rangle, |2, \phi_{\boldsymbol{p}}\rangle\}$. This is

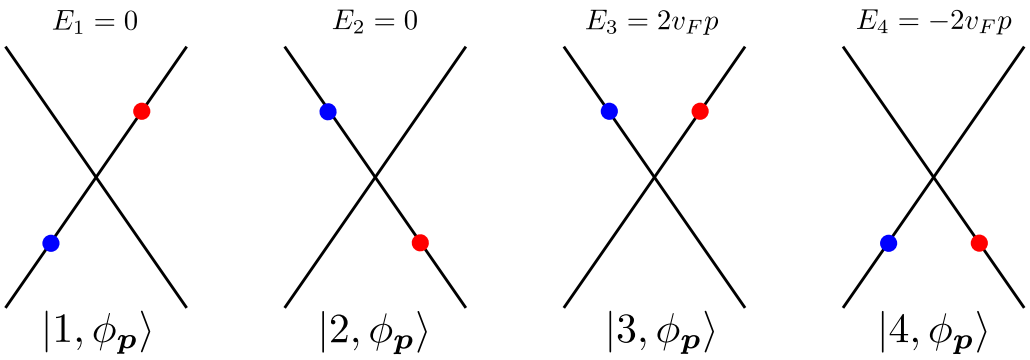

Figure 2.1: A schematic of the four eigenstates of the two-particle kinetic Hamiltonian. $\boldsymbol{K} = 0$ in each case, and $\boldsymbol{p}$ is the same throughout. The states can be divided into two sectors: those in which the particles are in opposite bands ($E_{1,2} = 0$) and those in which the particles are in the same band ($E_{3,4} = \pm 2v_F p$). The colours of the electrons are included to distinguish between particle 1 and particle 2.

achieved, e.g., by constructing the two-particle Hamiltonian, and projecting out states with non-zero weights along $|3, \phi_{\boldsymbol{p}}\rangle$ and $|4, \phi_{\boldsymbol{p}}\rangle$. The Hamiltonian which acts on $\mathcal{H}$ and includes the effects of these extra terms is $\widehat{H}_{1,2} = \widehat{H}_1 \oplus \widehat{H}_2$:

$$\widehat{H}_{1,2} = \begin{bmatrix} -2\alpha p^2 & f_2(-\boldsymbol{p}) & f_1(\boldsymbol{p}) & 0 \\ f_2^*(-\boldsymbol{p}) & -2\alpha p^2 & 0 & f_1(\boldsymbol{p}) \\ f_1^*(\boldsymbol{p}) & 0 & -2\alpha p^2 & f_2(-\boldsymbol{p}) \\ 0 & f_1^*(\boldsymbol{p}) & f_2^*(-\boldsymbol{p}) & -2\alpha p^2 \end{bmatrix}, \tag{2.4}$$

where $f_i(\boldsymbol{p}) = v_F p e^{-i\phi_{\boldsymbol{p}}} + \tau_i \mu p^2 e^{2i\phi_{\boldsymbol{p}}}$ and, as above, $\boldsymbol{p} = \boldsymbol{p}_1 = -\boldsymbol{p}_2$. To examine the dynamics in the non-dispersing sector, we restrict the two-particle Hamiltonian to this subspace. We explicitly treat two distinct cases: *direct pairs* (when both particles are in the same valley) and *indirect pairs* (opposite valleys). All ortho- and para-states are annihilated by the operator $(\boldsymbol{\sigma}_1 - \boldsymbol{\sigma}_2) \cdot \boldsymbol{p}$. In calculating the matrix elements of the kinetic energy we change to the eigen-basis defined by Eq. (2.2) and project out the

high-energy degrees of freedom, giving the effective Hamiltonian matrix [39]:

$$\widehat{H}^{\text{eff}}_{1,2} = \begin{bmatrix} -\frac{p^2}{2m^*} & \tau_{1,2}\mu p^2 \sin(3\phi_{\boldsymbol{p}}) \\ \tau_{1,2}\mu p^2 \sin(3\phi_{\boldsymbol{p}}) & -\frac{p^2}{2m^*} \end{bmatrix}, \tag{2.5}$$

where the rows and columns correspond to states $|1, \phi_{\boldsymbol{p}}\rangle$ and $|2, \phi_{\boldsymbol{p}}\rangle$, $m^* = 1/4\alpha$ is a two-particle effective reduced mass and $\tau_{1,2} = \tau_1 + \tau_2$. For further details about the calculation of $\widehat{H}^{\text{eff}}_{1,2}$, see Appendix A. The eigenvalues of Eq. (2.5) are given by:

$$E = -\frac{p^2}{2m^*} \pm |\tau_{1,2}|\mu p^2 \sin(3\phi_{\boldsymbol{p}}). \tag{2.6}$$

It is easily verified that these are the two eigenvalues of Eq. (2.4) corresponding to the non-dispersing sector.

Let us clarify the meaning of the pair having "zero total momentum" for both direct and indirect pairs. Recall that the single particle momentum $\boldsymbol{p}_i$ is measured with respect to one of the Dirac points. A schematic of what it means for $\boldsymbol{p}_1 + \boldsymbol{p}_2 = 0$ is given in Fig. 2.2. If we define $\boldsymbol{P}_i$ to be the momentum of the particle with respect to the $\boldsymbol{\Gamma}$-point (the centre of the Brillouin zone, as in Fig. 1.5) then $\boldsymbol{P}_i = \boldsymbol{K}^{\pm} + \boldsymbol{p}_i$. Therefore, for the case of interest, where $\boldsymbol{p} = \boldsymbol{p}_1 = -\boldsymbol{p}_2$:

$$\boldsymbol{P}_1 + \boldsymbol{P}_2 = \begin{cases} 2\boldsymbol{K}^+, & \text{for direct pairs in the } \boldsymbol{K}^+ \text{ valley} \\ 2\boldsymbol{K}^-, & \text{for direct pairs in the } \boldsymbol{K}^- \text{ valley} \\ \boldsymbol{K}^+ + \boldsymbol{K}^-, & \text{for indirect pairs.} \end{cases} \tag{2.7}$$

For indirect pairs, the total momentum $\boldsymbol{K}^+ + \boldsymbol{K}^-$ is equal to a reciprocal lattice vector, so that the dynamics are identical to the pair with $\boldsymbol{P}_1 + \boldsymbol{P}_2 = \boldsymbol{\Gamma}$ in analogy with pairs in the Cooper channel of superconductors. For direct pairs, the situation is different: particles lying equidistant from, and on oposite sides of, the same Dirac point have a non-vanishing total momentum. Thus indirect pairs, with vanishing true momentum, are most likely of greater importance in the experiment, as they can be excited by

zero-momentum probes. We note that for all of the above cases, however, the particles are in opposite bands, so that this momentum configuration leads to non-zero band velocity of the pair. We will examine this in more detail in Section 2.4.

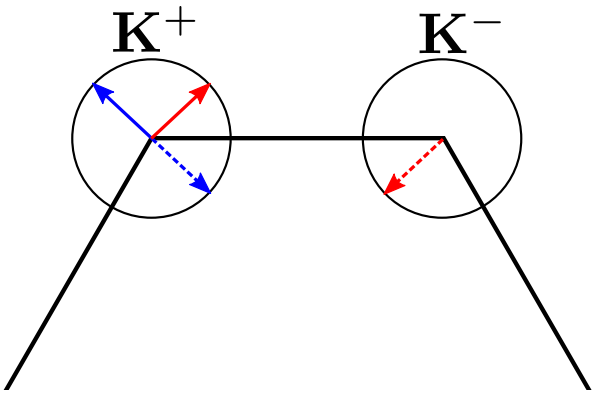

Figure 2.2: Electron momenta at the Brillouin-zone corners. Example momentum configurations for direct (indirect) pairs are represented by blue (red) arrows. Solid (dashed) arrows correspond to the momentum of particle 1 (particle 2).

We will show that some of the features in the dynamics of two-particle states crucially depend upon the signs and relative magnitudes of the quadratic terms, i.e., on the values of m^* and μ. It has been shown by a variety of different approaches [7,23–26] that t and t' have the same sign, however there is a disagreement on the precise value of t'. *Ab initio* calculations [7,23] give the range $0.02t \leq t' \leq 0.2t$, while cyclotron resonance [24], quantum capacitance [25] and polarization-resolved magnetospectroscopy [26] measurements have produced $t' = 0.04t, 0.11t$ and $0.14t$ respectively. The full two-particle kinetic energy is $\widehat{H}_{1,2} = \widehat{H}_1 + \widehat{H}_2$, and so $-m^*$ plays the role of a two-particle reduced mass due to the $-\frac{p^2}{2m^*}$ term which arises when $\widehat{H}_{1,2}$ is written explicitly, with the corresponding range of values $0.7 \leq \frac{m^*}{m_e} \leq 7.5$. This implies that the isotropic kinetic energy term is negative definite, which will be shown to be of crucial importance to the spectrum of two-particle states.

2.3 Bound states of electron pairs

To understand the dynamics of pairs described by the kinetic energy terms in $\widehat{H}_{1,2}$, let us first consider the simplest case of indirect pairs, where the electrons are in opposite valleys. In this configuration $\tau_{1,2} = 0$, so that the contribution of trigonal-warping vanishes and the only remaining kinetic term is $-\frac{p^2}{2m^*}$. The dynamics of the interacting pair is therefore described by the Hamiltonian $H_I = -\frac{p^2}{2m^*} + U(r)$ for para-states, where $U(r)$ is the potential energy. The Hamiltonian H_I describes the motion of a particle with *negative* effective mass $-m^*$ in the external potential $U(r)$. We note that $-H_I$ describes the motion of a particle with a *positive* mass m^* in an attractive potential. In two dimensions, an arbitrarily weak attractive potential exhibits at least one bound state at negative energies for massive particles [40]. It follows, therefore, that H_I will exhibit positive energy bound states if $U(r)$ is repulsive. This property is a direct consequence of the negative definite kinetic energy of the pair, the dynamics of which is akin to the motion of a hole-like state near the top of the valence band in a semiconductor: the repulsive potential due to a negatively charged impurity is perceived as an attraction due to negative band curvature. In the real space picture, two electrons with opposite momenta reside in different cones and have nearly the same velocities. The repulsive force tends to increase the momentum of one electron, and decrease the momentum of the other. Due to the negative dispersion term, this decreases the velocity of the first particle, and increases the velocity of the other, reducing the distance between them. Unlike conventional bound states, these positive eigenstates are metastable. Formation of regular (electron-hole) excitons is prohibited in this regime.

Since the effective mass ($-m^*$) is only about five times larger than the free electron mass, the binding can be quite strong. For the example of a repulsive Coulomb interaction, $U(r) = \frac{e^2}{\epsilon_s \epsilon_N r}$, the problem reduces to the two-dimensional hydrogen atom [41]. (Here $\epsilon_N = 1 + \frac{N\pi e^2}{8\epsilon_s \hbar v_F}$ is the intrinsic dielectric constant [42] of graphene embedded in a material with dielectric constant ϵ_s. For single (double) layer graphene, the number of fermion species is $N = 4$ ($N = 8$)). The highest energy level is given by $E_1 = \frac{2m^* e^4}{\epsilon_s^2 \epsilon_4^2 \hbar^2}$.

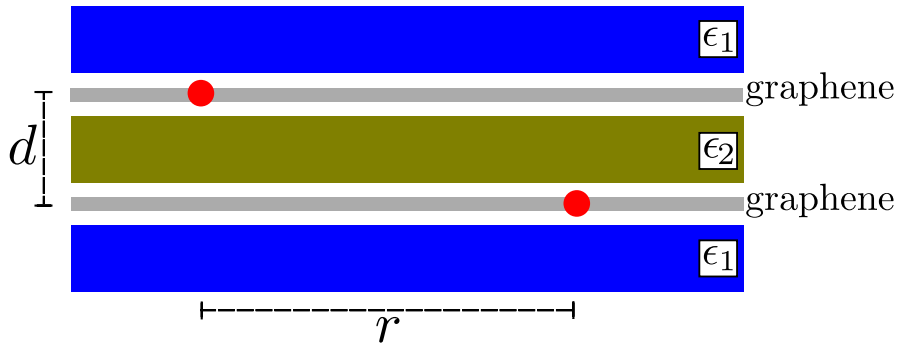

Figure 2.3: A toy model of our problem: two electrons (red circles), which are isolated in parallel graphene layers, interact via a Coulomb potential but are electrically isolated by an intermediate dielectric spacer (green) of relative permittivity ϵ_2. That double-layer structure is embedded in a (in general) different dielectric medium (blue), of relative permittivity ϵ_2. The in-plane distance between the electrons is r and the separation between the layers is d.

We note that the hydrogen-like Hamiltonian H_I results in binding energy $E_1 \sim 1.5$eV and Bohr radius $a_B \sim 2.5$Å for $t' = 0.1t$. At such short distances, the low-energy approximation to the graphene band structure is not valid [43], rendering the solution inconsistent. More importantly, the dynamics of particles at such high energies is affected by Pauli blocking due to the Dirac sea. For the bound state to be observable, the relevant phase space domain must be free from other particles. This can be achieved by, e.g., gating, if the bound state energy is well below 1eV.

Two-particle states with smaller binding energies can be realized in double-layered structures where the electrons in opposite layers are separated vertically by a dielectric spacer of thickness d. We provide a schematic of such a construction in Fig. 2.3. Note that for the case of interest here $\epsilon_1 = \epsilon_2 \equiv \epsilon_s$, and the case of inequivalent dielectrics ($\epsilon_1 \neq \epsilon_2$) will become important in Chapter 4. Hexagonal boron nitride ($\epsilon_s = 3 - 4$) spacers have been experimentally shown to electrically isolate parallel graphene layers at a thickness of 4 atomic layers ($d = 1.3$nm) [44]. This suppresses the $\frac{1}{r}$ singularity, yielding smaller binding energies. For a rough estimate of the binding energy we approximate the potential as $V(r) \sim e^2/\epsilon_s\epsilon_4^2\sqrt{r^2+d^2}$ (see Chapter 3). The spectrum of the resulting shallow well can be found in the harmonic approximation, assuming $r \ll d$. The energy of the highest bound state is $E_0 = -\hbar\omega + \frac{e^2}{\epsilon_s\epsilon_4^2 d}$, where $\omega = \sqrt{\frac{e^2}{\epsilon_s\epsilon_4^2 m^* d^3}}$ is

the oscillation's angular frequency near the potential maximum. For example, $t' = 0.1t$ gives binding energy $E_0 = 31$meV. For the case of direct pairs the trigonal warping is not compensated ($\tau_{1,2} \neq 0$), and the situation becomes more complicated. We note, however, that if the mass m^* is small enough the trigonal warping terms cannot change the sign of the kinetic energy. Further, there are several momentum space orientations for which $\sin(3\phi_{\boldsymbol{p}}) = 0$. We therefore take E_0 as a first approximation of the binding energy for direct *and* indirect pairs.

To analyze the case of the direct pair with anisotropic dispersion, we derive its effective Hamiltonian in momentum space. The potential energy $V(r)$ is represented by a non-local operator proportional to its Fourier transform $\tilde{V}_{\boldsymbol{p},\boldsymbol{p}'} = \tilde{V}(|\boldsymbol{p} - \boldsymbol{p}'|)$, while the kinetic energy terms are given by Eq. (2.5) for $\tau_{1,2} = \pm 2$. Restricting the potential energy to the non-dispersing sector requires some care due to a non-trivial overlap between non-dispersing states with different momenta: $\langle 1, \phi_{\boldsymbol{p}'} | 1, \phi_{\boldsymbol{p}} \rangle = \cos(\phi_{\boldsymbol{p}} - \phi_{\boldsymbol{p}'})$. For the case of direct interactions, the $(\boldsymbol{p}, \boldsymbol{p}')$ block of the Hamiltonian matrix takes the form:

$$\widehat{H}_{\boldsymbol{p},\boldsymbol{p}'} = \delta_{\boldsymbol{p},\boldsymbol{p}'} \widehat{H}^{\text{eff}}_{1,2} + \tilde{V}_{\boldsymbol{p},\boldsymbol{p}'} \begin{bmatrix} \cos(\phi_{\boldsymbol{p}} - \phi_{\boldsymbol{p}'}) & 0 \\ 0 & 1 \end{bmatrix}, \tag{2.8}$$

where $\widehat{H}^{\text{eff}}_{1,2}$ is given by Eq. (2.5). In the absence of inter-particle interaction the eigenvalues of this matrix are given by the kinetic energy terms: $\epsilon_2^{(2)} = -2\mu p^2 [\eta + \sin(3\phi_{\boldsymbol{p}})]$, where we have introduced the *anisotropy parameter* $\eta = \frac{6t'}{t}$ which is not physically tunable (uncertainty in the value of t' gives a range of possible values $0.12 \leq \eta \leq 1.2$). Depending on the value of η, the kinetic energy is either negative-definite ($\eta > 1$) or sign-indefinite ($\eta < 1$).

We proceed by numerically diagonalizing the Hamiltonian given by Eq. (2.8) using the interlayer interaction from Ref. [33]:

$$V_q = \frac{v_q e^{-dq}}{1 + 2\frac{N\pi\alpha}{8} + (\frac{N\pi\alpha}{8})^2 [1 - e^{-2dq}]}, \tag{2.9}$$

where $N = 4$ is the number of Fermion flavours, $\alpha = {}^{e^2}/_{\epsilon_s \hbar v_F}$ is the Coulomb coupling constant and v_q is the bare Coulomb interaction. for a full discussion, see Sec. 3.3. We outline the numerical procedure in Appendix B. Although it is assumed that the relevant phase space domain is free of other particles to avoid the effect of Pauli blocking, we will treat the case of screening at half-filling ($p_f = 0$) as a first approximation. Indeed, the dielectric contribution to the screening giving rise to ϵ_N occurs at scales smaller than the Fermi wavelength (λ_f), and is most important in the realistic limit of $\lambda_f \ll d$. To visualize the resulting wavefunctions, we calculate the local density of states (LDOS), $\nu(\epsilon, x, y) = \sum_n \delta(\epsilon - \epsilon_n)|\psi_n(x, y)|^2$, where x and y are the components of the in-plane separation and n labels the eigenstates. In the isotropic regime, $\eta > 1$, as is evidenced by Fig. 2.4a for $\eta = 1.1$, there is a formation of distinct, highly localized, bound states at $\epsilon_1 = 45$meV, $\epsilon_2 = 30$meV and $\epsilon_3 = 27$meV. We note that the energy of the highest bound state, ϵ_1, is very similar to the value predicted in the harmonic approximation above. This validates the further use of such an approximation in the calculations of the transition rates that are to follow. At negative energies there is a low intensity continuum of unbound states, which are only weakly coupled to the bound states due to the symmetry of the Hamiltonian, resulting in their large lifetimes.

In the anisotropic regime ($\eta < 1$), there are six *easy axis* angles, defined by the relation $\sin(3\phi_0) = -\eta$, along which the dispersion is effectively suppressed despite the broken conduction-valence symmetry. By concentrating the wavefunction along these axes, one constructs a state qualitatively similar to the non-dispersing solutions in which the interparticle distance takes a constant value r_0: $\psi(r) \propto \delta(r - r_0)$. The energies of these states (see Fig. 2.4b) follow the profile of the interaction potential, $\epsilon \approx U(r_0)$. Further, a negative energy state dragged into the positive continuum by the interaction potential can decay by changing its pseudospin configuration rather than by tunnelling through a barrier. This is wholly due to the sign-indefinite kinetic energy.

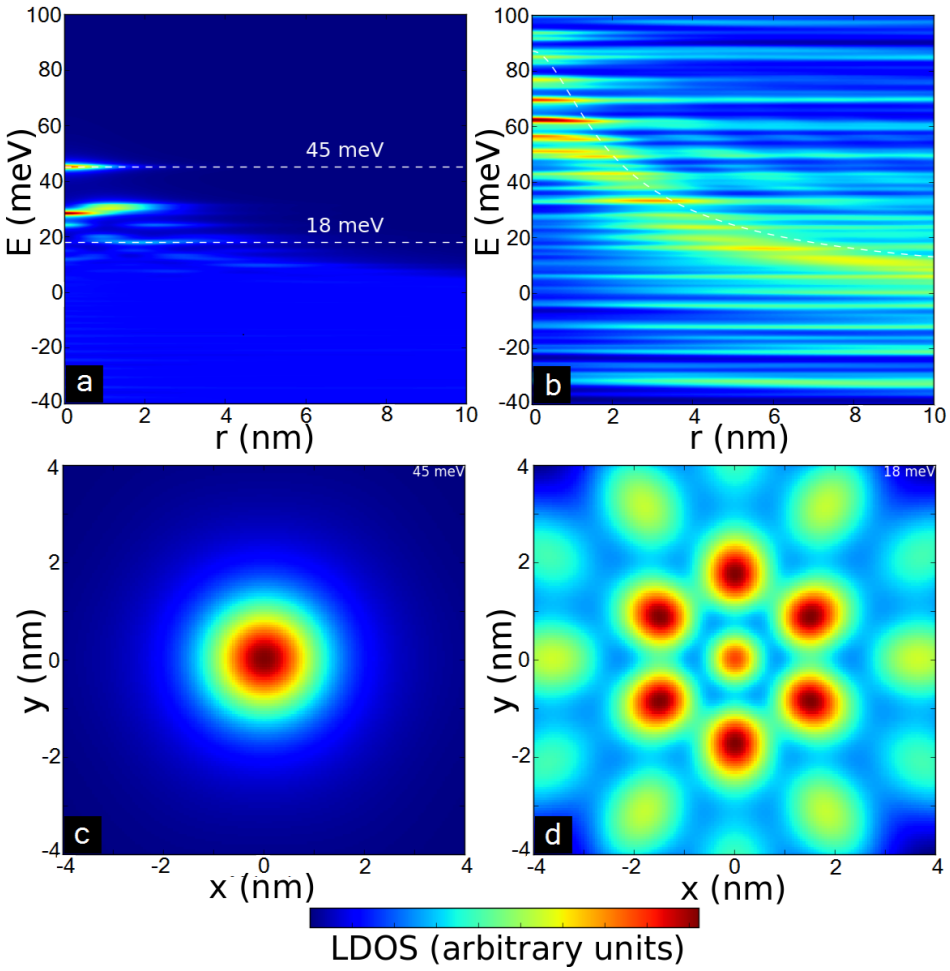

Figure 2.4: Two-body LDOS in a graphene hybrid structure as a function of binding energy E and interparticle distance r. The energy dependence shows distinct bound states in the (a) isotropic regime, which peel off into the free particle continuum in the (b) anisotropic regime (Coulomb potential in white). In real space, the wavefunctions are those of the states at $\epsilon_1 = 45$meV (Fig. (c)), and $\epsilon_2 = 18$meV (Fig. (d)).

2.4 Semiclassical trajectories

In this section, we will examine how the pairing of two like-charged particles can be facilitated by the Coulomb interaction, which is formally repulsive, by plotting the semiclassical trajectories of the pairs. In classical mechanics, a deterministic theory, one needs only the equations of motion, and initial values of the coordinates and momenta, to fully determine the time evolution of a system. In other words: if we know where a particle (or ensemble of particles) are, and we know where they are going, we can predict where they will be at some later time and draw a picture of their path.

This is not the case in quantum mechanics due to the canonical uncertainty principle, which states that there is a minimum bound on the products of the uncertainties of each coordinate and its corresponding momentum: $\Delta x_i \Delta p_{x_i} \geq \hbar/2$.

One implication of the uncertainty principle is that the concept of an absolute trajectory is meaningless in quantum mechanics. This can be understood with a simple thought experiment. We imagine that there is some measurement apparatus which will tell us, with arbitrary accuracy, the position of an electron which is constrained to move along the x-axis. As $\Delta x \to 0$, it is necessary that $\Delta p_x \to \infty$ in order to preserve the uncertainty relation. Now we know the exact position of our electron, but have no information about where it will be even a moment later and, therefore, cannot plot the path of the particle. This phenomenon is general, and not dependant on the chosen constraint or the precise details of the experiment.

In order to gain some intuition for the motion of the particles, we employ a semi-classical approximation: we determine the kinetic energies of the two particles as if they are quantum objects, and assume that these energies can be used in a classical Hamiltonian to determine the equations of motion. Treating the momenta as classical variables, the time evolution of the two-particle system is then governed by Hamilton's equations:

$$\begin{aligned} \frac{d\boldsymbol{p}_i}{dt} &= -\nabla_{\boldsymbol{x}_i} H, \\ \frac{d\boldsymbol{x}_i}{dt} &= \nabla_{\boldsymbol{p}_i} H, \end{aligned} \tag{2.10}$$

where the subscript $i = 1, 2$ denotes the particle number.

We will restrict our discussion to the case of indirect pairs in the subspace of para-states. In this case the kinetic energy is isotropic and there is a trivial overlap of states with different momenta. We take as the (classical) kinetic energy the relevant eigenvalue of the quantum Hamiltonian for each particle. These have been given previously in Eq. (2.6), and we will assume that particle 1 (particle 2) is in the upper (lower) cone. Thus,

we write:

$$H = -\frac{p_1^2 + p_2^2}{4m^*} + v_F(p_1 - p_2) + \frac{V_0}{\sqrt{|\boldsymbol{x}_1 - \boldsymbol{x}_2|^2 + d^2}}, \tag{2.11}$$

where $p_i = |\boldsymbol{p}_i|$ is the magnitude of the momentum for particle i, $\boldsymbol{x}_i = (x_i, y_i)$ is its position and $V_0 = \frac{e^2}{\epsilon_s \epsilon_N^2}$ determines the strength of the potential. We note the importance of retaining the linear terms in this analysis. Although we will restrict ourself to the $\boldsymbol{K} = 0$ channel, Hamilton's equations (Eq. (2.10)) act on the single particle coordinates and conjugate momenta independently of one another. Substitution of the Hamiltonian into Eqns. (2.10) give eight first-order coupled differential equations, which will be solved to obtain the equations of motion:

$$\begin{aligned} \frac{d\boldsymbol{p}_{1,2}}{dt} &= \pm \frac{V_0 \boldsymbol{r}_{12}}{[|\boldsymbol{r}_{12}|^2 + d^2]^{\frac{3}{2}}}, \\ \frac{d\boldsymbol{x}_{1,2}}{dt} &= -\frac{\boldsymbol{p}_{1,2}}{2m^*} \pm v_F \frac{\boldsymbol{p}_{1,2}}{p_{1,2}}. \end{aligned} \tag{2.12}$$

Due to the translational invariance of the potential, we have some extra flexibility in the choice of our initial conditions. In particular, at $t = 0$, particle 1 was chosen to reside at the origin, and particle 2 on the x-axis. The position of the second particle was chosen so that the initial distance between the particles was equal to the expectation value of the radial coordinate of a two-dimensional harmonic oscillator ground state wavefunction (which, based on our previous analysis, we take to be a typical size of the pair):

$$a_0 \equiv < r >_0 = \sqrt{\frac{\pi\hbar}{m^*\omega}} \sim 1\text{nm}. \tag{2.13}$$

To set the initial momenta, we note that there are only two free parameters, p and ϕ:

$$\begin{aligned} p_{x,1} &= -p_{x,2} = p\cos(\phi), \text{ and} \\ p_{y,1} &= -p_{y,2} = p\sin(\phi). \end{aligned} \tag{2.14}$$

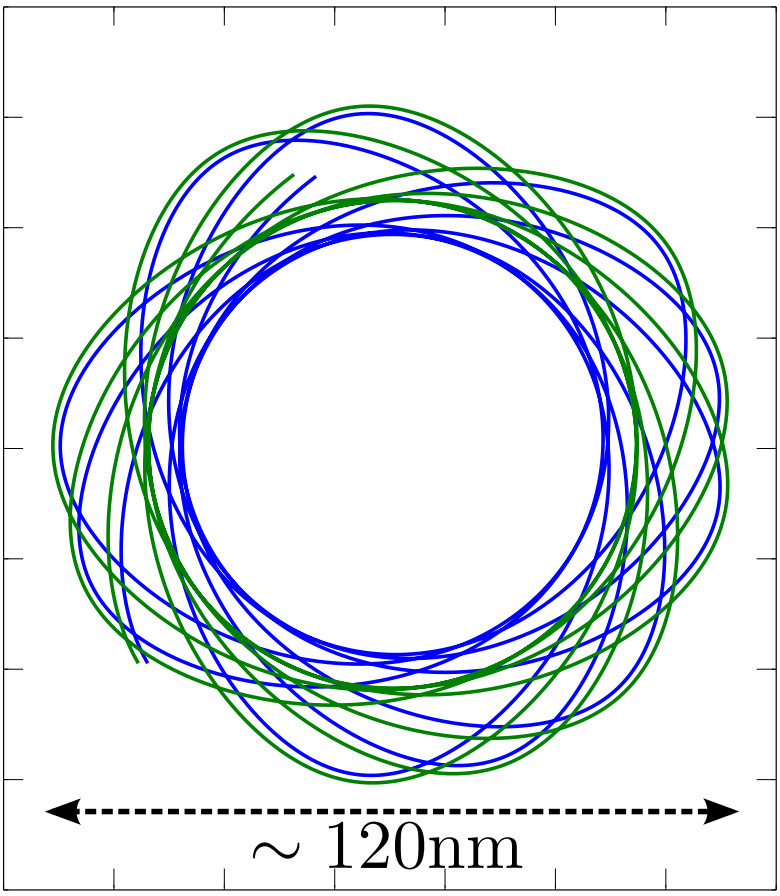

Figure 2.5: Typical trajectories of an electron pair with zero total momentum relative to the Dirac point, $\boldsymbol{p}_1 = -\boldsymbol{p}_2$, in separated graphene layers (separation $d = 1.3$nm) with a hBN dielectric spacer ($\epsilon_s = 3.9$). The constituent particles are in different colours, and the ticks on the axes correspond to steps of 20nm. Results were generated for the initial conditions $\phi(0) = 2\pi/3$ (relative to the x-axis) and $p(0) = 0.6p_{\max}$.

We know that, for the case of negative kinetic energy and repulsive potential, bound states have positive energy, $H > 0$. Therefore, we restrict ourselves to the pairing regime, which puts an upper bound on the magnitude of the momentum. We obtain,from Eqn. (2.11):

$$p_{\max} = \sqrt{\frac{2m^* V_0}{\sqrt{a_0^2 + d^2}}} \sim 1\frac{\hbar}{\text{nm}}. \tag{2.15}$$

We solved Eqns. (2.12) numerically using a 4^{th}-order Runge-Kutta procedure for the case of zero-total momentum of the pair relative to the Dirac point ($\boldsymbol{p}_1 = -\boldsymbol{p}_2$), and a typical result is given in Fig. 2.5.

For a pair with vanishing total momentum, $\boldsymbol{p}_1 = -\boldsymbol{p}_2 \equiv \boldsymbol{p}$, Eqns. (2.12) define the band velocities of the individual particles, which are given by

$$\boldsymbol{v}_{1,2} = v_F \hat{\boldsymbol{p}} \mp \frac{\boldsymbol{p}}{2m^*}, \tag{2.16}$$

where $\hat{\boldsymbol{p}}$ is a unit vector in the direction of $\boldsymbol{p}$. It is illuminating to consider the following change of variables:

$$\boldsymbol{v}_{cm} = \frac{1}{2}\left(\boldsymbol{v}_1 + \boldsymbol{v}_2\right) = v_F \hat{\boldsymbol{p}}, \tag{2.17}$$

and,

$$\boldsymbol{v}_r = \boldsymbol{v}_2 - \boldsymbol{v}_1 = \frac{\boldsymbol{p}}{m^*}, \tag{2.18}$$

which correspond to the centre-of-mass and relative velocities, respectively. It immediately follows that the trajectories of the electrons can be represented in terms of a superposition of two motions: a fast center-of-mass motion, characterized by the Fermi velocity, and a much slower relative motion, with velocity determined by the large effective mass m^*.

In the absence of interactions, and for small momenta, the relative velocity is sufficiently small that the pair behaves as if they were a single particle, moving with velocity v_F in the direction of the momentum. This is due to the chirality of carriers in graphene. The particles have opposite momenta of equal magnitude, but they are in opposite cones. The pseudospin projects onto the particle momentum in opposite directions in the two different cones, which changes the sign of the energy. Thus, the gradient of the band (the band velocity) is the same for opposite-cone particles with opposite momenta.

If we now switch on the inter-particle interaction, the momenta of the particles become time-dependent, in accordance with Eqns. (2.12). The sign of the interaction

is positive, but the effective forces carry opposite signs for the two particles, so that whenever $\boldsymbol{p}_1$ is increasing, $\boldsymbol{p}_2$ must be decreasing, and vice versa. Due to the sign of the parabolic energy term, this will cause the particle with the smaller of the two velocities to speed up slightly, and the other particle to slow down, closing the distance between the two particles. Therefore, the finite relative velocity implies that a repulsive force between the two particles will increase the velocity of one particle while decreasing the velocity of the other, causing them each to change direction slightly in such a way that their seperation is almost constant. This causes the two particles to behave as if they were "stuck together" despite the repulsive force.

Now let us note that the momentum $\boldsymbol{p}$ is changed by the interaction. Hence, as the particles are orbiting around their mass center, the direction of $\boldsymbol{v}_{cm}$ is also changing, so that the average velocity of the pair over a long time is zero, as can be seen from Fig. 2.5. The large value of v_F, compared to $\boldsymbol{v}_r$, results in non-propagating orbits of relatively large diameter $d \sim v_F/\omega$ where ω is the angular frequency of the orbit, which can be estimated as $\omega = E_0/\hbar$ ($d \sim 100$nm in Fig. 2.5).

2.5 Decay into the continuum

In our analysis so far we have only considered states in the non-dispersing ($E = 0$) sector. In view of any reasonable experiment, one might ask the following question: is it possible to populate a macroscopic number of bound states in the non-dispersing sector, or is their coupling to the continuum of dispersing states sufficiently strong so as to deem the previous analysis invalid? In other words, is it sufficient to treat states in the $E = 0$ subspace on their own, or do such states quickly decay? In this section we provide a partial answer to this question.

Coupling to the dispersing sector could lead to the decay of the metastable states found above, however these transitions are suppressed by momentum mismatch between the sectors. It is instructive to analyze the decay via Fermi's golden rule. Firstly, we

note that such a transition can only occur if it conserves the energy. Due to the repulsive interaction, we have found that the binding energy of the pair is positive. Therefore, due to energy conservation the decay is only allowed into states with positive energy $E = 2v_f p$. States with such energy exist in the continuum of non-interacting, two-particle dispersing states, and are given by $|3, \phi_{\boldsymbol{p}}\rangle$ in Eq. (2.2). Therefore the transition results in a pair of non-interacting electrons in the upper Dirac cone. The coupling between these two sectors occurs via trigonal-warping and potential energy terms, due to the non-trivial overlap between states with different momenta. The relevant matrix elements of the Hamiltonian are given by:

$$H_{1,3} = \frac{i}{\sqrt{2}} \tilde{V}_{\boldsymbol{p},\boldsymbol{p}'} \sin(\phi_{\boldsymbol{p}} - \phi_{\boldsymbol{p}'}), \tag{2.19}$$

$$H_{2,3} = i\sqrt{2}\mu p^2 \sin(3\phi_{\boldsymbol{p}})\delta_{\boldsymbol{p},\boldsymbol{p}'}, \tag{2.20}$$

where $H_{i,j} = \langle i, \phi_{\boldsymbol{p}'}| \, \widehat{H} \, |j, \phi_{\boldsymbol{p}}\rangle$ (see Appendix A for details).

We calculate the rate of transitions from bi-electronic bound states into the continuum of free states using Fermi's golden rule:

$$\Gamma = \frac{2\pi}{\hbar} |M_{if}|^2 \mathcal{D}_f, \tag{2.21}$$

where $\mathcal{D}_f$ is the density of final states and M_{if} is the transition matrix element:

$$M_{if} = \int \psi_f(\boldsymbol{r})^* H(\boldsymbol{r}) \psi_i(\boldsymbol{r}) d\boldsymbol{r}. \tag{2.22}$$

Due to the non-trivial overlap of states with different momenta, and the trigonal warping terms, it is not straightforward to express the Hamiltonian as a function of position. Instead, we will calculate the matrix elements in Eqn. (2.22) within the momentum-space representation. This is achieved by transforming the wavefunctions:

$$\psi_{i,f}(\boldsymbol{r}) = \int \tilde{\psi}_{i,f}(\boldsymbol{p}) e^{i\frac{\boldsymbol{p}\cdot\boldsymbol{r}}{\hbar}} \frac{d\boldsymbol{p}}{(2\pi\hbar)^2}, \tag{2.23}$$

and substitution into Eqn. (2.22). Thus we obtain:

$$M_{if} = \int \tilde{\psi}_f^*(\boldsymbol{p}')H_{\boldsymbol{p}'-\boldsymbol{p}}\tilde{\psi}_i(\boldsymbol{p})\frac{d\boldsymbol{p}}{(2\pi\hbar)^2}\frac{d\boldsymbol{p}'}{(2\pi\hbar)^2}. \tag{2.24}$$

We can represent the momentum-space wavefunctions in terms of a part which depends only on the pseudspin, and another which takes the form of the wavefunction of a massive particle ie. $\tilde{\psi}_i(\boldsymbol{p}) = \phi_i(\boldsymbol{p})\,|i, \phi_{\boldsymbol{p}}\rangle$ and $\tilde{\psi}_f(\boldsymbol{p}') = \phi_f(\boldsymbol{p}')\,|f, \phi_{\boldsymbol{p}'}\rangle$, for $i = 1, 2$ and $f = 3$. It follows from Eq. (2.24) that:

$$M_{i,f} = \int \phi_f^*(\boldsymbol{p}')H_{f,i}\phi_i(\boldsymbol{p})\frac{d\boldsymbol{p}}{(2\pi\hbar)^2}\frac{d\boldsymbol{p}'}{(2\pi\hbar)^2}. \tag{2.25}$$

In keeping with the harmonic approximation used so far, we assume that the initial wavefunctions are those of the ground state of the two dimensional harmonic oscillator:

$$\psi_i(\boldsymbol{r}) = \sqrt{\frac{2}{\pi}}\frac{1}{r_0}e^{-\frac{r^2}{r_0^2}}, \tag{2.26}$$

where $r_0 = \sqrt{2\hbar/m^*\omega}$ characterises the suppression of the wavefunction at large distances. In the momentum space picture, the wavefunction is given by the Fourier transform:

$$\phi_i(\boldsymbol{p}) = \int \psi_i(\boldsymbol{r})e^{-i\frac{\boldsymbol{p}\cdot\boldsymbol{r}}{\hbar}}d\boldsymbol{r} = \frac{2\sqrt{2\pi}\hbar}{p_0}e^{-\frac{p^2}{p_0^2}}, \tag{2.27}$$

where $p_0 = \sqrt{2m^*\omega\hbar}$ is the zero point momentum in the initial state. We approximate the final state wavefunctions by plane waves of wavevector $\boldsymbol{p}_f/\hbar$, which are highly localized in momentum space:

$$\phi_f(\boldsymbol{p}') \sim \delta(\boldsymbol{p}' - \boldsymbol{p}_f). \tag{2.28}$$

The transition matrix element due to the interaction potential, $M_{1,3}$, vanishes by symmetry if $\psi_i(\boldsymbol{p})$ is an s-state. Thus, we immediately obtain the decay rate:

$$\Gamma_{1\to 3} = 0. \tag{2.29}$$

Now let us turn to the kinetic energy term, $H_{2,3}$, which conserves the momentum. Therefore the decay occurs when the initial (p_i) and final (p_f) momenta satisfy conservation laws: $E_0 = 2v_F p_{i,f}$. Here E_0 is the energy of the ground state of a two-dimensional harmonic oscillator: $E_0 = -\hbar\omega + \frac{e^2}{\epsilon_s \epsilon_4^2 d}$ which gives $p_i \ll p_0$. The smallness of p_i results in a small matrix element which is proportional to p^2. The interaction cannot flip the spins, and we also assume that it does not scatter particles between the valleys. Notice that the dynamics for particles with configuration $|3, \phi_{\boldsymbol{p}}\rangle$ are the same as for free particles within the conical regime, subject to the replacement $v_f \to 2v_f$. Thus, the density of final states is given by Eq. 1.39, for a particle of velocity $2v_f$ (and $N = 1$, to account for the absence of spin-flipping and inter-valley scattering):

$$\mathcal{D}_f = \frac{|E|}{8\pi\hbar^2 v_F^2}. \tag{2.30}$$

Using the wavefunctions given in Eqs. (2.27) and (2.28) and Fermi's golden rule, we obtain for the decay rate of particles which are initially para-states:

$$\Gamma_{2\to 3} = \frac{\mu^2 p_f^4 E_0}{\pi\hbar v_f^2 p_0^2} \sim 10^{-10}\frac{E_0}{\hbar}. \tag{2.31}$$

This suggests only weak coupling to the continuum, justifying our consideration of the non-dispersing sector independently. Note that $H_{2,3}$ vanishes for indirect pairs, which do not decay by this mechanism.

These small values of the decay rate correspond to lifetimes on the order of $\sim 100\mu$s. Experiments with high-quality suspended devices have shown that the mean free path of carriers in graphene can be on the order of 1μm [45]. The scattering time of carriers

in zero-field is highly suppressed by the high Fermi velocity, however, so that such long mean-free-paths correspond to scattering times on the order of $\sim$ 1ps. This implies that the lifetime of the pair is likely to be limited by other, non-universal mechanisms, such as impurity, phonon or electron-electron scattering. This point was emphasised by Winkler *et al*, who noted that the long lifetimes of atom pairs in optical lattices (of the order of $\sim$ 100ms) were enabled by the near-absence of decay channels in the system, and would not likely be replicable in the condensed matter setting [46]. One might suggest that decay of the pair due to scattering is suppressed, by analogy to the traditional superconductors. The interaction potential that leads to the formation of Cooper pairs is attractive, however, so that at low temperatures they condense to the ground state. While the bi-electrons discussed herein may form condensates, they have positive energies, and the state of highest energy is the most stable. Thus, the energy of the phases would not be a minimum. This implies that there is no energy cost in splitting a pair into the two constituent electrons, as there is in a superconductor, so that scattering will indeed play an important roll. Thus, we reiterate that we have calculated the decay rates to justify the form of the effective Hamiltonian, which ignores the coupling between dispersing and non-dispersing sectors. Also, one has to bear in mind that higher-order virtual transitions could lift the restriction $p_f = p_i \ll p_0$. The detailed analysis of this strongly depends on the properties of $\tilde{V}_{\boldsymbol{p},\boldsymbol{p}'}$.

2.6 Repulsively bound pairs in other systems

Now that we have seen the mechanism which leads to the formation of bi-electrons in graphene, we are in a position to briefly note some of the literature pertaining to similar effects in other systems. In a 1971 paper, Gross *et al* reported anomalous optical spectra of BiI_3 [47]. The resonant absorption and emission lines were seen to obey the $\propto n^{-2}$ dependence of a hydrogen-like atom, but converged at long wavelengths. By fitting the lines to known formulae for such atoms, it was found that the particles involved were

not atoms, but rather particles with a similar effective mass to the electrons in BiI_3. Thus, the authors concluded that the anomalous lines were due to electron pairs with negative effective reduced mass (such as those states which might exist near the top of a band with negative curvature) [47].

Simple models of bound state formation due to a negative single-particle energy dispersion near the top band boundary were considered in Refs. [48, 49]. Mahajan *et al* showed that two-body bound states of like-charged particles occur for arbitrary periodic potentials, as long as the band gap is non-vanishing [48]. Souza *et al* treated the case of particles with an on-site repulsion, and showed that they can exhibit Bloch oscillations characteristic of doubly charged ($q = -2e$) pairs [49]. These studies have purported to explain the recent observations of bi-electron peaks in the photo-double-ionization spectra of aromatic hydrocarbons [50] and the pairing of ultracold rubidium atoms in an optical lattice [46].

We note, however, that the origin of the negative dispersion in graphene is different: the leading term in the single particle energy is linear, and the pair Hamiltonian arises via the compensation between the two sub-bands. This means that the dynamics of these pairs can be represented as a slow relative motion $v \propto p/m^*$ equation superimposed with the fast motion of the pair, $v \propto v_F$.

Chapter 3

Electron-electron interactions in single- and double-layer nanostructures

If one wants to study the many-electron system in graphene, one needs to take into account the effects of the Dirac sea on the electron-electron interaction of the pair. As an electron moves through a solid, it repels all of the other electrons in its immediate vicinity, so that it is surrounded by a region of positive charge due to the lattice ions which remain stationary. Many of the electric field lines of the electron terminate on the lattice ions, with only a few leaking out to interact with other, faraway electrons which are, in turn, dressed in their own small cloud of positive charge. For a high-density of the electron gas, the electron-electron interactions are heavily suppressed by this phenomenon, which is known as screening.

The simplest approach to the study of screening physics (beyond purely dielectric screening) is the Thomas-Fermi approximation, a semiclassical approach in which one derives the effective potential of an electron by considering its effect on the electronic density of an ideal electron gas [19]. Although the Thomas-Fermi approximation gives a reasonable qualitative description of traditional metals, it breaks down in graphene because the interactions are long-ranged at charge neutrality, where it screens like an

insulator. This can be understood by recalling that the density of states vanishes at the Dirac points in graphene, so that any transitions have to be between the bands if the valence band is full. Because the electron-electron interactions are long-ranged, one can not assume that the Dirac sea is a free electron gas. The simplest approach which accounts for the presence of an interacting Dirac sea is the Random Phase Approximation (RPA). First proposed in a series of four papers by Bohm and Pines [51–54] and later restated diagrammatically by Gell-Mann and Brueckner [55], the RPA is a perturbation series in r_s (the so-called Wigner-Seitz radius) which includes the most divergent bubble diagrams (see Fig. 3.1). Due to the dimensionality of graphene, and the relativistic nature of its elementary excitations, r_s is independent of the doping: $r_s = {}^{e^2}\!/_{\epsilon_s \hbar v_F} \left[{}^{4}\!/_{N}\right]^{1/2} \sim 0.5$ (for graphene on a SiO_2 substrate with $N = 4$). Thus, the RPA is a particularly good approximation for the case of graphene [42, 56], and has been used to analyse the dielectric function by a number of authors [42, 57–59].

In this chapter, we will study the form of the electron-electron interaction in single- and double-layer graphene. We begin by finding the form of the dielectric function for a graphene monolayer in Section 3.1, paying special attention to the roles of interband and intraband transitions. In particular, it will be explained why the vanishing density of states at the Dirac points prohibits the use of the Thomas-Fermi approximation and leads to screening physics altogether different to conventional metals. In Sections 3.2 and 3.3 we extend this theory to account for the screening interactions between electrons in parallel graphene layers. In Chapter 2, we made use of two intrinsic dielectric constants of graphene, which do not fully incorporate the screening behaviour. We will explain the origin of these factors in Sections 3.1 (for the single layer case) and 3.3 (for the double layer case) below. Finally, we explain why the short range of the interactions at finite doping permits us to replace the potential with a delta function as a first approximation, and study the strength of the coupling within such an approximation.

3.1 Screening properties of monolayer graphene

Here we will review the primary results pertaining to the screening physics of graphene (for full details, we refer the reader to Refs. [42,57–59]). The screened electron-electron interaction in the RPA is given by the bare-bubble diagram:

(3.1)

where double interaction lines represent the screened potential (V_q), single interaction lines represent the bare Coulomb interaction (v_q) and the fermion bubble represents the polarizability of a graphene monolayer ($\Pi(q,\omega)$). The solution to Eq. (3.1) is given by:

$$V_q = \frac{v_q}{1 + v_q \Pi(q,\omega)}, \tag{3.2}$$

where the polarizability is given by [42]:

$$\Pi(q,\omega) = -\frac{N}{\Omega} \sum_{\boldsymbol{k},s,s'} \frac{n_{s,\boldsymbol{k}} - n_{s',\boldsymbol{k}+\boldsymbol{q}}}{\omega + E_{s,\boldsymbol{k}} - E_{s',\boldsymbol{k}+\boldsymbol{q}} + i\eta} F_{s,s'}(\boldsymbol{k},\boldsymbol{q}), \tag{3.3}$$

where $s, s' = \pm 1$ are band indices, $\eta \to 0^+$ is a positive infinitesimal,

$$n_{s,\boldsymbol{k}} = \frac{1}{\exp(\beta(E_{s,\boldsymbol{k}} - E_F)) + 1} \tag{3.4}$$

is the Fermi-Dirac distribution at inverse temperature $\beta = 1/k_B T$ and

$$F_{s,s'}(\boldsymbol{k},\boldsymbol{q}) = \frac{1 + ss' \cos(\phi_{\boldsymbol{k}+\boldsymbol{q}} - \phi_{\boldsymbol{k}})}{2} \tag{3.5}$$

is the overlap of wavefunctions in the bands s and s' with wavevectors $\boldsymbol{k}$ and $\boldsymbol{k} + \boldsymbol{q}$.

For the entirety of this work, we will assume that $T = 0$, so that all of the states whose energies are below (above) the Fermi energy are occupied (vacant). We will also assume that interactions are instantaneous, because particles in graphene propagate

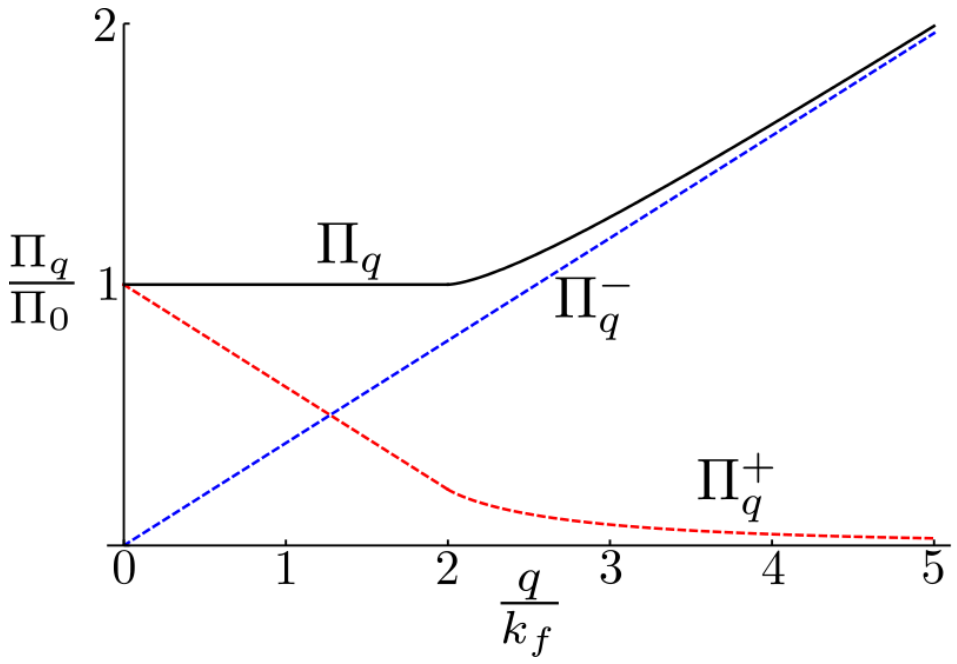

Figure 3.1: The static polarizability of graphene (black) can be separated into intrinsic (blue dashed) and extrinsic (red dashed) contributions.

much slower than light speed. This is called the static approximation, and is equivalent to setting $\omega = 0$ in the polarizability. Within this regime, the polarizability is known exactly [42], and is given by $\Pi(q, \omega = 0) \equiv \Pi_q = \Pi_q^+ + \Pi_q^- = \Pi_0(\tilde{\Pi}_q^+ + \tilde{\Pi}_q^-)$, where:

$$\tilde{\Pi}_q^+ = \begin{cases} 1 - \frac{\pi q}{8k_F}, & q \leq 2k_F \\ 1 - \frac{1}{2}\sqrt{1 - \frac{4k_F^2}{q^2}} - \frac{q}{4k_F}\sin^{-1}(\frac{2k_F}{q}), & q > 2k_F \end{cases}, \tag{3.6}$$

$$\tilde{\Pi}_q^- = \frac{\pi q}{8k_F},$$

and

$$\Pi_0 = \frac{N|E_F|}{2\pi(\hbar v_F)^2}, \tag{3.7}$$

is the density of states at the Fermi energy. This result is depicted in Fig. 3.1.

In Eq. (3.6) above, $\tilde{\Pi}_q^-$ is due to intrinsic effects, taking account of the electrons which fill the valence band in undoped graphene. Therefore, it is the only term which contributes to the polarizability in the absence of doping: $k_F = 0$. When $k_F \neq 0$, $\tilde{\Pi}_q^+$

also plays a role, and takes into account the presence of the electrons (holes) which reside in the conduction (valence) band when the system is doped away from charge neutrality. $\tilde{\Pi}_q^-$ arises due to transitions between the bands, because the phase space available for intra-band transitions is filled for valence electrons in intrinsic graphene. This restriction is partially lifted in extrinsic graphene, so that $\tilde{\Pi}_q^+$ takes into account inter-band *and* intra-band transitions. We note that this point is different to that put forward by the authors of Ref. [42], who claimed that $\tilde{\Pi}_q^-$ and $\tilde{\Pi}_q^+$ arose due to inter-band and intra-band transitions, respectively.

The screening behaviour of graphene can be pictured as partly metallic, and partly due to the effects of polarization (as in an insulator). For undoped graphene, $k_F = 0$ and all intra-band transitions are blocked by the Pauli exclusion principle. Thus, in this regime, graphene screens like an insulator. This effect can be absorbed into an "intrinsic dielectric constant" [42], which we used previously in Chapter 2. If we assume that the graphene layer is embedded within a dielectric environment of relative permittivity ϵ_s, then the bare Coulomb interaction (within the momentum representation) is given by:

$$v_q = \frac{2\pi e^2}{\epsilon_s q}. \tag{3.8}$$

The static dielectric function, for $k_F = 0$, then takes the form:

$$\epsilon(q) = 1 + v_q \Pi = 1 + \frac{N\pi e^2}{8\epsilon_s \hbar v_F} = 1 + \frac{N\pi\alpha}{8}, \tag{3.9}$$

where $\alpha = {}^{e^2}/_{\hbar v_F \epsilon_s} = {}^{2.2}/_{\epsilon_s}$ is the effective Coulomb coupling constant of graphene in a dielectric environment characterized by ϵ_s. The single-layer screened electron-electron interaction follows from Eqs. (3.2) and (3.8):

$$V_q = \frac{2\pi e^2}{\epsilon_s \epsilon_4 q}, \tag{3.10}$$

where we have defined $\epsilon_N = 1 + {}^{N\pi\alpha}/_{8}$ to be the intrinsic dielectric constant of graphene. Here, as before, N denotes the number of fermion species. For a single-layer system, $N = 4$ owing to the spin and valley degeneracies. In double-layered structures, $N = 8$ due to the extra "which-layer?" degree of freedom. We note that in the latter case, however, the interband transitions cannot be absorbed into the potential in the same way as they were in (3.10). This will be explained in the following sections.

From Fig. 3.1 we see that the polarizability is constant ($\Pi_q = \Pi_0$, see Eq. (3.7)) for $q < 2k_F$. In the long wavelength limit, this leads to qualitatively similar screening behaviour as in 2DEG's with massive excitations [42,60]. The static dielectric function in the long-wavelength limit ($q \to 0$) reduces to the Thomas-Fermi dielectric function:

$$\epsilon(q) = 1 + \frac{N\alpha k_F}{q} = 1 + \frac{q_s}{q}, \tag{3.11}$$

where $q_s = N\alpha k_F = \frac{2\pi e^2}{\epsilon_s}\mathcal{D}(E_F)$ is the Thomas-Fermi screening wavevector. This gives, for the statically screened potential:

$$V_q = \frac{2\pi e^2}{\epsilon_s} \cdot \frac{1}{q + q_s}. \tag{3.12}$$

The screening length, $\lambda = 1/q_s$, is particularly long in graphene. In conventional metals, λ is of the order of 1Å. For monolayer graphene embedded in hBN doped to $|E_F| = 100\text{meV}$, $\lambda = 3\text{nm}$, so that interactions are long-ranged in graphene [56].

We have seen that the effective interaction takes on two different forms depending on the doping: for intrinsic graphene, $k_F = 0$ and we obtain Eq. (3.10), but for extrinsic graphene, $k_F \neq 0$, and we obtain Eq. (3.12) in the $q < 2k_F$ limit. In the position space, the $q = 0$ singularity in Eq. (3.10) leads to long-ranged interactions, which are screened as if by a dielectric:

$$V(r) = \frac{e^2}{\epsilon_s \epsilon_4 r}. \tag{3.13}$$

Conversely, the presence of doping means that the interaction can be screened by transitions within the same band, which enhances the polarizability at long wavelengths and suppresses the long-range ($q_s r \gg 1$) interactions:

$$V(r) \sim \frac{1}{q_s^2 r^3}. \tag{3.14}$$

Because the Fourier component of the interaction is suppressed by the monotonically increasing polarizability for large q (see Fig. 3.1), we have assumed that the $q < 2k_F$ regime dominates the interaction physics. In graphene, as in 2DEG's, a discontinuity in the polarizability leads to Friedel oscillations. This discontinuity is in the 2$^{\text{nd}}$ derivative (as opposed to the 1$^{\text{st}}$ derivative in 2DEG systems), leading to a suppression of Friedel oscillations, which go like $\sim {}^{\cos(2k_F r)}/_{r^3}$ in graphene. This will become important when we include the effects of doping in our analysis of the bi-electron in Chapter 4, as it means that we can assume the sample is homogeneously doped (rather than having local fluctuations in the charge density which could destroy the pairing).

We note in closing that, in order to approximate the screened potential using an intrinsic dielectric constant, we have assumed that the graphene is undoped and ungated ($k_F = 0$). Therefore, there would be no available phase space to support the pairing described in Chapter 2. On the other hand, we have assumed that Pauli blocking due to the Dirac sea does not occur, so that the metallic screening described by $\tilde{\Pi}_q^+$ needs to be taken into account. Resolving this conflict requires the treatment of an inherently many-body problem, and will occupy our attention for the remainder of this work.

3.2 Bare double-layered interactions

In this section, we derive the bare electron-electron interaction potential for the double layer nanostructure pictured in Fig. 2.3. We will see in Section 3.3 that the polarizability of graphene discussed above and the bare interactions to be derived here completely

define the double layer screened interaction potential. This result is not novel, indeed it has been given previously by many authors [31–33, 61–65], but is stated incorrectly in several of their papers [33, 62, 65]. Therefore, it is necessary to give a derivation here for completeness.

As the final form of the screened double-layer potential is simply stated without proof in most of those aforementioned papers, it is not clear at which point in the calculation those authors made the error. Thus, we start from the beginning and consider the case of two electrons which are free to move in parallel graphene monolayers. The layers are separated by a dielectric spacer of thickness d and relative permittivity ϵ_2. That structure is sandwiched between a pair of semi-infinite dielectrics, each of relative permittivity ϵ_1. A schematic of this setup is given in Fig. 2.3. We note that in what is to follow we assume that the z-axis points upwards in the plane of the page and is perpendicular to the graphene layers in that figure. Due to the thinness of graphene, it enters the picture through its screening properties only. Thus, the bare interactions are actually determined by the problem of a pair of charges which are pinned at the interfaces between the dielectric media, but free to move in the plane. We assume the lower interface is at $z = 0$ and the upper interface is at $z = d$, and employ the following naming conventions for the three regions partitioned by them: region 1 fills the space $z > d$, region 2 fills the space $0 < z < d$ and region 3 is the remainder, $z < 0$.

We begin by calculating the electrostatic potential, $\Phi(\boldsymbol{r}, z)$ due to the electron at $(\boldsymbol{r}, z) = (0, d)$, where $\boldsymbol{r}$ is the polar vector. We assume that we are in the Galilean limit so that the laws of electrostatics are valid because the Fermi velocity of charge carriers in graphene is much less than the speed of light: $v_F \ll c$ [66]. As none of the three regions contain any charge, the potential is determined by Laplace's equation, $\nabla^2\Phi(\boldsymbol{r}, z) = 0$. We choose to absorb the oscillatory part of the solution into the plane, to make the boundary conditions manageable so that in the regions $j = 1, 2, 3$

we obtain:

$$\Phi_j(\boldsymbol{r}, z) = \exp(i\boldsymbol{q}\cdot\boldsymbol{r})\left(\mu_j e^{qz} + \nu_j e^{-qz}\right). \tag{3.15}$$

where q is a constant arising from the separation of variables[1]. The constants μ_j and ν_j are different for the three regions, and are determined from boundary conditions. Setting the zero-point of the potential at $z = \pm\infty$ gives $\mu_1 = \nu_3 = 0$. Because the electron at the lower interface will enter the problem as a test charge in the potential energy function, the normal component of the displacement field $\boldsymbol{D}$ is continuous at $z = 0$. There is a discontinuity due to the charge at $z = d$, however, giving two more boundary conditions:

$$\begin{aligned}
(\boldsymbol{D}_1 - \boldsymbol{D}_2)\cdot\hat{\boldsymbol{z}}|_{z=d} = -4\pi e\delta(\boldsymbol{r})\delta(z-d) \quad &\rightarrow \quad \epsilon_2\mu_2 e^{qd} + (\epsilon_1\nu_1 - \epsilon_2\nu_2)e^{-qd} = -\frac{4\pi e}{q}, \\
(\boldsymbol{D}_2 - \boldsymbol{D}_3)\cdot\hat{\boldsymbol{z}}|_{z=0} = 0 \quad &\rightarrow \quad \epsilon_2\mu_2 - \epsilon_2\nu_2 - \epsilon_1\mu_3 = 0,
\end{aligned} \tag{3.16}$$

where we have used the standard relations $\boldsymbol{D}_j = \epsilon_j\boldsymbol{E}_j$ and $\boldsymbol{E}_j = -\nabla\Phi_j$ for the electric field ($\boldsymbol{E}$). We also enforce continuity of the potential across each interface, so that:

$$\begin{aligned}
\Phi_3(z=d) = \Phi_2(z=d) \quad &\rightarrow \quad \mu_2 e^{qd} + (\nu_2 - \nu_1)e^{-qd} = 0, \\
\Phi_2(z=0) = \Phi_1(z=0) \quad &\rightarrow \quad \mu_2 + \nu_2 - \mu_3 = 0.
\end{aligned} \tag{3.17}$$

Eqs. (3.16) and (3.17) determine the remaining constants which give us the potential in region 2, which is valid at both of the interfaces:

$$\Phi_2(\boldsymbol{r}, z) = -\frac{4\pi e}{q}\cdot\frac{\exp(i\boldsymbol{q}\cdot\boldsymbol{r})}{(\epsilon_1+\epsilon_2)^2 e^{qd} - (\epsilon_1-\epsilon_2)^2 e^{-qd}}\left[(\epsilon_1+\epsilon_2)e^{qz} + (\epsilon_1-\epsilon_2)e^{-qz}\right]. \tag{3.18}$$

We calculate the potential energy function by incorporating the second electron as a test charge at $z = 0$ with planar position $\boldsymbol{r}$ (since we assumed the first electron was

[1]It becomes clear that q is the magnitude of an in-plane wavevector $\boldsymbol{q}$ when one Fourier-transforms the separated equations.

at $\boldsymbol{r} = 0$): $V(\boldsymbol{r}) = -e\Phi_2(\boldsymbol{r}, 0)$. Its Fourier transform is given by:

$$v_{12} = \frac{2\pi e^2}{q} \times \frac{\epsilon_2}{f_2}. \tag{3.19}$$

By instead placing the test charge in the upper layer, we obtain the bare interaction for two electrons in the same layer:

$$v_{11} = \frac{2\pi e^2}{q} \times \frac{f_1}{f_2}. \tag{3.20}$$

In Eqs. (3.19) and (3.20) above, we have defined the following functions:

$$\begin{aligned} f_1 &= \exp(qd)\left[\frac{\epsilon_1 + \epsilon_2}{2}\right] - \exp(-qd)\left[\frac{\epsilon_1 - \epsilon_2}{2}\right], \\ f_2 &= \exp(qd)\left[\frac{\epsilon_1 + \epsilon_2}{2}\right]^2 - \exp(-qd)\left[\frac{\epsilon_1 - \epsilon_2}{2}\right]^2. \end{aligned} \tag{3.21}$$

It follows from symmetry that $v_{22} = v_{11}$ and $v_{21} = v_{12}$.

In the limit where the two graphene layers are on top of each other ($d \to 0$), the role of the central dielectric vanishes, and we regain the single layer interaction:

$$v_{11} = v_{12} = \frac{2\pi e^2}{\epsilon_1 q}, \tag{3.22}$$

which corresponds to the bare interaction of an electron pair for monolayer graphene in a dielectric environment characterized by ϵ_1. In the opposite limit ($d \to \infty$), the layers are fully decoupled, so that the interlayer potential vanishes, and the intralayer potential is that of a monolayer in the dielectric environment created by the two dielectrics it separates, $\kappa = {}^{(\epsilon_1+\epsilon_2)}/_2$:

$$\begin{aligned} v_{12} &\to 0, \\ v_{11} &= \frac{2\pi e^2}{\kappa q}. \end{aligned} \tag{3.23}$$

In the case where all three dielectrics are of the same type ($\epsilon_1 = \epsilon_2$), we recover the standard form of the intralayer potential from Eq. (3.22). The interlayer potential takes the form $v_{12} = v_{11}e^{-qd}$, which corresponds the standard double-layer Coulomb potential in real space:

$$V(r) = \frac{e^2}{\epsilon_1\sqrt{r^2 + d^2}}, \tag{3.24}$$

for electrons confined to parallel layers of separation d in a homogeneous dielectric environment.

3.3 Screened double-layered interactions

Let us now consider the effects of screening on the interlayer interaction. We begin by assuming the two layers have different polarizabilities, Π_1 and Π_2, which amounts to the layers not necessarily having the same carrier density. The presence of the two layers can be captured by representing the Dyson equation resulting from Eq. (3.1) as a matrix equation [62, 64, 67]. Thus, the screened interaction is given by

$$W = (1 + V\Pi)^{-1}V = V - V\Pi W, \tag{3.25}$$

where

$$V = \begin{bmatrix} v_{11} & v_{12} \\ v_{21} & v_{22} \end{bmatrix} \tag{3.26}$$

is the bare interaction (subscripts refer to layers 1 and 2; the matrix elements of V were all calculated in Section 3.2) and

$$\Pi = \begin{bmatrix} \Pi_1 & 0 \\ 0 & \Pi_2 \end{bmatrix} \tag{3.27}$$

represents the polarizabilities. We note that both off-diagonal elements in the polarizability matrix vanish because tunnelling between the layers is forbidden. By direct computation, we obtain:

$$W = \begin{bmatrix} v_{11}\Pi_1 + 1 & v_{12}\Pi_2 \\ v_{21}\Pi_1 & v_{22}\Pi_2 + 1 \end{bmatrix}^{-1} \begin{bmatrix} v_{11} & v_{12} \\ v_{21} & v_{22} \end{bmatrix} \tag{3.28}$$

$$= \frac{1}{(1+v_{11}\Pi_1)(1+v_{22}\Pi_2)} \begin{bmatrix} v_{11}(1+v_{22}\Pi_2) - v_{12}v_{21}\Pi_2 & v_{12}(1+v_{22}\Pi_2) - v_{22}v_{12}\Pi_2 \\ v_{21}(1+v_{11}\Pi_1) - v_{11}v_{21}\Pi_1 & v_{22}(1+v_{11}\Pi_1) - v_{12}v_{21}\Pi_1 \end{bmatrix}.$$

The off-diagonal elements of W are just the interlayer electron-electron potential. For all structures that we consider, $v_{11} = v_{22}$ and $v_{12} = v_{21}$. Thus, we obtain:

$$W_{12} = W_{21} \equiv U_q = \frac{v_{12}}{(1+v_{11}\Pi_1)(1+v_{11}\Pi_2) - v_{12}^2\Pi_1\Pi_2}. \tag{3.29}$$

Let us focus on the case of the homogeneous dielectric environment (so that $\epsilon_1 = \epsilon_2 \equiv \epsilon_s$). In that scenario, $v_{11} = v_q$ and $v_{12} = v_q e^{-dq}$. We will show below that at the relevant distances the filling of the bands is not important, so that we use the approximation $k_F = 0$ for both layers (where, for example, k_F in layer one refers to the momentum, relative to the Dirac point, of a state at the *local* Fermi energy of layer one). Then $\Pi \equiv \Pi_{1,2} = \frac{Nq}{16\hbar v_F}$ (see Section 3.1 for details). Note that the Fermi energy can be tuned by the application of a gate voltage in graphene, so we are free to assume that the layers have equal carrier concentrations if we choose. The interaction then takes the form:

$$V_q = \frac{v_q e^{-dq}}{(1+v_q\Pi)^2 - v_q^2\Pi^2 e^{-2dq}} \tag{3.30}$$

$$= \frac{v_q e^{-dq}}{1 + 2\frac{N\pi\alpha}{8} + (\frac{N\pi\alpha}{8})^2[1 - e^{-2dq}]}. \tag{3.31}$$

Now let us turn to the determination of the intrinsic dielectric constant of graphene, when there are two layers. To justify the choice of $k_F = 0$ we note that the behaviour

of $V(r)$ at distances $k_F r \lesssim 1$ is determined by $q > k_F$ where the exact value of k_F is not important. As we are most interested in the behaviour at small distances, $k_F = 0$ is a reasonable first treatment of the two-body problem. This is a far more realistic approach than naïvely using the bare interaction, which results in unrealistically high binding energies.

At small distances, $q \gg \frac{1}{d}$, the potential takes the form:

$$V_q \sim \frac{v_q e^{-dq}}{1 + 2\frac{N\pi\alpha}{8} + \left(\frac{N\pi\alpha}{8}\right)^2} = \frac{2\pi e^2}{\epsilon_s \epsilon_N^2 q} e^{-dq}. \tag{3.32}$$

The inverse Fourier transform is then a first approximation to the inter-layer potential in position space:

$$V_r \sim \frac{e^2}{\epsilon_s \epsilon_N^2 \sqrt{r^2 + d^2}}, \tag{3.33}$$

which is the form used to approximate the bound state energies in this work.

At intermediate distances $d \ll r \ll \lambda_F$, however, the potential takes a slightly different form:

$$V_q \sim \frac{v_q e^{-dq}}{1 + 2\frac{N\pi\alpha}{8}} = \frac{2\pi e^2}{\epsilon_s \epsilon_N q} e^{-dq}, \tag{3.34}$$

where ϵ_N is defined in the same way as it was in the discussion above, but with $N = 8$. We note the contribution of the two layers in Eq. (3.34), resulting in an extra "which-layer" degree of freedom.

As discussed above, we have presented the derivation of the screened double-layer interaction in full detail because it was given incorrectly in the literature [33, 62, 65]. Although the potential has been given correctly by other authors [61,63,64], the absence of complete arguments in those papers mean that one has no immediate reason to accept one result over another. We will now argue that the result we have given in Eq. (3.29) is indeed the correct one.

Firstly, Hosono *et al* gave a definition of the multi-component screened interaction which was not self-consistent: $W = V + V\Pi W = V(1 - V\Pi)^{-1}$ (see Eq. (8) in Ref. [62]). Let us contrast this with the form we gave in Eq. (3.25). In principle, one can convert our definition into theirs, $V + V\Pi W \to V - V\Pi W$, by absorbing the extra minus sign into the definition of the polarizability Π. We note, however, that Hosono *et al* did *not* absorb the extra phase into the polarizability in this way (instead, they used the polarizability of Ref. [42], as we did. See Eq. (10) in Ref. [62]). The second error arises in the Dyson-summed form of their definition: $W = V(1 - V\Pi)^{-1}$. We note that this is not equivalent to $W = (1 + V\Pi)^{-1}V$, even ignoring the phase we mentioned above, because W and V do not commute for $\Pi_1 \neq \Pi_2$. The form given by us in Eq. (3.25) follows directly if one remembers that the objects involved are matrices, and obey non-commutative algebra. Upon performing the diagrammatic expansion of Eq. (3.1) we obtain:

(3.35)

up to third order in the bare interaction. Upon performing the corresponding expansion of our definition of the screened interaction in the algebraic form:

$$W = (1 + V\Pi)^{-1} V = V - V\Pi V + V\Pi V\Pi V - ..., \tag{3.36}$$

which correctly captures the ordering of the bare potential and the bare bubbles as in Eq. (3.35). Expanding the definition of Hosono *et al*, however:

$$W = V (1 - V\Pi)^{-1} V + V^2\Pi + V^2\Pi V\Pi + ..., \tag{3.37}$$

which does not reflect the non-commutativity of V and Π and leads to nonsensical diagrams. The arguments those authors gave previously, and the results obtained thereafter, were correct however, and so we assume this was a typographical error.

Secondly, Abergel *et al* gave the following result (see Eq. (2) of Ref. [33]):

$$U_A = \frac{v_q e^{-qd}}{1 + 2v_q(\Pi_1 + \Pi_2) + v_q^2 \Pi_1 \Pi_2 (1 - e^{-2qd})}, \tag{3.38}$$

which differs from our result by the factor of 2 in the denominator. The interaction U_A effectively over-counts the number of fermion flavours. To see this, we set $\Pi_1 = \Pi_2$ and take the harsh limit $d \to 0$, so that the two layers are directly on top of each other. For our result, Eq. (3.29), as well as for Ref. [33], we obtain:

$$U_q = \frac{2\pi e^2}{\epsilon_s \epsilon' q}. \tag{3.39}$$

where, for our result, $\epsilon' = \epsilon_8$, but for that of Abergel *et al* $\epsilon' = \epsilon_{16}$. In the correct case $N = 8$ fermion species have arisen due to two projections of the real spin, two valleys and two layers (although the layers occupy the same space in this limit they are both there, in the formal sense). The doubling of the fermion species to $N = 16$ cannot be accounted for.

Finally, Kharitonov *et al* gave the following result for $\Pi_1 = \Pi_2$ (see Eq. (5) in Ref. [65]):

$$U_K = \frac{v_q e^{-qd}}{1 + 2v_q \Pi + \Pi^2 v_q^2 (1 - e^{-qd})}, \tag{3.40}$$

which differs from our result by the factor of two in the exponential term in the denominator. One can see the error by recalling that the exponential factors arise due to the bare inter-layer interaction. We assume those authors made the following arithmetic error: $v_{12}^2 = (v_q e^{-qd})^2 \stackrel{?}{=} v_q^2 e^{-qd}$.

3.4 Short-ranged interaction approximation

In this section, we will explain how the screened interaction in graphene can be modelled by a short ranged potential $V(\boldsymbol{r}) = \lambda \delta(\boldsymbol{r})$, and determine the strength of the interaction,

λ. We begin with the case of a graphene monolayer in an environment of dielectric constant κ. If $\Pi(q=0) \neq 0$, within the random phase approximation, the effective electron-electron interaction $U_{\boldsymbol{q}}$ is given by Eq. (3.2). For sufficiently small momenta, $q \ll q_s$, the potential U_q can be approximated by a short-ranged potential $V(\boldsymbol{r}) = \lambda\delta(\boldsymbol{r})$, where $\lambda = U_{q=0}$ and q_s is the inverse screening radius. We can therefore write down the interaction strength, $\lambda = U_{\boldsymbol{q}=0}$, for a single-layer system:

$$\lambda = \frac{2\pi v_F \alpha}{q_s}, \tag{3.41}$$

where $q_s = N\alpha p_F$ is the Thomas-Fermi screening momentum of electrons in graphene.

Let us now turn to the case of two layers separated by a dielectric spacer of thickness d. We assume that the device is fully embedded in the same dielectric material. The case of a dielectric spacer between the layers with permittivity different from that of the environment is treated below. Assuming the electrons are in opposite layers, the potential takes the form of Eq. (3.30). We also restrict ourselves to the simplest case where the local Fermi levels of the two layers are independently tuned to the same value, so that $\Pi_1 = \Pi_2 \equiv \Pi$. Following the reasoning applied to the single-layer case above, we obtain for the interaction strength:

$$\lambda = \frac{\pi v_F \alpha}{q_s(1 + q_s d)}. \tag{3.42}$$

Let us reiterate that we have focussed our attention on the simplest case of equal doping, when $\Pi_1 = \Pi_2$. Because the pairs reside in different bands and have opposite momenta relative to the Dirac point, the limiting role is played by the layer which hosts the lower-cone electron (which we will now call layer 1, without loss of generality). Clearly Fermi statistics does not change the problem at all for any level of hole doping in layer 2, as the necessary phase space is always free for an electron in the upper cone: all that is required is $E_{F,2} \leq 0$. On the other hand, the form of Eq. (3.29) suggests that inequivalent doping might significantly change the strength of the interlayer potential.

Let the local Fermi energies of layers 1 and 2 be given by E_F and $E_F - \delta E_F$, respectively, where $E_F < 0$ and $\delta E_F > 0$. The interaction strength is then given by:

$$\lambda(\delta E_F) = \frac{\lambda(0)}{1 + \frac{\delta E_F}{|E_F|}\left[\frac{q_s d + \frac{1}{2}}{q_s d + 1}\right]}. \tag{3.43}$$

We therefore conclude that our results are relevant for a range of doping regimes, so long as $|E_{F,1} - E_{F,2}| \ll |E_{F,1}|$.

In the above analysis, it was assumed that the dielectric material used to encapsulate the two layers was the same as that which separated them (i.e. $\epsilon_1 = \epsilon_2$ in Fig. 3.2). Let us now consider the case where the inter-layer spacer (with dielectric constant ϵ_2) is a different material to the encapsulating dielectrics (which have dielectric constant ϵ_1). The device in question is shown in Fig. 2.3, for $\epsilon_1 \neq \epsilon_2$. Let us now calculate the interaction strength which is applicable to the results for suspended double-layered systems, which corresponds to $\epsilon_1 = 1$ (the role of the outer dielectrics being played by vacuum) and $\epsilon_2 = 3.9$ (for a hBN spacer). We find that the interaction strength is governed by the permittivity of the spacer, and has the same form as it did in the $\epsilon_1 = \epsilon_2$ case (see Eq. (3.42)).

The screened inter-layer interaction for the case of a non-trivial dielectric environment was given in Eq. (3.29). It is not immediately obvious which of the dielectrics is most important in determining the screening behaviour. Taking the limit of $q \to 0$, we obtain the interaction strength:

$$\lambda = U_{q=0} = \frac{\pi e^2}{q_b + \frac{q_b^2 d}{\epsilon_2}}, \tag{3.44}$$

where $q_b = N\alpha_b p_F$ is a kind of "bare screening radius" determined by the bare coupling constant: $\alpha_b = e^2/v_F$. Thus, the material used to encapsulate the double-layered structure does not play a role in determining the strength of the momentum-independent interaction $V(r) = \lambda\delta(r)$. We therefore define the Coulomb coupling constant to be

$\alpha = e^2/\epsilon_2 v_F$, which in turn implies that $q_s = q_b/\epsilon_2$, and obtain

$$\lambda = \frac{\pi v_F \alpha}{q_s(1 + q_s d)}, \tag{3.45}$$

for $q_s d \gg 1$. This brings λ to the form given by Eq. (3.42), so that ϵ_2 does indeed play the role of the effective dielectric constant.

Naïvely, one might expect the interaction strength to be determined by the outer dielectrics, ϵ_1, because it is through these layers that most of the electric field lines pass in the case of bare interactions (see Fig. 3.2a). In fact, the result arises due to metallic screening of the interaction in the two graphene layers, which leads to charge compensation within a screening cloud of radius $1/q_s \sim 1$Å, so that the in-plane separation of the two electrons is very small: $r \ll d$. Because the charge is compensated, almost all electric field lines will begin on one electron and terminate on its surrounding ionic cloud. Occasionally, however, an electric field line will "leak out" leading to a relatively weak coupling mediated through the inter-layer region, of dielectric constant ϵ_2 (see Fig. 3.2b). The two electrons therefore interact directly through the middle dielectric. This can be seen by taking the limit $d \to 0$ in Eq. (3.45), which formally removes the spacer from the problem. In that limit, λ does not depend on either of the two permittivities.

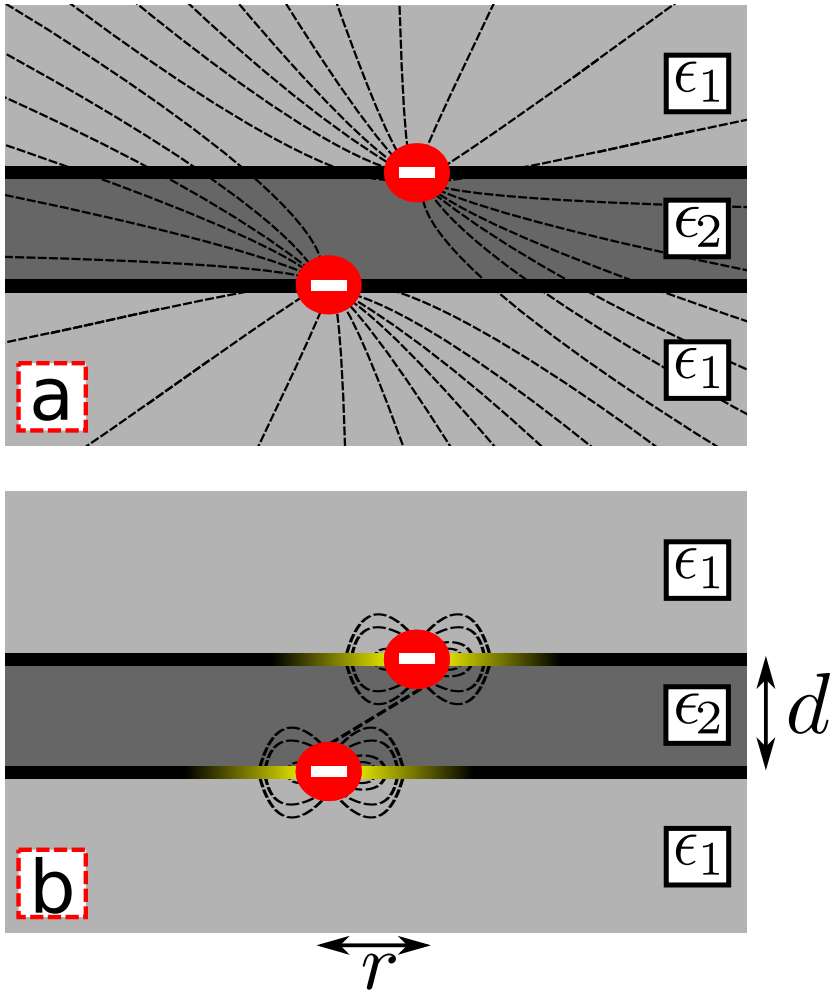

Figure 3.2: Schematic of the inequivalent dielectric double-layer. Two graphene layers are separated by a dielectric spacer of permittivity ϵ_2 and thickness d. The double layer is encapsulated in a second dielectric material, which has permittivity ϵ_1. The layers host a pair of electrons (red circles) which have in-plane separation r. a) In the absence of screening by the electron sea, most of the electric field lines pass through the outer dielectrics and the interaction is mostly determined by the dielectric constant of the environment, ϵ_1. b) When screening is considered, the electron charge is compensated by a positive screening cloud (yellow) within each graphene layer. The majority of the field lines now terminate on the screening charge, and the resulting (weak) interaction propagates through the middle dielectric. Hence, the interaction becomes sensitive to the value of the dielectric constant of the spacer, ϵ_2.

Chapter 4

Effects of the Dirac sea: screening and Pauli blocking

4.1 Introduction

It is instructive to compare the interaction effects described in Chapter 2 to other, more familiar condensed matter systems. In semiconductors at low doping, attractive interactions result in binding between electrons near the bottom of an empty conduction band and holes near the top of a filled valence band, separated by a gap. When the concentrations of electrons and holes are sufficiently low, one can ignore the effects of Fermi statistics and describe the excitons in terms of two constituent massive particles. The resulting energy levels are dependent on dimensionality and the details of the interaction. In contrast to this, metals admit low-energy excitations which involve transitions between electron states near the Fermi level within the same band. Most of these transitions are blocked due to the Pauli exclusion principle, which may result in low-temperature anomalies and, eventually, the formation of strongly correlated phases such as ferromagnets, charge density waves, etc. The details of such transitions depend upon the interaction between the electrons, as well as the structure of the single particle spectrum. In the case of a weak attractive interaction and flat density of states, the restrictions arising from Pauli blocking can result in the formation of a bound state

known as a Cooper pair, irrespective of the dimensionality. The many-body physics of graphene does not fit neatly into either of the scenarios above. On the one hand, monolayer graphene is gapless, so that elementary excitations cannot be thought of as entirely separate from the sea of free carriers, as they can be in semiconductors. On the other hand, the density of states is linear, and vanishes near the charge-neutrality point. Therefore, graphene (near $E_F = 0$) can not be considered to be a metal, either (for a full discussion see, e.g., Ref. [56]). Further, due to the linear dispersion, the Coulomb coupling constant is independent of the density of free carriers, and electron-electron interactions are important irrespective of the doping. This is not the case for a two-dimensional electron gas with parabolic dispersion [56]. It is therefore unclear whether the two-body problem will necessarily stand on its own or, e.g., be valid for only some (if any) doping regimes when the effects of the Dirac sea are taken into account. Thus, it is desirable to incorporate the effects of Pauli blocking and screening into the two-body problem of an interacting electron-electron pair.

In this chapter, we show that the electron-electron pairs which form in the subspace of non-dispersing two-particle states have their energies renormalized by many-body effects. We study the two most important many-body phenomena at zero temperature: screening of the interaction by free carriers in the Dirac sea, and Pauli blocking, in which scattering into single-particle states below the Fermi level is forbidden due to the Pauli exclusion principle. We show that the problem admits an analytic solution when the interaction is short-ranged (in the subspace of states where the trigonal warping is compensated). We then treat the complete problem, with bandstructure warping and screened interaction potential, numerically. For both single- and double-layered structures we find good agreement between numerical results and our exact solution which is applicable over a range of experimentally realizable doping configurations.

The rest of the chapter will have the following structure. In Section 4.2 we naïvely impose restrictions of Pauli blocking on the wavefunction and show that this can lead to pairing for any level of hole doping. We provide a simple heuristic model in which

the subspace of states where trigonal warping is not important are studied. We show that this model has an analytic solution when the interaction potential is sufficiently short-ranged. In Section 4.3 we discuss the role of screening in determining the binding energies, using the interaction strengths derived for single- and double-layer systems in Section 3.4. We show that the screening is vital for accurately determining the binding energies in systems near $E_F = 0$, and exponentially suppresses the binding when the system is heavily doped. We note that this approach is not fully rigorous, and is based on a naïve (but intuitive) imposition of the phase space restriction on the pair wavefunction. Therefore, in Sections 4.5 and 4.4 we take the more rigorous approach by treating the Bethe-Salpeter equation in detail. In doing so, we not only develop a more general formal theory which includes the effects of finite-ranged interactions and trigonal warping of the dispersion, but also show that the heuristic model of Section 4.2 is nothing but a representation of the Bethe-Salpeter equation in the sector of para-states with short-ranged interactions. In Section 4.7 we discuss the results of numerical calculations of the binding energies of pairs, including the effects of trigonal warping and momentum-dependent interaction neglected previously. We find that the numerical results agree with our analytical solutions in the low-doping regime, where the binding energies are proportional to the Fermi energy [68].

4.2 Analytical solution for short-ranged interaction

A formal treatment of electron-electron pairing which includes the effects of the Dirac sea requires the solution of the Bethe-Salpeter equation. We will perform that calculation in detail in the sections that follow, but it is helpful to first treat a heuristic model which incorporates the most important many-body effects in a simple way.

It is instructive to first recall the case of a two-dimensional massive particle in a short-ranged potential $V(\boldsymbol{r})$ of interaction radius a. For a weak potential, the bound state is shallow, and the wavefunction is concentrated at the distances $r \gg a$. Therefore, it is possible to approximate the potential by a delta function, $V(\boldsymbol{r}) \approx \lambda\delta(\boldsymbol{r})$,

where $\lambda = 2\pi \int V(\boldsymbol{r}) r dr$ is the interaction strength. This gives the binding energy in the form [40]:

$$|E| \sim E_c \exp\left\{-\frac{2\pi\hbar^2}{m\lambda}\right\}. \tag{4.1}$$

The prefactor $E_c \sim \hbar^2/ma^2$ represents the energy cut-off which is determined by the behaviour of $V(\boldsymbol{r})$ at distances $r \sim a$. Thus, it shows that the model with a delta-like potential is incomplete, and has to be regularized at short distances in a non-universal way. Therefore, Eq. (4.1) is only applicable for $\lambda \ll 2\pi\hbar^2/m$, so that the binding energy is determined by the universal exponentially small factor. Since the dynamics of the electron-electron pair is governed by quadratic kinetic energy, the bound state in this problem has similar properties. However the regularization is now provided by the momentum space cut-off at $p = p_F$, rather than the interaction radius a, as explained below.

In finding the binding energy of the pair, we begin with two natural assumptions: (i) that the free carriers in the system screen the electron-electron interaction to the extent that it can be considered short-ranged (see Section 3.4), and (ii) transitions into paired states in which at least one of the electrons is below the Fermi level are blocked by the Pauli exclusion principle [69]. In the limit of large hole doping, the interaction is suppressed for distances $rp_f \gtrsim 1$, so as a first approximation we assume that the electron-electron interaction takes the form $V(\boldsymbol{r}) = \lambda\delta(\boldsymbol{r})$, where λ determines the strength of the interaction which is different for single- and double-layered systems. We note that this is just the case treated in Section 3.4. Our second assumption is equivalent to only allowing contributions of momenta in the range $0 < p < p_F$. We will show that, subject to these assumptions, the problem admits an analytical solution. We explained above that models with a delta-like potential can be incomplete, requiring regularization at short distances in a non-universal way. However, in this case the regularization is provided by the momentum space cut-off $p = p_F$, rather than the interaction radius a. We will show below that this leads to an exact solution for the

binding energy of the bi-electron, as opposed to the approximate solution of Eq. (4.1). Not only does this cut-off extend the range of validity of the solution to $\lambda \gtrsim 2\pi\hbar^2/m$, we will show below that it is vital if one is to correctly determine the low-doping behaviour of the system.

We note that the presence of a Fermi surface also plays an important role in superconducting pairing [70]. Cooper noted that a pair of electrons interacting above the Fermi sphere with net attractive interaction (due to the presence of electron-electron as well as electron-phonon interactions) would form a bound state with the same qualitative properties as the carriers in conventional superconductors [70]. In that case, wavefunction regularization was provided by the Fermi surface and the Debye cut-off, with the density of states near the Fermi level playing a dominant role in the determination of the binding energies. A bound state does not necessarily exist in three spatial dimensions for a particle in a shallow well [40], so that in the superconducting case, the Fermi surface plays a critical role in enabling the pairing. For bi-electrons in graphene, however, we will see that the Fermi surface suppresses the pairing, especially when the doping is low (when $p_F \to 0$ in Eq. (4.6)).

We consider the subspace spanned by para-states, so that the two-particle wavefunction is given by $\Psi = \sum_{|\boldsymbol{p}|<p_F} \psi_{\boldsymbol{p}} \, |2, \phi_{\boldsymbol{p}}\rangle$. In this case the kinetic energy is isotropic and there is a trivial overlap of states with different momenta [37]. The Pauli exclusion principle requires that no two electrons may occupy the same quantum state [69], so that (at zero temperature) if the Dirac sea occupies every state of energy $E < E_F$, the electrons in the pair cannot be in any configuration which requires either of the two constituent particles to be below the Fermi level. Thus, to include the effects of Pauli blocking by the Dirac sea, we explicitly remove all transitions which involve the scattering of one of the particles to a state below the Fermi level. Further, we assume that the deformation of the valence band due to trigonal warping is not important, so the Fermi surface can be approximated by a circle of radius p_F. Within the momentum representation, the Schrödinger equation subject to this constraint takes the form (from

now on we choose $\hbar = 1$):

$$-\frac{p^2}{2m^*}\psi_{\boldsymbol{p}} + \iint\limits_{|\boldsymbol{p}'|<p_F} U_{\boldsymbol{p}-\boldsymbol{p}'}\psi_{\boldsymbol{p}'}\frac{d^2p'}{(2\pi)^2} = E\psi_{\boldsymbol{p}}. \tag{4.2}$$

Note that we also impose the restriction $|\boldsymbol{p}| < p_F$ in Eq. (4.2). The short-ranged potential is described by a momentum-independent interaction, $U_{\boldsymbol{p}-\boldsymbol{p}'} = \lambda$, which can be taken outside of the integral. Because the integral is independent of the momentum $\boldsymbol{p}$, we denote it as:

$$A = \iint\limits_{|\boldsymbol{p}'|<p_F} \psi_{\boldsymbol{p}'}\frac{d^2p'}{(2\pi)^2}, \tag{4.3}$$

which plays the role of a separation constant for the integral Eq. (4.2). Thus, the form of the wavefunction $\psi_{\boldsymbol{p}}$ follows directly from Eq. (4.2):

$$\psi_{\boldsymbol{p}} = \frac{A\lambda}{E + \frac{p^2}{2m^*}}. \tag{4.4}$$

In order to determine the energy E, we note that the definition of A, Eq. (4.3), plays the role of a self-consistency relation for the wavefunction. Therefore, we need to substitute $\psi_{\boldsymbol{p}}$ from Eq. (4.4) into Eq. (4.3):

$$1 = \frac{\lambda}{2\pi}\int_0^{p_F}\frac{p'dp'}{E + \frac{p'^2}{2m^*}} = \frac{\lambda m^*}{2\pi}\ln\left[\frac{p_F^2}{2m^*E} + 1\right]. \tag{4.5}$$

One then needs only to rearrange Eq. (4.5) for E, giving the binding energies of the form:

$$E = \frac{p_F^2}{2m^*} \times \frac{1}{\exp\left(\frac{2\pi}{m^*\lambda}\right) - 1}. \tag{4.6}$$

Let us note the role played by the limits of the momentum space integral in determining the right hand side of Eq. (4.5). The integral is carried out over the interval $p' \in$

$[0, p_F]$ because Pauli blocking strictly forbids transitions of electrons to occupied states. Therefore, at zero temperature, the sharpness of the Fermi surface has removed the need for any non-universal regularization of the binding energies in position-space and the model is exactly solvable. As discussed above, this was not the case for the result in Eq. (4.1) [40]. For one particle in a shallow well, the solution is known by the order of magnitude only, with the prefactor being determined by the details of the profile of $V(r)$ at short distances. In the presence of many-particles, however, the cut-off is given by the Fermi-Dirac sea, and is known exactly. We can see this by identifying Eq. (4.3) with the inverse Fourier transform of $\psi_{\boldsymbol{p}}$, evaluated at the origin: $\Psi(\boldsymbol{r} = 0)$. Thus, the wavefunction is regularized by the precise value $\boldsymbol{r} = 0$ in contrast to the imprecise length scale $r \sim a$, as was the case in determining Eq. (4.1) [40]. If we remove the phase space restriction from the definition of A we lose the self-consistency of our approach: the integral in Eq. (4.5) diverges and one has to resort to the approach of Ref. [40], as discussed above.

For a repulsive potential, $\lambda > 0$, the energies are positive definite. Further, the pairs are only destroyed by many-body effects in two limits: $p_F \to 0$ (the neutrality point, when the phase space is full and all pairing is blocked) and $\lambda \ll 2\pi/m^*$ (the limit of the ultra-dense hole gas, in which screening fully suppresses the interaction at all length scales). The states are therefore not destroyed for any systems of experimental interest. We note that in the latter case, the assumption of high doping exponentially suppresses the binding energies:

$$E \sim \exp\left(-\frac{2\pi}{m^*\lambda}\right), \tag{4.7}$$

and we regain the behaviour of the single particle in a shallow well (see Eq. (4.1)). This is to be expected as the limit of high (hole) doping corresponds to the removal of the Fermi-Dirac sea.

Eq. (4.6) can be understood as the product of two factors which compete to determine the binding energy. The first factor, which scales as $\sim p_F^2$, arose in our calculation

due solely to the momentum cut-off in the integral Eq. (4.2), and can therefore be understood as the contribution of Pauli blocking to the pairing. As the system is tuned towards the charge neutrality point from below, $E_F \to 0^-$, the phase space available to accommodate pairs in the channel $\boldsymbol{p}_1 = -\boldsymbol{p}_2$ shrinks, and the binding is suppressed as $p_F \to 0$. The second factor depends on λ and is therefore governed by the strength of the interaction. In the next section we will show that, $\lambda \sim p_F^{-n}$, so that for both cases of interest (monolayer ($n = 1$) and double-layer ($n = 2$) systems) it leads to an exponential suppression of the binding energy for large p_F.

4.3 Doping dependence of the binding energies

To understand the doping dependence of the binding energies from Eq. (4.6), we now discuss the dependence of the potential strength $\lambda \equiv \lambda(E_F)$ on the Fermi energy. We note that only the repulsive Coulomb interaction is considered in this thesis. This is in contrast to, e.g., the case of traditional superconductivity, in which the repulsive Coulomb interaction is not sufficient to cause pair binding, and the Hamiltonian must be extended by the attractive electron-phonon interaction. Because the kinetic energy of the pair is negative-definite and parabolic in the momentum, binding occurs for an arbitrarily weak repulsive interaction [37] in two dimensions in analogy with the case of a massive particle in an arbitrarily shallow well, which has been shown to exhibit at least one bound state in, e.g., Ref. [40].

We begin with the case of a graphene monolayer in an environment of dielectric constant κ. In that scenario, λ is given by Eq. (3.41). The binding energy of the pair is plotted in Fig. 4.1a. We see that as the doping increases the interaction strength λ decreases, so that the binding becomes weak at large doping. Let us introduce the crossover scale by setting the argument of the exponential factor in Eq. (4.6) to unity. This occurs when the magnitude of the Fermi energy is of the order of $E_s \equiv m^* v_F^2/N \sim 1\text{eV}$. In the limit of high doping ($|E_F| \gg E_s$) the binding energies are

exponentially suppressed:

$$E \sim \exp\left(-\frac{|E_F|}{E_s}\right), \tag{4.8}$$

but we note that this suppression would be hard to observe, due to the large doping required: $|E_F| \gtrsim 1\text{eV}$. Hence, only the limit $|E_F| \ll E_s$ is discussed below.

Let us now turn to the case of two layers separated by a dielectric spacer of thickness d. We assume that the device is fully embedded in the same dielectric material. The case of a dielectric spacer between the layers with permittivity different from that of the environment is treated below. Here we restrict ourselves to the simplest case where the polarizabilities of the two layers are the same: $\Pi_1 = \Pi_2 \equiv \Pi$. This is equivalent to the assumption that the Fermi levels of the two layers are tuned to the same value: $E_{F,1} = E_{F,2}$. Under these conditions, the interaction strength is given by Eq. (3.42). Thus, the crossover to weak binding in the double-layer case occurs at a different Fermi energy, E_d, which for inter-layer separation $d \gtrsim 1\text{nm}$ is given by $E_d = v_F/2\alpha N d \sim 0.1\text{eV}$. The fact that $E_d < E_s$ is due to the large minimum separation of two particles when they are confined to separate layers: even when the in-plane distance between the electrons is zero, they are still separated by $d \sim 1\text{nm}$. In the limit of high doping ($|E_F| \gg E_d$) the binding energies are again exponentially suppressed:

$$E \sim \exp\left(-\frac{E_F^2}{E_s E_d}\right), \tag{4.9}$$

We therefore expect screening to be the limiting factor in the binding energy for large p_F. The binding energies of the pair for such a double-layer structure are plotted in Fig. 4.1b.

On the other hand, the Coulomb interaction is only weakly screened in graphene doped near the neutrality point, $|E_F| \ll E_d \ll E_s$. As noted above, Pauli blocking is particularly important in this regime, giving a contribution $\sim p_F^2$. Nevertheless,

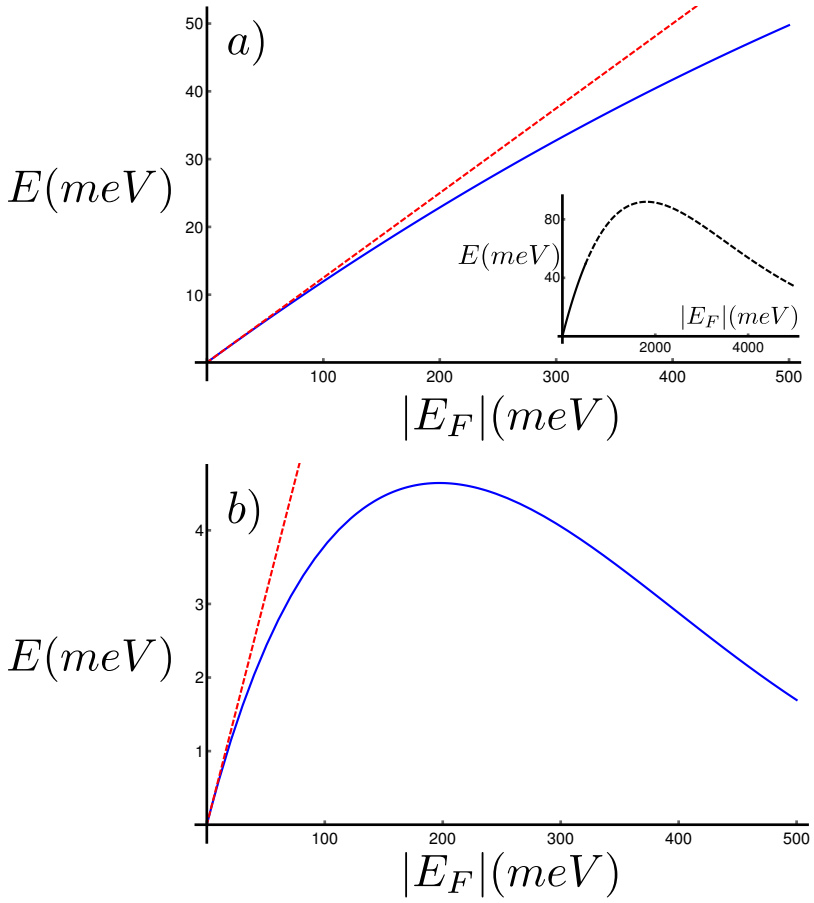

Figure 4.1: Analytic solutions for the binding energies of the pair in (a) single-layer and (b) double-layer structures. Solid blue lines represent the energies of Eq. (4.6). Dashed red lines represent the low-doping approximation of Eq. (4.10). In both cases, we assume the structure is embedded in hBN (in the double-layer case the dielectric spacer is also hBN). Both large graphs are plotted over doping range of experimental interest, and the inset to (a) shows the exponentially suppressed energies at unrealistically high doping. In the inset, only the solid line segment corresponds to the experimentally realistic regime.

screening does reduce this suppression for finite negative doping, leading to binding energies which are linear in the Fermi energy:

$$E = \frac{p_F^2}{2m^*} \cdot \frac{m^*\lambda}{2\pi} = \frac{1}{2Nn}|E_F|, \tag{4.10}$$

where $n = 1, 2$ is the number of graphene layers. We note the role of the exact cut-off momenta of Eq. (4.2): they prevent the binding energies from becoming singular as $E_F \to 0^-$.

We postpone further discussion of the analytical results obtained thus far until we introduce the effects of finite screening length and band warping. Indeed, so far we have assumed that the potential was delta-like and that the only effect of the Pauli exclusion principle is to prohibit transitions to states below the Fermi level. Although the latter seems like a reasonable assumption, we have not proved it. Further, we have limited ourselves to the subspace spanned by the para-state. To treat the more general system, we will need to resort to a numerical analysis. It is first necessary to extend the theory to include the fully screened single- and double-layer electron-electron interactions, with finite range, and also the effects of trigonal warping, not only to include the contributions of ortho-states, but also to account for a non-circular Fermi surface and the resulting non-trivial Pauli blocking. All of the above can be addressed by solving the Bethe-Salpeter equation, which we will consider in the following section.

4.4 Bethe-Salpeter equation and ladder approximation

In this section, we include the effects of the Dirac sea into the problem of electron-electron pairing in graphene, focusing on the case of zero temperature. This requires a significant development of the theory, which will occupy our attention throughout this section, as well as Sections 4.5 and 4.6. In the many-body theory, the two-particle problem is studied within the formalism of the Bethe-Salpeter equation (for a discussion see, for example, Refs. [71–74]). For example, the Bethe-Salpeter (BSE) equation can be used to treat the case of an electron-hole pair (exciton) in the context of excitonic condensation. The BSE is typically solved to obtain the two-particle propagator Γ, the poles of which correspond to the bound states of the pair in the same way that the poles of the single-particle propagator correspond to the quasiparticle excitations of the system [71,72]. Γ is the sum over ladder diagrams, and can be written in the equivalent and more-convenient form:

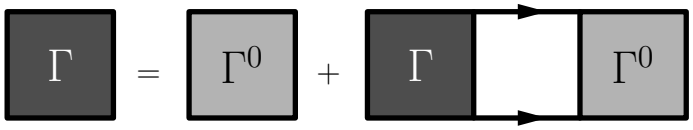

(4.11)

Let us explain the meaning of the diagrammatic elements of Eq. (4.11). The solid arrows represent free particle propagators, which point in the same direction because we are working in the electron-electron channel (antiparallel arrows correspond to the electron-hole channel). The block labelled Γ is the electron-electron scattering amplitude representing a sum over ladder diagrams, and plays the role of the two-particle propagator as discussed above. Finally, the block Γ^0 is the sum over all irreducible diagrams with dressed interaction lines:

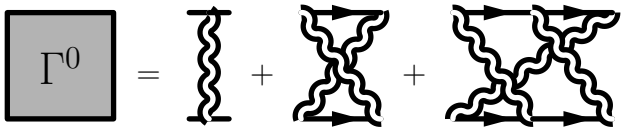

(4.12)

To leading order in momentum, electrons in graphene travel with velocity $v_F = c/300$, and so it is sufficient to ignore retardation effects and treat the bare interaction as instantaneous (i.e., the dielectric function takes the form $\epsilon(\boldsymbol{q}, \omega) = \epsilon(\boldsymbol{q}, 0)$). There could be extra retardation, however, due to a frequency dependence of the pair bubble. Physically, such a frequency would correspond to the time it takes for the electron sea to become polarized. We note, however, that the static limit of the polarizability is given by $\omega \ll v_F q$ (see, for e.g., Ref. [56]). One can motivate the static limit by assuming that the frequency is of the order of the binding energy of the pair: $\omega \sim E_b$. On the other hand, we know that the pairs have a small radius, so that we might assume a typical momentum scale is $q \sim p_F$. Therefore, the static approximation is valid when the binding energy is smaller than the Fermi energy (which is the case, see Fig. 4.1). Therefore, we will work within the static approximation throughout. In this case, all diagrams in Eq. (4.12) containing crossed interaction lines involve frequency integrals with poles in the same half plane for particles of the same species, and therefore vanish exactly. Therefore, there is only one irreducible part with non-trivial contribution in

Eq. (4.12), which takes the form $\Gamma^0 \sim U_{\boldsymbol{p}-\boldsymbol{p}'}$.

The BSE in Eq. (4.11) provides a natural way to extend the theory to incorporate the effects of the Fermi-Dirac sea: we simply interpret the electron propagators as causal propagators (which only allow us to propagate electrons above the Fermi level) and use the dressed interaction lines, as introduced in Eq. (4.12), to take account of screening.

One might wonder why we do not include any other effects (such as dressed single-particle propagators or dressed vertices) in our analysis. Let us explain why such extensions are not important. The nature of quasiparticles in intrinsic and extrinsic graphene has been studied by various authors (for a review see, for example, Ref. [56]). The self energy of electrons was studied by Das Sarma *et al*, who found that the dressed propagator takes the form [59]:

$$G^+(\boldsymbol{p},\omega) = \frac{Z}{\omega - v^*\boldsymbol{\sigma}\cdot\boldsymbol{p} + i\delta}, \tag{4.13}$$

within the conical approximation. To leading order in the coupling constant (α), the quasiparticle residue is given by:

$$Z^{-1} = 1 + \frac{\alpha}{\pi}\left(1 + \frac{\pi}{2}\right) + \mathcal{O}(\alpha^2), \tag{4.14}$$

and the Fermi velocity is renormalized by an isotropic prefactor:

$$\frac{v^*}{v_F} = 1 - \frac{\alpha}{\pi}\left[\frac{5}{3} + \ln(\alpha)\right] + \frac{\alpha}{4}\ln\left(\frac{k_c}{k_f}\right) + \mathcal{O}(\alpha^2), \tag{4.15}$$

where $k_c \sim 1/a$ is the momentum scale at which the conical approximation is no longer valid [59]. We note that renormalizing the bands in this way does not break the electron-hole symmetry, and so we will not include it in our analysis. One might also include the effects of vertex corrections, but such effects have been shown to be irrelevant in the weak coupling regime ($\alpha < 1$) [56, 75].

We are therefore left with two dominant zero-temperature many-body effects. The first is the screening of the Coulomb interaction by the Fermi-Dirac sea, which was already studied in detail in Chapter 3. The second is Pauli blocking of transitions to states below the Fermi level. This can be accounted for by using the causal propagators, which is the final missing ingredient. Therefore, we will study in Section 4.5 the form of the bare single-particle propagators.

4.5 Free particle propagator

In the following section, we will treat the problem of a pair of electrons interacting in the presence of the Dirac sea in graphene by mapping the BSE onto an effective two-particle Schrödinger equation. In order to do so, however, we first need to find the form of the bare, single-electron propagators. Given the time-dependent Dirac equation

$$\widehat{H}_1\psi = i\hbar\partial_t\psi, \tag{4.16}$$

we seek the free particle retarded propagator for particle 1, $G^+_{0,1}(\boldsymbol{p}, \boldsymbol{p}', t'-t)$. This function is proportional to the probability amplitude that if, at some time t, the electron is in a non-interacting system in eigenstate $\psi_{\boldsymbol{p}}$ then, at some later time $t' > t$, it will be in $\psi_{\boldsymbol{p}'}$. We can use the argument $t'-t$ without loss of generality unless dealing with time-dependant potentials (i.e. those which break time translational symmetry). The retarded propagator corresponds to an electron moving *forwards* in time. We note that we cannot propagate an electron below the Fermi level, so that excitations of energy $E < E_F$ are interpreted as holes (or, formally, electrons propagating *backwards* in time). Such excitations are instead described by the so-called advanced propagators. Therefore, it is natural to incorporate the effects of the Fermi-Dirac sea by using the language of causal propagators, which incorporate the effects of both electrons and holes, and which reduce to retarded and advanced Green's functions in the appropriate phase space regime ($E > E_F$ and $E < E_F$, respectively). We note that, given the

(bare) retarded propagator, the form of the causal propagator can be deduced in a straightforward way (see below). Thus, we first treat the simplest case of the retarded propagator, for the time-being.

The propagator is a Green's function. That is to say it is a solution to

$$(i\hbar\partial_t - \widehat{H}_1)G^+_{0,1}(\boldsymbol{p}, \boldsymbol{p}', t' - t) = \delta(t' - t). \tag{4.17}$$

We begin by making an ansatz for the $(\boldsymbol{p}, \omega)$-space Green's function, and will then check that it's Fourier transform satisfies Eq. (4.17). We propose that, in analogy with the free particle problem ($\widehat{H}_0 = \frac{p^2}{2m}$), the Green's function takes the form ($\hbar = 1$):

$$G^+_{0,1}(\boldsymbol{p}, \boldsymbol{p}', \omega) = \delta_{\boldsymbol{p},\boldsymbol{p}'} \left[\omega - \widehat{H}_1 + i\delta\right]^{-1}, \tag{4.18}$$

where δ is a positive infinitesimal and ω is the frequency associated with the propagation of the particle. Note that the Kronecker-δ factor explicitly conserves the momentum for a particle in the absence of interactions. Instead of writing it explicitly, we will now write the propagator as a function of $\boldsymbol{p}$ only and be careful to impose momentum-conservation on the diagrams later. The Hamiltonian $\widehat{H}_1$ operates on particle 1 only, but care must be taken to remember the two-particle nature of the problem. The Hilbert space defined in Section 2.2 is a two particle space. Thus, to capture the dynamics of particle 1 only, we use the tensor product operator $\widehat{H}_1 = \widehat{H} \otimes \sigma_{0,2}$, where $\widehat{H}$ is given by Eq. (1.47) and $\sigma_{0,2}$ is the unit operator on the space of particle 2. Upon substitution

into Eq. (4.18), we obtain:

$$G^{+}_{0,1}(\boldsymbol{p},\omega)_{=}\begin{bmatrix} \omega+\frac{p^2}{4m^*}+i\delta & 0 & -f(\boldsymbol{p}) & 0 \\ 0 & \omega+\frac{p^2}{4m^*}+i\delta & 0 & -f(\boldsymbol{p}) \\ -f^*(\boldsymbol{p}) & 0 & \omega+\frac{p^2}{4m^*}+i\delta & 0 \\ 0 & -f^*(\boldsymbol{p}) & 0 & \omega+\frac{p^2}{4m^*}+i\delta \end{bmatrix}^{-1}$$
$$= \frac{\omega+\frac{p^2}{2m^*}+\widehat{H}_1}{(\omega+\frac{p^2}{4m^*}+i\delta)^2-|f(\boldsymbol{p})|^2}, \tag{4.19}$$

where $f_i(\boldsymbol{p}) = v_F p e^{-i\phi_{\boldsymbol{p}}} + \tau_i \mu p^2 e^{2i\phi_{\boldsymbol{p}}}$. As expected, the poles of the propagator in Eq. (4.19) are located at the single-particle kinetic energies: $\omega_{\pm} = -\frac{p^2}{4m^*} \pm |f(\boldsymbol{p})|$. The Fourier transform is then given by:

$$\tilde{G}^{+}_{0,1}(\boldsymbol{p},t) = \int_{-\infty}^{\infty} G^{+}_{0,1}(\boldsymbol{p},\omega) e^{-i\omega t}\frac{d\omega}{2\pi} \tag{4.20}$$
$$= -\begin{bmatrix} i\cos(F) & 0 & \frac{f(\boldsymbol{p})}{|f(\boldsymbol{p})|}\sin(F) & 0 \\ 0 & i\cos(F) & 0 & \frac{f(\boldsymbol{p})}{|f(\boldsymbol{p})|}\sin(F) \\ \frac{f^*(\boldsymbol{p})}{|f(\boldsymbol{p})|}\sin(F) & 0 & i\cos(F) & 0 \\ 0 & \frac{f^*(\boldsymbol{p})}{|f(\boldsymbol{p})|}\sin(F) & 0 & i\cos(F) \end{bmatrix}$$
$$\times\, \Theta(t) e^{i\frac{p^2}{4m^*}t}$$

where $F = -|f(\boldsymbol{p})|t$ and $\Theta(t)$ is a step function which explicitly forces the electron to propagate forwards in time. In the above, we have chosen to set $t' = 0$ for simplicity, as allowed by time translational symmetry. Substitution into Eq. (4.17) shows that it does indeed satisfy the Schrödinger equation. Thus we conclude that Eq. (4.19) is the $(\boldsymbol{p},\omega)$-space bare propagator for particle 1.

For particle 2, we instead use the Hamiltonian $\widehat{H}_2 = \sigma_{0,1} \otimes \widehat{H}$, where $\widehat{H}$ is given by Eq. (1.47) and $\sigma_{0,1}$ is the unit operator on the space of particle 1. The same analysis

for particle 2 gives the Green's function

$$G^{+}_{0,2}(\boldsymbol{p},\omega) = \frac{\omega + \frac{p^2}{2m^*} + \widehat{H}_2}{(\omega + \frac{p^2}{4m^*} + i\delta)^2 - |f(\boldsymbol{p})|^2}. \tag{4.21}$$

In the following section, it will prove useful to express the propagators in terms of projection operators onto the eigenstates of the Hamiltonians for particles 1 and 2. We define the projection operator onto the state $|i,\lambda\rangle \otimes |\psi_{j\neq i}\rangle$ in the space of particle i:

$$\widehat{P}_{i,\lambda} = |i,\lambda\rangle \langle i,\lambda| , \tag{4.22}$$

where the $\{|i,\lambda\rangle\}$ are the eigenstates of the single particle Hamiltonian of particle i, with corresponding eigenvalues $E_{i,\lambda}$. In Appendix C we show that, for the i^{th} particle, the Green's functions can be expressed in the following form:

$$G^{+}_{0,i}(\boldsymbol{p},\omega) = \sum_{\lambda} \frac{\widehat{P}_{i,\lambda}}{\omega - E_{i,\lambda} + i\delta}. \tag{4.23}$$

Because we will no longer assume the Fermi level is at charge neutrality, we must modify the Green's function so as to account for some states with $E < 0$ being vacant. As discussed above, these vacancies correspond to hole excitations, which can be formally described as electrons which propagate backwards in time. This amounts to the replacement $\delta \to -\delta$ in the bare free-particle propagator (for a discussion see, for example, Refs. [71,72]). We will therefore switch to the language of the so-called causal Green's functions, which account for states above ($\omega > E_F$) and below ($\omega < E_F$) the Fermi level. For clarity of notation, we will also drop the subscript of 0, and proceed with the understanding that the single-particle Green's functions are all bare (since, as above, dressing them is not important for the purposes of this analysis). The Green's function of particle $i = 1, 2$ in the chiral representation becomes:

$$G_i(\boldsymbol{p},\omega) = \sum_{\lambda} \frac{\widehat{P}_{i,\lambda}}{\omega + E_F - E_{i,\lambda} + i\delta^{(i)}_{\boldsymbol{p},\lambda}}, \tag{4.24}$$

where, for $E_F < 0$:

$$\delta^{(i)}_{\boldsymbol{p},1} = \delta^{(i)}_{\boldsymbol{p},2} = \begin{cases} \delta, & \text{for } E_{i,\lambda}(\boldsymbol{p}) > E_F \\ -\delta, & \text{for } E_{i,\lambda}(\boldsymbol{p}) \leq E_F \end{cases}$$
$$\delta^{(i)}_{\boldsymbol{p},3} = \delta^{(i)}_{\boldsymbol{p},4} = \delta \tag{4.25}$$

with $\delta = 0^+$. Note that we have suppressed the 0 subscript, usually used to denote a free propagator because we will not calculate the single particle propagator here.

We now have all of the ingredients necessary to treat the BSE, which was given in its diagrammatic form in Eq. (4.11). In the following section, we will map this equation onto an effective, two-particle Schrödinger equation, and show that the poles of the former correspond to the eigenvalues of the latter, thus giving the binding energies of the pair.

4.6 Derivation of the effective two–particle Schrödinger equation

In Section 4.4, we gave the form of the BSE and explained the meaning of the various diagrammatic ingredients used in its formulation. In the momentum representation, Eq. (4.11) takes the form of an integral equation, which is to be solved for Γ. It is given by:

$$\Gamma(\boldsymbol{p}'\Omega', \boldsymbol{p}\Omega; \boldsymbol{K}\omega) = V_{\boldsymbol{p}\boldsymbol{p}'} + i \iint V_{\boldsymbol{p}''\boldsymbol{p}'} G_1(\boldsymbol{p}'', \epsilon) G_2(\boldsymbol{K} - \boldsymbol{p}'', \omega - \epsilon) \Gamma(\boldsymbol{p}''\epsilon, \boldsymbol{p}\Omega; \boldsymbol{K}\omega) \frac{d\boldsymbol{p}''}{(2\pi)^2} \frac{d\epsilon}{2\pi}, \tag{4.26}$$

where $V_{\boldsymbol{p}\boldsymbol{p}'} = V_{\boldsymbol{p}'\boldsymbol{p}} = V(|\boldsymbol{p} - \boldsymbol{p}'|)$ is the fully screened inter-layer interaction from Eq. (3.29). The momenta in Eq. (4.28) are interpreted as follows: $\boldsymbol{p}(\boldsymbol{p}')$ is the incoming (outgoing) momentum of particle 1, and $\boldsymbol{K}$ is the total momentum (this is not to be confused with the two Dirac points, which are denoted $\mathbf{K}^+$ and $\mathbf{K}^-$). We note that

$\boldsymbol{K}$ is a constant of the motion, due to momentum conserving factors in the interaction matrix element U_q, which arise due to translation invariance of the real-space potential: $V(\boldsymbol{r}_1, \boldsymbol{r}_2) = V(|\boldsymbol{r}_1 - \boldsymbol{r}_2|)$. Thus, $\boldsymbol{K} - \boldsymbol{p}$ ($\boldsymbol{K} - \boldsymbol{p}'$) is the incoming (outgoing) momentum of particle 2. In this thesis, we have focussed on the $\boldsymbol{K} = 0$ channel, but we will delay this restriction until the end for generality. This integral equation is general for such a ladder approximation up to the potentials which are written with no frequency dependence explicitly, for convenience. In fact, as Γ carries no external propagators, it is actually only dependant on the total frequency (ω) for our problem (i.e. Ω and Ω' are just used as convenient labels for the Γ diagram). For each term in Eq. (4.26) all internal frequencies (those used to label the Green's functions) are integrated out. This is not the case for a time-dependant interaction, however. In that case the second term in Eq. (4.26), for example, would correspond to:

$$-i\Gamma^{(1)}(\boldsymbol{p}'\Omega', \boldsymbol{p}\Omega; \boldsymbol{K}\omega) = \iint V(\boldsymbol{p}' - \boldsymbol{p}'', \Omega' - \epsilon) V(\boldsymbol{p}'' - \boldsymbol{p}, \epsilon - \Omega) \times G_1(\boldsymbol{p}'', \epsilon) G_2(\boldsymbol{K} - \boldsymbol{p}'', \omega - \epsilon) \frac{d\boldsymbol{p}''}{(2\pi)^2} \frac{d\epsilon}{2\pi}, \tag{4.27}$$

which *does* have an explicit dependence on Ω and Ω' for dynamic interactions. As we are only considering static screening in our case, we can simplify Eq. (4.26):

$$\Gamma(\boldsymbol{p}', \boldsymbol{p}; \boldsymbol{K}\omega) = V_{\boldsymbol{p}\boldsymbol{p}'} + \int V_{\boldsymbol{p}''\boldsymbol{p}'} \left[i \int G_1(\boldsymbol{p}'', \epsilon) G_2(\boldsymbol{K} - \boldsymbol{p}'', \omega - \epsilon) \frac{d\epsilon}{2\pi} \right] \Gamma(\boldsymbol{p}'', \boldsymbol{p}; \boldsymbol{K}\omega) \frac{d\boldsymbol{p}''}{(2\pi)^2}, \tag{4.28}$$

We therefore wish to compute the following integral:

$$I = \frac{i}{2\pi} \int_{-\infty}^{\infty} G_1(\epsilon) G_2(\omega - \epsilon) d\epsilon, \tag{4.29}$$

which is given in the brackets in Eq. (4.28) above. The details of the calculation are somewhat tedious, and have thus been relegated to Appendix D. There, we show that

it is given by:

$$I = \frac{1 - \widehat{n}_1 - \widehat{n}_2}{\omega + 2E_F - \widehat{H}_1 - \widehat{H}_2 + i(1 - \widehat{n}_1 - \widehat{n}_2)\delta}. \tag{4.30}$$

Substitution into Eq. (4.28), gives

$$\Gamma(\boldsymbol{p}', \boldsymbol{p}; \boldsymbol{K}\omega) = V_{\boldsymbol{p}\boldsymbol{p}'} + \int \frac{V_{\boldsymbol{p}''\boldsymbol{p}'} \widehat{N}_{\boldsymbol{p}'',\boldsymbol{K}}}{\omega + 2E_F - \widehat{H}_1(\boldsymbol{p}'') - \widehat{H}_2(\boldsymbol{K} - \boldsymbol{p}'') + i\widehat{N}_{\boldsymbol{p}'',\boldsymbol{K}}\delta} \Gamma(\boldsymbol{p}'', \boldsymbol{p}; \boldsymbol{K}\omega) \frac{d\boldsymbol{p}''}{(2\pi)^2}, \tag{4.31}$$

where we have defined $\widehat{N}_{\boldsymbol{p}'',\boldsymbol{K}} = 1 - \widehat{n}_1(\boldsymbol{p}'') - \widehat{n}_2(\boldsymbol{K} - \boldsymbol{p}'')$ from the Fermi-Dirac distributions at zero temperature:

$$n_i(p) = \begin{cases} 0, & \text{for } E_i(\boldsymbol{p}) > E_F, \\ 1, & \text{for } E_i(\boldsymbol{p}) \leq E_F. \end{cases} \tag{4.32}$$

We propose the following change of variables:

$$\Gamma(\boldsymbol{p}', \boldsymbol{p}; \boldsymbol{K}\omega) = \int V_{\boldsymbol{Q}} \widehat{N}_{\boldsymbol{p}'-\boldsymbol{Q},\boldsymbol{K}} \Psi(\boldsymbol{p}' - \boldsymbol{Q}, \boldsymbol{p}; \boldsymbol{K}\omega) \frac{d\boldsymbol{Q}}{(2\pi)^2}, \tag{4.33}$$

which we take to be a definition of Ψ rather than a solution for Γ. It follows then, that

$$\Gamma(\boldsymbol{p}'', \boldsymbol{p}; \boldsymbol{K}\omega) = \int V_{\boldsymbol{Q}'} \widehat{N}_{\boldsymbol{p}''-\boldsymbol{Q}',\boldsymbol{K}} \Psi(\boldsymbol{p}'' - \boldsymbol{Q}', \boldsymbol{p}; \boldsymbol{K}\omega) \frac{d\boldsymbol{Q}'}{(2\pi)^2}. \tag{4.34}$$

Substitution of Eqs. (4.33) and (4.34) into Eq. (4.31) gives an integral equation in Ψ:

$$\int V_{\boldsymbol{Q}} \widehat{N}_{\boldsymbol{p}'-\boldsymbol{Q},\boldsymbol{K}} \Psi(\boldsymbol{p}' - \boldsymbol{Q}, \boldsymbol{p}; \boldsymbol{K}\omega) \frac{d\boldsymbol{Q}}{(2\pi)^2} = V_{\boldsymbol{p}\boldsymbol{p}'} + \iint \frac{d\boldsymbol{Q}'}{(2\pi)^2} \frac{d\boldsymbol{p}''}{(2\pi)^2} V_{\boldsymbol{p}''\boldsymbol{p}'} V_{\boldsymbol{Q}'} \times$$
$$\times \frac{\widehat{N}_{\boldsymbol{p}'',\boldsymbol{K}}}{\omega + 2E_F - \widehat{H}_1(\boldsymbol{p}'') - \widehat{H}_2(\boldsymbol{K} - \boldsymbol{p}'') + i\widehat{N}_{\boldsymbol{p}'',\boldsymbol{K}}\delta} \widehat{N}_{\boldsymbol{p}''-\boldsymbol{Q}',\boldsymbol{K}} \Psi(\boldsymbol{p}'' - \boldsymbol{Q}', \boldsymbol{p}; \boldsymbol{K}\omega). \tag{4.35}$$

In order to map the integral equation (4.31) onto the two-particle Schrödinger equation, we propose the following change of variables:

$$\Psi(\boldsymbol{p}', \boldsymbol{p}; \boldsymbol{K}\omega) = (2\pi)^2 \delta^{(2)}(\boldsymbol{p}-\boldsymbol{p}') + \frac{1}{\omega + 2E_F - \widehat{H}_1(\boldsymbol{p}') - \widehat{H}_2(\boldsymbol{K}-\boldsymbol{p}') + i\widehat{N}_{\boldsymbol{p}',\boldsymbol{K}}\delta} \times \\ \times \int V_{\boldsymbol{q}'} \widehat{N}_{\boldsymbol{p}'-\boldsymbol{q}',\boldsymbol{K}} \Psi(\boldsymbol{p}'-\boldsymbol{q}', \boldsymbol{p}; \boldsymbol{K}\omega) \frac{d\boldsymbol{q}'}{(2\pi)^2}. \tag{4.36}$$

Let us examine the significance of Eq. (4.36). The frequency ω gives the energy of the pair near the poles, and E_F simply sets the zero point of the energy, so we can make the replacement $\omega + 2E_F \equiv E$. The first term in Eq. (4.36) is energy independent, while the second term has poles which correspond to two-particle states. Near these poles, the first term can be dropped. Further, the integrand vanishes due to $\widehat{N}$ whenever the particle in the valance band is below the Fermi level. We can therefore absorb it into the limits of the integral. Finally, this can be expressed as an effective two-particle Schrödinger equation, where we identify Ψ as a two-particle wavefunction:

$$\left(\widehat{H}_1(\boldsymbol{p}') + \widehat{H}_2(\boldsymbol{K}-\boldsymbol{p}')\right) \Psi_{\boldsymbol{p}',\boldsymbol{K}} + \iint\limits_{|\boldsymbol{q}'+\boldsymbol{p}'|<p_F} U_{\boldsymbol{q}'} \Psi_{\boldsymbol{p}'-\boldsymbol{q}',\boldsymbol{K}} \frac{d\boldsymbol{q}'}{(2\pi)^2} = E\Psi_{\boldsymbol{p}',\boldsymbol{K}}. \tag{4.37}$$

In the $\boldsymbol{K} = 0$ channel, Eq. (4.37) is equivalent to the two-particle Schrödinger equation we presented as a heuristic model in Section 4.2 when one projects the Hamiltonian onto the sub-space spanned by the para-state, such that $\Psi = \sum\limits_{|\boldsymbol{p}|<p_F} \psi_p \, |2, \phi_{\boldsymbol{p}}\rangle$. This justifies the assumption of Section 4.2 in the absence of trigonal warping. To include the warping effects, all four states have to be included in the model. The states $|3, \phi_{\boldsymbol{p}}\rangle$ and $|4, \phi_{\boldsymbol{p}}\rangle$, however, are less important than ortho-states due to energy mismatch.

4.7 The effects of finite-range interaction and trigonal warping

The analytic form of the binding energies, along with the low-doping approximation, are plotted in Figs. 4.2 and 4.3 for the cases of single- and double-layer devices, respectively. For the two-layer case, the results were obtained for graphene in a hexagonal boron nitride (hBN) environment. For the single-layer case, however, our analytical result is entirely independent of the substrate (see Eq. 3.41). In both configurations the linear approximation is substrate-independent, confirming that the low-doping behaviour is dominated by momentum-space restrictions due to Pauli blocking. The points on those plots correspond to binding energies obtained numerically (see below), and account for contributions from the full non-dispersing sector, as well as the momentum-dependent interaction. We have used $\eta = 1.1$ throughout.

So far we have considered a subspace of the possible bound states of the system: those spanned by the para-state. It was shown that the isotropic dispersion ($\propto -p^2/2m^*$) leads to an exact solution under the assumption that the potential is short-ranged. When we consider other states in the non-dispersing sector, however, the effects of trigonal warping enter the problem in two ways: (i) there is an extra contribution to the kinetic energy (see Eq. (2.5)), and (ii) the Fermi surface is deformed, so that states excluded by Pauli blocking occupy a domain with a more complicated shape. In addition, we treated an electron-electron potential of the form $V(\boldsymbol{r}) = \lambda\delta(\boldsymbol{r})$, which tends to overestimate the interaction strength. In Chapter 2 it was shown that the effective Hamiltonian of an electron pair in the non-dispersing sector is given by

$$\widehat{H}_{\boldsymbol{p},\boldsymbol{p}'} = \delta_{\boldsymbol{p},\boldsymbol{p}'}\widehat{H}^{\text{eff}}_{1,2} + U_{\boldsymbol{p},\boldsymbol{p}'}\begin{bmatrix} \cos(\phi_{\boldsymbol{p}} - \phi_{\boldsymbol{p}'}) & 0 \\ 0 & 1 \end{bmatrix}, \tag{4.38}$$

due to the non-trivial overlap of wavefunctions with different momenta: $\langle 1, \phi_{\boldsymbol{p}'}|1, \phi_{\boldsymbol{p}}\rangle = \cos(\phi_{\boldsymbol{p}} - \phi_{\boldsymbol{p}'})$. When the effects of screening (so that $U_{\boldsymbol{p},\boldsymbol{p}'} \equiv U(|\boldsymbol{p} - \boldsymbol{p}'|)$ is given by

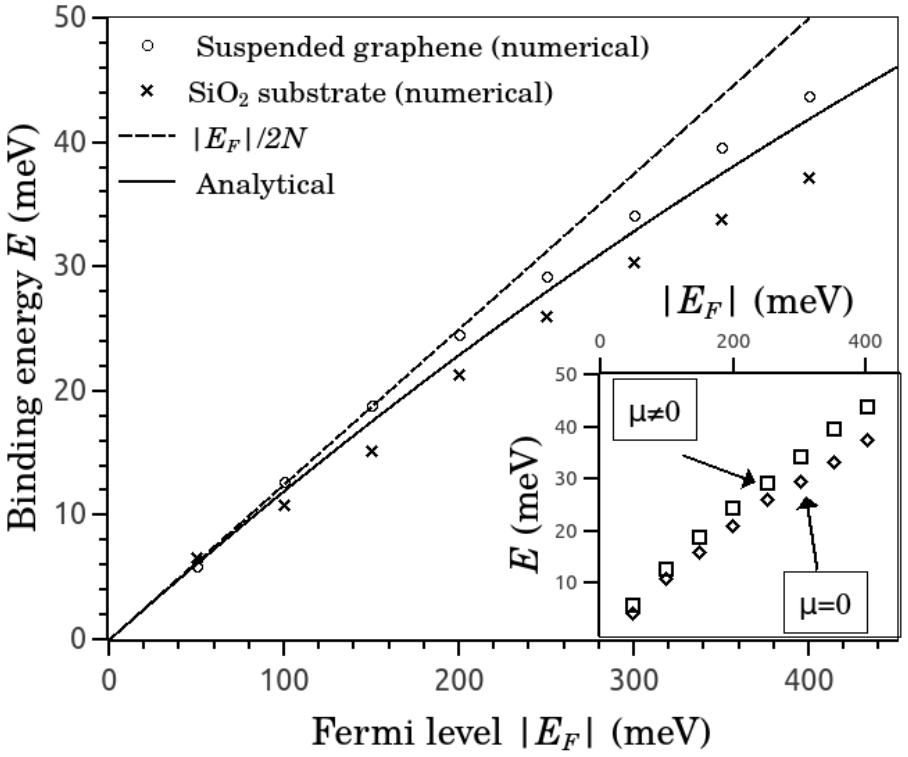

Figure 4.2: Binding energies in single-layer systems. The symbols represent numerical results, the solid line is the analytical form of Eq. (4.6) and the broken line corresponds to the low-doping approximation of Eq. (4.10). The inset shows numerical results for a single-layer suspended graphene structure with trigonal warping switched on ($\mu \neq 0$) and off ($\mu = 0$). The small increase in kinetic energy from the trigonal warping explains the difference between numerical results and the analytical approximation (which was calculated with isotropic kinetic energy) for the case of suspended graphene.

the potentials in Eq. (3.29)) and the warped Fermi surface are taken into account, the problem becomes intractable. Therefore, in this section we present the results of the numerical diagonalization of Eq. (4.38), and compare them with the analytical solution discussed previously.

For monolayer systems, we assume the graphene lies on a substrate of dielectric constant ϵ_s, so that $\kappa = \frac{1}{2}(1+\epsilon_s)$. We present results for two common experimental systems: (i) suspended graphene ($\epsilon_s = 1$) and (ii) graphene on a SiO_2 substrate ($\epsilon_s = 3.9$). For double-layer systems the situation is slightly different, as the graphene layers must be separated by a dielectric spacer in order to suppress bilayer coupling.

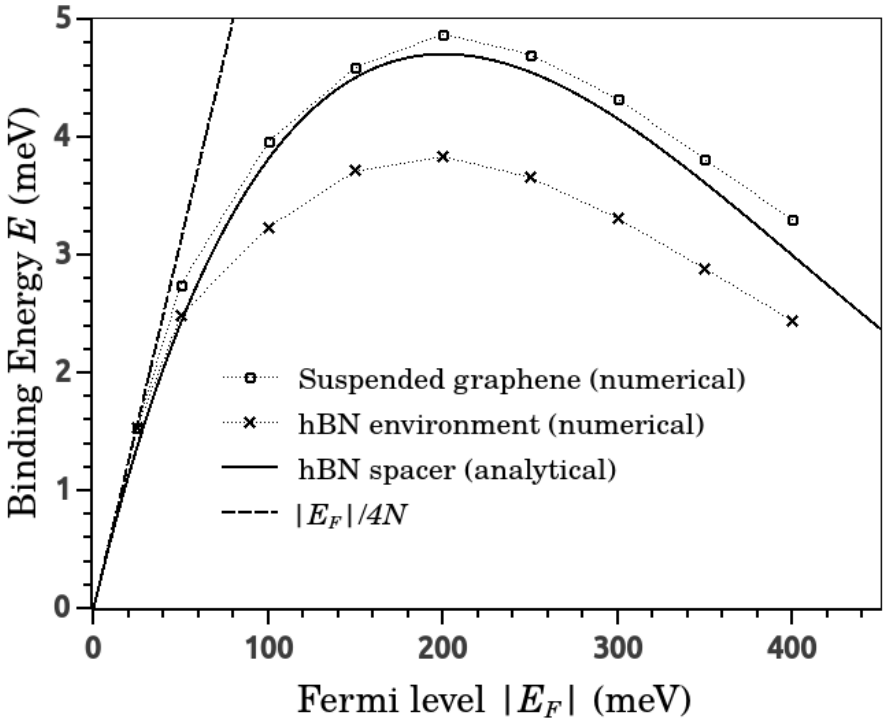

Figure 4.3: Binding energies in double-layer (graphene-hBN-graphene) structures which are suspended over vacuum (circles) or embedded in an hBN environment (crosses). The solid line is the analytical result for the double-layered system embedded in hBN, and the broken line is the low-doping approximation.

We provide results for a hexagonal boron nitride (hBN) spacer. hBN has dielectric constant $\epsilon_h = 3.9$ and has been experimentally shown to electrically isolate parallel graphene layers at a thickness of 4 atomic layers ($d = 1.3$nm) [44]. We have considered two distinct double-layered cases: hBN-graphene-hBN structures which are (i) embedded in a hBN environment ($\kappa = \epsilon_h$) and (ii) suspended in vacuum ($\kappa = \frac{1}{2}(1 + \epsilon_h)$).

For the double-layer case (see Fig. 4.3) there is good agreement between the numerical results and the linear approximation of Eq. (4.10) for $|E_F| \lesssim 50$meV. For higher doping, however, the analytical solution overestimates the binding energy. Our assumption that the Fermi surface is circular (i.e. ignoring trigonal warping) is asymptotically exact in the limit $p_F \to 0$ so we expect our analytical solution from Sec. 4.2 to diverge from the numerical results (which take account of warping) for large p_F. We also note

that the interaction potential U_q is positive definite and has a maximum at $q = 0$. Therefore, using the interaction strength $\lambda = U_{q=0}$ is guaranteed to overestimate the strength of the potential. The curve is peaked at $E_F \sim -200$meV. This is due to the small value of $E_d \sim 0.2$eV, which defines an energy scale accessible even at relatively low doping.

For the single-layer case, the linear approximation of our analytical result agrees well with numerical values over the whole region of experimental interest ($|E_F| \lesssim 400$meV). In contrast to the double-layer case, the exponential suppression of the binding is not accessible in this range, however, due to the relatively large energy scale of the single-layer problem: $E_s \sim 5E_d$.

We also note that the single-layer numerical results of Fig. 4.2 for the case of suspended graphene are slightly higher than the analytic result. This is entirely due to trigonal warping, which was not accounted for in Eq. (4.2). The effective Hamiltonian of Eq. (2.5) has eigenvalues of the form $\epsilon = -2\mu p^2 [\eta + \sin(3\phi_{\boldsymbol{p}})]$, which correspond to the kinetic energy of the pair. Although this term is negative definite for $\eta > 1$, the kinetic energy is suppressed for certain momentum space configurations due to the sign-indefinite trigonal contribution. This leads to increased binding energy when interactions are taken into account, an effect not accounted for in the purely isotropic Hamiltonian used in the analytic approximation of Section 4.2. The inset of Fig. 4.2 displays the binding energies of a bi-electron in single-layer suspended graphene with ($\mu \neq 0$) and without ($\mu = 0$) trigonal warping switched on. The results show that trigonal warping tends to increase the binding energy of the pair, as discussed above. We note that the results for $\mu = 0$ and $\mu \neq 0$ diverge from each other as the Fermi energy is decreased. This is to be expected, as warping of the energy bands is only appreciable at high energies. When the system is doped near the neutrality point, the difference between phase-space restriction for the warped and conical cases is negligible.

Although we have obtained numerical results up to $E_F = 400$meV, we note that such high doping may not be practical for experiment. For the cases of monolayer

graphene on SiO_2 and double layer graphene in a hBN environment, the limiting factor is likely to be dielectric breakdown in the region between graphene and gate. For the example of hBN, it was found in tunnelling experiments [44] that breakdown occurs at 3V for a 4-layer-thick spacer, so that it is possible to achieve $|E_F| \sim 800$meV. Due to the large breakdown field of vacuum, other factors are expected to limit the range of validity for suspended graphene. When not supported by a substrate, finite charge densities of opposite sign on the gate and graphene respectively lead to deflection of the graphene away from its usual atomically flat structure [76–78], which can result in the electrostatic collapse of the device. As an example, we consider the device of Ref. [76]: a square graphene sample of dimension $\sim 3\mu$m is suspended 150nm above a 150nm thick layer of SiO_2 (which rests atop a Si substrate). When a gate voltage V_G was applied between graphene and Si, collapse occurred at $V_G = 20$V. This corresponds to a maximum doping of $|E_F| \sim 90$meV. The precise upper bound which is experimentally accessible depends strongly on device geometry, which we do not consider here.

Chapter 5

Conclusion

5.1 Summary

In this thesis, we have analysed the problem of an interacting electron-electron pair in graphene. We have shown that kinetic energy terms which are of second order in the momentum can lead to the formation of bi-electrons: bound states of two electrons, which are facilitated by the repulsive Coulomb interaction.

In Chapter 2 we analyzed the problem of an isolated electron-electron pair, without significant attention being paid towards many-body effects. We have shown that, in the isotropic regime, the conduction-valence band asymmetry allows the formation of a new kind of Cooper-pair-like bound state in the sector spanned by eigenfunctions which are dispersionless in the conical approximation. From analysis of the local density of states, we found that such pairs can have energies of 45meV when the constituent electrons are spatially separated in hybrid double-layer structures. The structures we considered were those formed by parallel graphene layers with hBN spacers with thickness of several atomic layers. These states have positive energy and therefore do not represent energy minima, however once created they have long lifetimes. We calculated their transition rates and found that tunnelling into the continuum of free-particle states has an associated lifetime of $\sim 100\mu$s. Due to the large value of this lifetime, we note that such tunnelling is likely not the limiting factor in the stability of the pair. Instead, they

would have their true lifetimes determined by non-universal factors such as impurity scattering, which we do not consider here. Finally, we applied a semiclassical approach to the real-space dynamics of the pair in order to visualize their behaviour and develop an intuition for the pairing mechanism from a classical perspective. We saw that a finite relative velocity of the pair implies that a repulsive force between the two particles will increase the velocity of the slower particle, while decreasing the velocity of the faster one. This gives a qualitative picture of the pairing in the absence of attractive interactions, and shows how the unusual band-structure of graphene can allow us to go beyond the conventional wisdom that 'like charges repel' without a fully quantised formalism.

In Chapter 3, we calculated the bare and screened interactions for single- and double-layered graphene structures in homogeneous and non-trivial dielectric environments. In particular we have explained and justified the calculation of intrinsic dielectric constants, which enable the incorporation of screening for in systems doped near charge neutrality without a full treatment of the polarizability function. We also argued that, in the presence of the Dirac sea in graphene, the most important aspects of the electron-electron interaction can be captured by an effective delta-like potential, and calculated the interaction strength.

In Chapter 4, we turned our attention to the problem of an electron-electron pair in single- and double-layer graphene structures, taking into account the most important many-body effects at zero temperature: interaction screening and the blocking of single-particle transitions to states below the Fermi level by the Pauli exclusion principle. We have shown that the binding energies are renormalized, but not destroyed, by the presence of the Dirac sea. Within the range of attainable doping, the binding energies are about an order of magnitude higher for single-layered structures, suggesting that they are of the greatest experimental interest. In particular we have shown that, for sufficiently low hole doping ($|E_F| \lesssim 400$meV for one layer and $|E_F| \lesssim 50$meV for two layers) the renormalized energies are directly proportional to the magnitude of

the Fermi energy, to a good approximation. We therefore conclude that the pairing is tunable by a gate voltage for single- and double-layer systems, and that the results are robust against a small doping mismatch between the layers.

5.2 Outlook

One important unanswered question is the nature of an experimental signature of this pairing. The positivity of the binding energies implies that the corresponding non-trivial correlated phase would be rather unusual: unlike the case of the more familiar excitons, which have negative binding energies due to an attractive interaction, the pairs described in this thesis have positive energies. Hence, their formation is not energetically favourable. It was shown in Chapter 2, however, that their decay rates are slow. Therefore, the bi-electronic condensate, should it form, would be metastable, and would not be a candidate for novel superconductivity. Further, because the pair is formed of two particles of the same species, they have a net negative charge. Thus, formation of the condensate would not result in a novel insulating phase. Another avenue might be to search for a bound state using scanning tunnelling microscopy but, due to the nature of the particles, that would require a sophisticated two-particle coherent tunnelling experiment. Probing the pairs using optical measurements, as is common in the excitonic phenomena, is complicated by zero dipole moment of liked-charged pairs. Again, this is due to the total charge of the pair, which cancels for electron-hole pairs.

Perhaps the most promising route towards experimental realization is by the coupling of the aforementioned graphene structures to a superconductor. As the metastable states are akin to Cooper pairs, this would lead to a giant enhancement of the proximity effect, which has been observed in graphene recently [79–81]. The recent realization of a graphene-based Cooper pair splitter might provide the setting for such an experiment [82]. The pair splitter is coupled to a quantum dot in each of its two output channels, and the dots can be tuned by the application of side gates so that the Cooper

pairs can tunnel into them when on resonance. By tuning across the energy range in which we predict bi-electrons to form, one would expect an enhancement in the occupation of the dots relative to the energy in which bi-electron pairing is not predicted. The enhancement is due to the increased density of states predicted in Chapters 2 and 4.

We have not, however, considered the effects of finite temperature which may be important, particularly for the case of double-layered structures where the binding energies are rather low (0meV–5meV).

Appendices

Appendix A

Calculation of the effective Hamiltonian Matrix

Here we explain in more detail the form of the effective Hamiltonian matrix given in Eq. (2.5). Our goal is to construct an operator which effectively describes the dynamics in the non-dispersing sector (two-particle states with $E = 0$) but neglects those states within the dispersing sector ($E \neq 0$). We note that the eigenfunctions of the two-particle Hamiltonian matrix in the conical regime (see Eq. (2.2)) form a complete basis. Therefore, we could perform a change of basis, and write the Hamiltonian matrix with elements $H_{i,j} = \langle i, \phi_{\boldsymbol{p}}| H |j, \phi_{\boldsymbol{p}}\rangle$. Let us write the resulting eigenvalue problem in block form:

$$\begin{bmatrix} H_D & H_C \\ H_C^\dagger & H_N \end{bmatrix} \begin{bmatrix} \Phi_D \\ \Phi_N \end{bmatrix} = E \begin{bmatrix} \Phi_D \\ \Phi_N \end{bmatrix}, \tag{A.1}$$

where H_D is the Hamiltonian matrix within the dispersing sector, H_N is the Hamiltonian matrix in the non-dispersing sector and H_C contains the coupling between the sectors. In the above, if we found that $H_C = 0$, so that there was no coupling between the sectors, then Φ_D are the states of configuration $|1, \phi_{\boldsymbol{p}}\rangle + \lambda |2, \phi_{\boldsymbol{p}}\rangle$ and Φ_N are the states of configuration $|3, \phi_{\boldsymbol{p}}\rangle + \lambda |4, \phi_{\boldsymbol{p}}\rangle$. Thus we have block diagonalized the Hamiltonian

matrix, and H_D would be the effective operator required.

If we calculate the matrix elements in this new basis, however, we find that H_C is non-zero, and should not be neglected in general. Thus we construct the effective Hamiltonian matrix using the approach from Ref. [39], which is akin to degenerate perturbation theory. Let $E^{(0)}$ be the unperturbed energies and $H^{(1)}$ be the Hamiltonian matrix which contains the details of the perturbation (ie, the nonlinear terms). Then the effective Hamiltonian matrix is given by:

$$H^{\text{eff}}_{i,j} = \delta_{i,j} E^{(0)}_i + \langle i, \phi_{\boldsymbol{p}}| \, H^{(1)} \, |j, \phi_{\boldsymbol{p}}\rangle - \sum_{k=3,4} \frac{\langle i, \phi_{\boldsymbol{p}}| \, H^{(1)} \, |k, \phi_{\boldsymbol{p}}\rangle \, \langle k, \phi_{\boldsymbol{p}}| \, H^{(1)} \, |j, \phi_{\boldsymbol{p}}\rangle}{E^{(0)}_k - E^0_i}, \quad \text{(A.2)}$$

where the summation runs over the dispersing states. From our previous analysis, we know that $E_{1,2} = 0$ and $E_{3,4} = \pm 2 v_f p$. Those terms terms which couple the two sectors are either vanishing or of second order in the momentum. Thus, we obtain:

$$H^{\text{eff}}_{i,j} = \langle i, \phi_{\boldsymbol{p}}| \, H^{(1)} \, |j, \phi_{\boldsymbol{p}}\rangle - \mathcal{O}\left[\frac{\mu p^3}{v_f}\right]. \quad \text{(A.3)}$$

Thus we keep only terms which are of first order in the perturbation, giving the effective Hamiltonian matrix:

$$\widehat{H}^{\text{eff}} = \begin{bmatrix} -\frac{p^2}{2m^*} & \tau_{1,2}\mu p^2 \sin(3\phi_{\boldsymbol{p}}) \\ \tau_{1,2}\mu p^2 \sin(3\phi_{\boldsymbol{p}}) & -\frac{p^2}{2m^*} \end{bmatrix}, \quad \text{(A.4)}$$

which is the form used in Eq. (2.5) and thereafter.

The matrix elements due to the contributions of states $|3, \phi\rangle$ and $|4, \phi\rangle$, which were

omitted from the form above, are as follows:

$$\begin{aligned}\langle 3,\phi'_j|\,H\,|1,\phi_i\rangle &= \langle 4,\phi'_j|\,H\,|1,\phi_i\rangle = -\langle 1,\phi'_j|\,H\,|3,\phi_i\rangle = -\langle 1,\phi'_j|\,H\,|4,\phi_i\rangle \\ &= -\frac{i}{\sqrt{2}}U(|\boldsymbol{q}_i-\boldsymbol{p}'_j|)\sin(\phi_i-\phi'_j) \qquad \text{(A.5)}\\ \langle 3,\phi'_j|\,H\,|2,\phi_i\rangle &= \langle 4,\phi'_j|\,H\,|2,\phi_i\rangle = \langle 2,\phi'_j|\,H\,|3,\phi_i\rangle = \langle 2,\phi'_j|\,H\,|4,\phi_i\rangle \\ &= i\sqrt{2}\mu q_i^2\sin(3\phi_i)\delta_{ij} \qquad \text{(A.6)}\\ \langle 4,\phi'_j|\,H\,|3,\phi_i\rangle &= \langle 3,\phi'_j|\,H\,|4,\phi_i\rangle = \frac{1}{2}\left[\cos(\phi_i-\phi'_j)-1\right]U(|\boldsymbol{q}_i-\boldsymbol{p}'_j|) \qquad \text{(A.7)}\\ \langle 3,\phi'_j|\,H\,|3,\phi_i\rangle &= \frac{1}{2}\left[\cos(\phi_i-\phi'_j)+1\right]U(|\boldsymbol{q}_i-\boldsymbol{p}'_j|)+2\alpha q_i^2\delta_{ij}+2\lambda q_i \qquad \text{(A.8)}\\ \langle 4,\phi'_j|\,H\,|4,\phi_i\rangle &= \frac{1}{2}\left[\cos(\phi_i-\phi'_j)+1\right]U(|\boldsymbol{q}_i-\boldsymbol{p}'_j|)+2\alpha q_i^2\delta_{ij}-2\lambda q_i \qquad \text{(A.9)}\end{aligned}$$

Appendix B

Numerical approach

Here we will briefly explain the approach used to calculate the LDOS plots given in Section 2.3. Recall that the LDOS is given by $\nu(\epsilon, x, y) = \sum_n \delta(\epsilon - \epsilon_n)|\psi_n(x, y)|^2$. The calculation of the real-space wavefunctions $\psi_n(x, y)$ is straightforward when given the momentum-space wavefunctions, following by fast Fourier transform. Thus, our main task is to describe the diagonalization of the effective Hamiltonian matrix in momentum space.

It is common to use one of several Brillouin zone summation schemes to sample the most important **k**-points instead of naively sampling a simple mesh, to minimize computational expense (see, for example, Ref. [83]). For the current purposes, however, we are most interested in a relatively small phase-space near the Dirac points. Therefore, the calculations utilized a simple hexagonal lattice of momentum-space sites to reflect the symmetry of graphene's honeycomb lattice. The grid is populated shell-by-shell (see Fig. B.1), so there are two parameters which can vary the results. The first is the number of shells, which we have taken to be $N = 33$ for all results given in this thesis (corresponding to approximately 3400 grid points). There are a total of $3N(N+1)+1$ grid sites for N shells, so increasing N corresponds to increasing the total number of points, and thus reduces discretization errors. We did not obtain results for $N > 33$ due to hardware limitations, but the energy levels were seen to vary negligibly above $N = 20$. Secondly, one can vary the cut-off momentum $p_{\max}$. Decreasing $p_{\max}$ allows

one to limit the phase space under consideration, hence increasing the density of sites. The results in the body of the present text were obtained for $p_{\max} = \frac{\pi}{3a}$, thus covering the sites of primary interest in the low-energy physics.

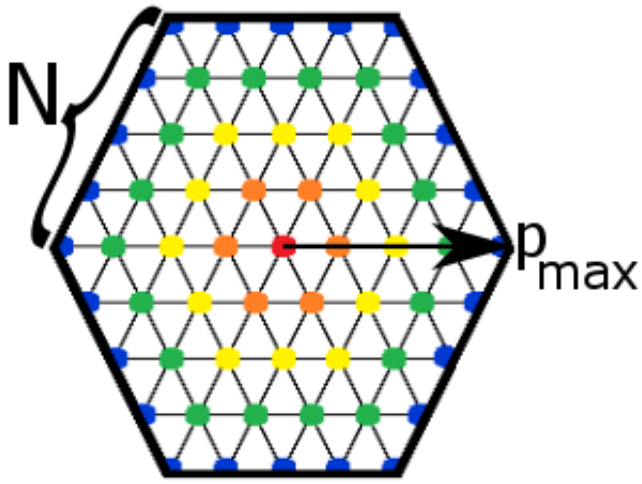

Figure B.1: Schematic of the momentum-space grid for the example of $N = 4$ shells. Shells are coloured as follows: red (0^{th} shell), orange (1^{st} shell), yellow (2^{nd} shell), and so on. The vector shown has magnitude $p_{\max}$. All results in this thesis were generated for $N = 33$.

In order to find the binding energies of the electron-electron pair, we begin with the discretized, momentum-space Schrödinger equation:

$$H_{\text{eff}}(\boldsymbol{p})\psi_{\boldsymbol{p}} + S_0 \sum_{\boldsymbol{p}'} \tilde{V}_{\boldsymbol{p}-\boldsymbol{p}'} A_{\boldsymbol{p},\boldsymbol{p}'} \psi_{\boldsymbol{p}'} = E\psi_{\boldsymbol{p}}, \tag{B.1}$$

which has been projected onto the subspace of non-dispersing states as explained previously. We have defined S_0 to be the area of a cell in the momentum space grid and $A_{\boldsymbol{p},\boldsymbol{p}'}$ is the matrix arising due to non-trivial overlap between non-dispersing states:

$$A_{\boldsymbol{p},\boldsymbol{p}'} = \begin{bmatrix} \cos(\phi_{\boldsymbol{p}} - \phi_{\boldsymbol{p}'}) & 0 \\ 0 & 1 \end{bmatrix} \tag{B.2}$$

Note that Eq. (B.1) can be re-written in the equivalent form:

$$\sum_{\boldsymbol{p}'} \begin{bmatrix} -\frac{p^2}{2m^*}\delta_{\boldsymbol{p},\boldsymbol{p}'} + S_0\tilde{V}_{\boldsymbol{p},\boldsymbol{p}'}\cos(\phi_{\boldsymbol{p}} - \phi_{\boldsymbol{p}'}) & 2\mu p^2 \sin(3\phi_{\boldsymbol{p}})\delta_{\boldsymbol{p},\boldsymbol{p}'} \\ 2\mu p^2 \sin(3\phi_{\boldsymbol{p}})\delta_{\boldsymbol{p},\boldsymbol{p}'} & -\frac{p^2}{2m^*}\delta_{\boldsymbol{p},\boldsymbol{p}'} + S_0\tilde{V}_{\boldsymbol{p},\boldsymbol{p}'} \end{bmatrix} \psi_{\boldsymbol{p}'}$$
$$= E\psi_{\boldsymbol{p}}. \tag{B.3}$$

The matrix in Eq. (B.3) simply that of Eq. (2.8). We calculate the binding energies by populating a matrix with these blocks or, equivalently, by constructing a system of equations of the form (B.3), each of which is designated a unique momentum $\boldsymbol{p}$. We note that, in the calculation of the LDOS using the definition of $\nu(\epsilon, x, y)$ given above, we have approximated the Dirac delta function by a Poisson distribution:

$$\delta(\epsilon - \epsilon_n) \sim \frac{1}{\pi}\frac{\gamma}{(\epsilon - \epsilon_n)^2 + \gamma^2}, \tag{B.4}$$

and used the broadening factor $\gamma = 0.1$meV throughout.

Appendix C

Free particle Green's functions in terms of projection operators

We look for a set of projection operators for particle 1, $\widehat{P}_{1,\lambda}(\boldsymbol{p})$, such that

$$\widehat{P}_{1,\lambda}(\boldsymbol{p})\chi_{\lambda'}(\boldsymbol{p}) = \chi_{\lambda}(\boldsymbol{p})\delta_{\lambda,\lambda'}, \tag{C.1}$$

where λ, λ' are the eigenstate numbers. This can be achieved by computing $\widehat{P}_{1,\lambda}(\boldsymbol{p}) = |\chi_\lambda\rangle \langle\chi_\lambda|$, giving

$$\widehat{P}_{1,1}(\boldsymbol{p}) = \frac{1}{2}\begin{bmatrix} 0 & 0 & 0 & 0 \\ 0 & 1 & 0 & -e^{i\theta_{\boldsymbol{p}}} \\ 0 & 0 & 0 & 0 \\ 0 & -e^{-i\theta_{\boldsymbol{p}}} & 0 & 1 \end{bmatrix},$$

$$\widehat{P}_{1,2}(\boldsymbol{p}) = \frac{1}{2}\begin{bmatrix} 1 & 0 & -e^{i\theta_{\boldsymbol{p}}} & 0 \\ 0 & 0 & 0 & 0 \\ -e^{-i\theta_{\boldsymbol{p}}} & 0 & 1 & 0 \\ 0 & 0 & 0 & 0 \end{bmatrix},$$

$$\widehat{P}_{1,3}(\boldsymbol{p}) = \frac{1}{2}\begin{bmatrix} 0 & 0 & 0 & 0 \\ 0 & 1 & 0 & e^{i\theta_{\boldsymbol{p}}} \\ 0 & 0 & 0 & 0 \\ 0 & e^{-i\theta_{\boldsymbol{p}}} & 0 & 1 \end{bmatrix},$$

$$\widehat{P}_{1,4}(\boldsymbol{p}) = \frac{1}{2}\begin{bmatrix} 1 & 0 & e^{i\theta_{\boldsymbol{p}}} & 0 \\ 0 & 0 & 0 & 0 \\ e^{-i\theta_{\boldsymbol{p}}} & 0 & 1 & 0 \\ 0 & 0 & 0 & 0 \end{bmatrix}. \tag{C.2}$$

In particular, it can be shown by substitution that

$$\sum_{\lambda} \widehat{P}_{1,\lambda}(\boldsymbol{p}) = \sigma_{0,1} \otimes \sigma_{0,2} \tag{C.3}$$

as required for projection operators.

Further, the same analysis can be completed to obtain a set of projection operators for particle 2, $\widehat{P}_{2,\lambda}(\boldsymbol{p}) = |\xi_\lambda\rangle \langle\xi_\lambda|$:

$$\widehat{P}_{2,1}(\boldsymbol{p}) = \frac{1}{2}\begin{bmatrix} 0 & 0 & 0 & 0 \\ 0 & 0 & 0 & 0 \\ 0 & 0 & 1 & e^{i\theta_{\boldsymbol{p}}} \\ 0 & 0 & e^{-i\theta_{\boldsymbol{p}}} & 1 \end{bmatrix},$$

$$\widehat{P}_{2,2}(\boldsymbol{p}) = \frac{1}{2}\begin{bmatrix} 1 & e^{i\theta_{\boldsymbol{p}}} & 0 & 0 \\ e^{-i\theta_{\boldsymbol{p}}} & 1 & 0 & 0 \\ 0 & 0 & 0 & 0 \\ 0 & 0 & 0 & 0 \end{bmatrix},$$

$$\widehat{P}_{2,3}(\boldsymbol{p}) = \frac{1}{2}\begin{bmatrix} 0 & 0 & 0 & 0 \\ 0 & 0 & 0 & 0 \\ 0 & 0 & 1 & -e^{i\theta_{\boldsymbol{p}}} \\ 0 & 0 & -e^{-i\theta_{\boldsymbol{p}}} & 1 \end{bmatrix},$$

$$\widehat{P}_{2,4}(\boldsymbol{p}) = \frac{1}{2}\begin{bmatrix} 1 & -e^{i\theta_{\boldsymbol{p}}} & 0 & 0 \\ -e^{-i\theta_{\boldsymbol{p}}} & 1 & 0 & 0 \\ 0 & 0 & 0 & 0 \\ 0 & 0 & 0 & 0 \end{bmatrix}. \tag{C.4}$$

Now we will write the Green's function for particle 1 in terms of these projection operators. Using the identity from Eq. (C.3), we can rewrite Eq. (4.19) in the following form:

$$\begin{aligned} G^{+}_{0,1}(\boldsymbol{p},\omega) &= \frac{\omega(\widehat{P}_{1,1}+\widehat{P}_{1,2}+\widehat{P}_{1,3}+\widehat{P}_{1,4}) + \frac{p^2}{2m^*} + \widehat{H}_1}{(\omega + \frac{p^2}{4m^*} + |f(\boldsymbol{p})| + i\delta)(\omega + \frac{p^2}{4m^*} - |f(\boldsymbol{p})| + i\delta)} \\ &= \frac{\omega(\widehat{P}_{1,1}+\widehat{P}_{1,2}+\widehat{P}_{1,3}+\widehat{P}_{1,4}) + \frac{p^2}{2m^*} + \widehat{H}_1}{(\omega - E_{1,-} + i\delta)(\omega - E_{1,+} + i\delta)} \end{aligned} \tag{C.5}$$

where $E_{11} = E_{12} = E_{1,-}$ and $E_{13} = E_{14} = E_{1,+}$. From $\widehat{H}_1 = \widehat{H} \otimes \sigma_{0,2}$, where $\widehat{H}$ is given by Eq. (1.47), we expand:

$$\begin{aligned} \widehat{H}_1 + \frac{p^2}{2m^*} &= \frac{p^2}{4m^*} + |f(\boldsymbol{p})| \begin{bmatrix} 0 & 0 & e^{i\theta_{\boldsymbol{p}}} & 0 \\ 0 & 0 & 0 & e^{i\theta_{\boldsymbol{p}}} \\ e^{-i\theta_{\boldsymbol{p}}} & 0 & 0 & 0 \\ 0 & e^{-i\theta_{\boldsymbol{p}}} & 0 & 0 \end{bmatrix} \\ &= \frac{p^2}{4m^*}(\widehat{P}_{1,1}+\widehat{P}_{1,2}+\widehat{P}_{1,3}+\widehat{P}_{1,4}) + |f(\boldsymbol{p})|(\widehat{P}_{1,3}+\widehat{P}_{1,4}-\widehat{P}_{1,1}-\widehat{P}_{1,2}) \\ &= -E_{1,+}(\widehat{P}_{1,1}+\widehat{P}_{1,2}) - E_{1,-}(\widehat{P}_{1,3}+\widehat{P}_{1,4}). \end{aligned} \tag{C.6}$$

Substitution of this form back into Eq. (C.5) allows us to re-write the Green's function as an eigenvalue expansion:

$$G^{+}_{0,1}(\boldsymbol{p},\omega) = \frac{(\omega - E_{1,+})(\widehat{P}_{1,1} + \widehat{P}_{1,2}) + (\omega - E_{1,-})(\widehat{P}_{1,3} + \widehat{P}_{1,4})}{(\omega - E_{1,-} + i\delta)(\omega - E_{1,+} + i\delta)}$$
$$= \sum_{\lambda} \frac{\widehat{P}_{1,\lambda}}{\omega - E_{1,\lambda} + i\delta}. \tag{C.7}$$

It can also be shown in the same way that the greens function for particle 2 has an analogous form:

$$G^{+}_{0,2}(\boldsymbol{p},\omega) = \sum_{\lambda} \frac{\widehat{P}_{2,\lambda}}{\omega - E_{2,\lambda} + i\delta}, \tag{C.8}$$

as given in the main text.

Appendix D

Some mathematical details of the calculation of the Bethe-Salpeter equation

$$
\begin{aligned}
I &= \frac{i}{2\pi}\int_{-\infty}^{\infty} G_1(\epsilon)G_2(\omega-\epsilon)d\epsilon \\
&= \frac{i}{2\pi}\sum_{\lambda,\lambda'}\widehat{P}_{1,\lambda}\widehat{P}_{2,\lambda'}\int_{-\infty}^{\infty}\frac{d\epsilon}{\left(\epsilon+E_f-E_{1,\lambda}+i\delta_{\lambda}^{(1)}\right)\left(\omega-\epsilon+E_f-E_{2,\lambda'}+i\delta_{\lambda'}^{(2)}\right)} \\
&\equiv \frac{i}{2\pi}\sum_{\lambda,\lambda'}\widehat{P}_{1,\lambda}\widehat{P}_{2,\lambda'}\int_{-\infty}^{\infty}\frac{d\epsilon}{h(\epsilon)},
\end{aligned}
\tag{D.1}
$$

where we have used the Green's functions from Eq. (4.24), suppressed the momentum variables for the time being as a matter of convenience and defined the function

$$
h(\epsilon)=\left(\epsilon+E_f-E_{1,\lambda}+i\delta_{\lambda}^{(1)}\right)\left(\omega-\epsilon+E_f-E_{2,\lambda'}+i\delta_{\lambda'}^{(2)}\right). \tag{D.2}
$$

The integrand has two poles:

$$
\begin{aligned}
\epsilon_1 &= E_{1,\lambda}-E_f-i\delta_{\lambda}^{(1)} \\
\epsilon_2 &= \omega-E_{2,\lambda'}+E_f+i\delta_{\lambda}^{(2)},
\end{aligned}
\tag{D.3}
$$

but because the imaginary part of each is multi-valued (depending on whether the particle is above or below the Fermi level) there are many individual cases to consider. We can immediately reduce the number of cases by a factor of 4 by utilizing the degeneracy of the single-particle energies calculated earlier. This degeneracy leads to many copies of the same case when calculating the integral, so instead of considering the contributions of the poles for $\lambda = \{1, 2, 3, 4\}$ we can instead consider $\lambda = \{+, -\}$, where $+$ and $-$ correspond to upper and lower cones respectively. We need only be careful to associate the correct sign to the correct projection operators when substituting the results back into I. A summary of the remaining cases is given in Table D.1. There are in fact two more cases which we have ignored because they are unphysical: these both correspond one electron being above the Fermi level in the lower cone and the other electron being below the Fermi level in the upper cone (both of these cases are impossible when the Fermi levels of the two layers are equal).

Case	λ	λ'	$E_{1,\lambda}$	$\delta_\lambda^{(1)}$	$E_{2,\lambda'}$	$\delta_{\lambda'}^{(2)}$
1	$+$	$+$	$> E_f$	δ	$> E_f$	δ
2			$< E_f$	$-\delta$	$< E_f$	$-\delta$
3			$> E_f$	δ	$< E_f$	$-\delta$
4			$< E_f$	$-\delta$	$> E_f$	δ
5	$+$	$-$	$> E_f$	δ	$> E_f$	δ
6			$< E_f$	$-\delta$	$< E_f$	$-\delta$
7			$> E_f$	δ	$< E_f$	$-\delta$
8	$-$	$+$	$> E_f$	δ	$> E_f$	δ
9			$< E_f$	$-\delta$	$< E_f$	$-\delta$
10			$< E_f$	$-\delta$	$> E_f$	δ
11	$-$	$-$	$> E_f$	δ	$> E_f$	δ
12			$< E_f$	$-\delta$	$< E_f$	$-\delta$
13			$> E_f$	δ	$< E_f$	$-\delta$
14			$< E_f$	$-\delta$	$> E_f$	δ

Table D.1: List of the relevant cases in the enumeration of states above (δ) and below ($-\delta$) the Fermi level.

We calculate the frequency integral using the calculus of residues:

$$I = -\sum_n \mathrm{Res}\left(\frac{1}{h(\epsilon)|\epsilon_n}\right) W_n = -\sum_n \frac{W_n}{h'(\epsilon_n)} \tag{D.4}$$

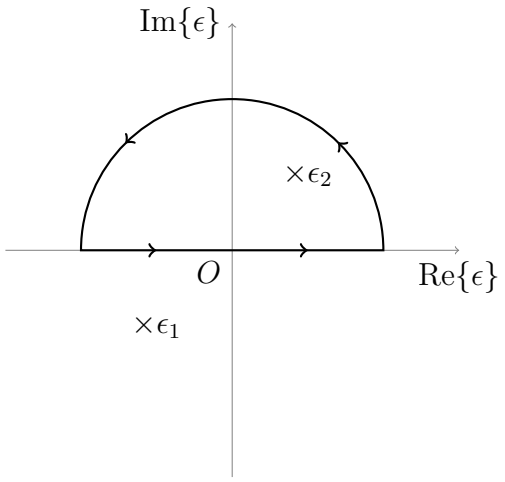

Figure D.1: Example of the contour used for case 1 in Table D.1.

where $n = 1, 2$ enumerates the poles and the winding number $W_n = 1$ (-1) for a pole in a contour traversed counter-clockwise (clockwise). We choose for a contour the semicircle which follows the $\mathrm{Re}(\epsilon)$-axis from $-\infty$ to ∞ and completes with an arc of infinite radius by noting that the integral vanishes over the arc. Notice that in each case at most one residue will be non-zero. For cases $3, 4, 7, 10, 13$ and 14 $\delta^{(1)}$ and $\delta^{(2)}$ have opposite signs and both poles will be in the same half-plane. When this is the case we can always choose to close the contour in the *other* half plane, and the integral vanishes without further analysis. In every other case the poles are on opposite sides of the real line and we choose to close the contour in whichever half-plane is convenient. As only one pole will be inside the contour, there is only ever one residue to calculate for these cases. For the example of case 1, ϵ_2 is in the upper-half plane and ϵ_1 is in the lower-half plane. We choose to close the contour as in Fig. D.1.

The residues for each case are given by:

$$
\begin{aligned}
1 \quad & \mathrm{Res}(\epsilon_2) = \tfrac{-1}{\omega+2E_f-E_{2,+}-E_{1,+}+i\delta} \\
2 \quad & \mathrm{Res}(\epsilon_1) = \tfrac{1}{\omega+2E_f-E_{2,+}-E_{1,+}-i\delta} \\
5 \quad & \mathrm{Res}(\epsilon_2) = \tfrac{-1}{\omega+2E_f-E_{2,-}-E_{1,+}+i\delta} \\
6 \quad & \mathrm{Res}(\epsilon_1) = \tfrac{1}{\omega+2E_f-E_{2,-}-E_{1,+}-i\delta} \\
8 \quad & \mathrm{Res}(\epsilon_2) = \tfrac{-1}{\omega+2E_f-E_{2,+}-E_{1,-}+i\delta} \\
9 \quad & \mathrm{Res}(\epsilon_1) = \tfrac{1}{\omega+2E_f-E_{2,+}-E_{1,-}-i\delta} \\
11 \quad & \mathrm{Res}(\epsilon_2) = \tfrac{-1}{\omega+2E_f-E_{2,-}-E_{1,-}+i\delta} \\
12 \quad & \mathrm{Res}(\epsilon_1) = \tfrac{1}{\omega+2E_f-E_{2,-}-E_{1,-}-i\delta}
\end{aligned}
\tag{D.5}
$$

Each of the cases in Eq. (D.5) can be summarized into the following form:

$$
\frac{-F(E_{1,\lambda}, E_{2,\lambda'})}{\omega + 2E_f - E_{1,\lambda} - E_{2,\lambda'} + iF(E_{1,\lambda}, E_{2,\lambda'})\delta},
\tag{D.6}
$$

where

$$
F(E_{1,\lambda}, E_{2,\lambda'}) = \begin{cases} 1 & E_{1,\lambda}, E_{2,\lambda'} > E_f \\ 0 & E_{1,\lambda} > E_f \geq E_{2,\lambda'} \text{ and } E_{1,\lambda} \leq E_f < E_{2,\lambda'} \\ -1 & E_{1,\lambda}, E_{2,\lambda'} \leq E_f. \end{cases}
\tag{D.7}
$$

This function can be expressed in the simpler form

$$
F(E_{1,\lambda}, E_{2,\lambda'}) = 1 - n_{1,\lambda} - n_{2,\lambda'},
\tag{D.8}
$$

where $n_{1,\lambda}$ and $n_{2,\lambda'}$ are the Fermi-Dirac distributions, e.g.

$$
n_{1,\lambda} = \frac{1}{\exp\left(\frac{E_{1,\lambda}-E_f}{k_b T}\right) + 1},
\tag{D.9}
$$

at zero temperature. We therefore have

$$I = \sum_{\lambda,\lambda'} \frac{\widehat{P}_{1,\lambda}\widehat{P}_{2,\lambda'}(1 - n_{1,\lambda} - n_{2,\lambda'})}{\omega + 2E_f - E_{1,\lambda} - E_{2,\lambda'} + i(1 - n_{1,\lambda} - n_{2,\lambda'})\delta} \tag{D.10}$$

Recall the definition of the Hamiltonian in the tensor product space of two particles:

$$\widehat{H}_1 \equiv \widehat{H}_{\boldsymbol{K}^+,1}(\boldsymbol{p}) \otimes \sigma_{0,2} \tag{D.11}$$

We are free to write the single-particle Hamiltonian as a spectral decomposition over it's eigenstates $\{|i\rangle\} \in \mathcal{H}_1$ which are defined by $\widehat{H}_{\boldsymbol{K}^+,1}|i\rangle = E_{1,i}|i\rangle$:

$$\widehat{H}_{\boldsymbol{K}^+,1} = \sum_i E_{1,i}|i\rangle\langle i|\,. \tag{D.12}$$

In the two-particle space $\mathcal{H} = \mathcal{H}_1 \otimes \mathcal{H}_2$, then, the Hamiltonian of particle 1 becomes

$$\widehat{H}_1 = \sum_i E_{1,i}\left(|i\rangle\langle i| \otimes \sigma_{0,2}\right). \tag{D.13}$$

Now we consider the factorized vector $|j\rangle \otimes |s\rangle \in \mathcal{H}$ where $\{|s\rangle\}$ is an orthonormal basis on $\mathcal{H}_1$. When we choose $j = 1, 2$ and $s \equiv \uparrow, \downarrow$ (i.e. $\{|s\rangle\}$ are just the spin-$\frac{1}{2}$ eigenspinors) we see that these four vectors are simply the eigenvectors of $\widehat{H}_1$ calculated above. In particular:

$$\widehat{P}_{1,\lambda} = \left(|j\rangle \otimes |s\rangle\right)\left(\langle j| \otimes \langle s|\right) = |j\rangle\langle j| \otimes |s\rangle\langle s|\,, \tag{D.14}$$

where it is important to note that we have introduced the placeholder $\lambda \equiv j, s$. This

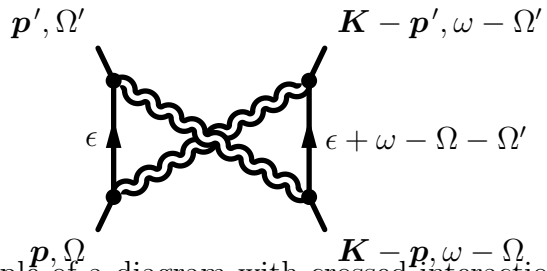

Figure D.2: An example of a diagram with crossed interaction lines. Such diagrams vanish for instantaneous interactions.

gives

$$\begin{aligned}
\widehat{P}_{1,\lambda}\widehat{H}_1 &= \sum_i E_{1,i} \left(|j\rangle \langle j|i\rangle \langle i| \otimes |s\rangle \langle s| \right) \\
&= \sum_i E_{1,i}\delta_{i,j} \left(|j\rangle \langle i| \otimes |s\rangle \langle s| \right) \\
&= E_{1,\lambda}\widehat{P}_{1,\lambda}. \qquad \text{(D.15)}
\end{aligned}$$

By following steps analogous to those above, one can prove the same relationship between the Hamiltonian and projectors for particle 2. It follows that, for a suitably well behaved function of the energies $f(E_{1,\lambda}, E_{2,\lambda'})$, the projectors act as $\widehat{P}_{2,\lambda'} f(E_{1,\lambda}, E_{2,\lambda'}) = \widehat{P}_{2,\lambda'} f(E_{1,\lambda}, \widehat{H}_2)$. We identify Eq. (D.10) as comprising such a function, and simplify:

$$\begin{aligned}
I &= \sum_\lambda \frac{\widehat{P}_{1,\lambda} \sum_{\lambda'} \widehat{P}_{2,\lambda'}(1 - n_{1,\lambda} - \widehat{n}_2)}{\omega + 2E_f - E_{1,\lambda} - \widehat{H}_2 + i(1 - n_{1,\lambda} - \widehat{n}_2)\delta} \\
&= \frac{\sum_\lambda \widehat{P}_{1,\lambda}(1 - \widehat{n}_1 - \widehat{n}_2)}{\omega + 2E_f - \widehat{H}_1 - \widehat{H}_2 + i(1 - \widehat{n}_1 - \widehat{n}_2)\delta} \\
&= \frac{1 - \widehat{n}_1 - \widehat{n}_2}{\omega + 2E_f - \widehat{H}_1 - \widehat{H}_2 + i(1 - \widehat{n}_1 - \widehat{n}_2)\delta}, \qquad \text{(D.16)}
\end{aligned}$$

where we have twice used the resolution of the identity, of Eq. (C.3).

As an aside, one might notice that diagrams of the type in Fig. D.2 which should, in general, appear in expansions of the two-particle propagator are absent from our analysis. In the time domain, such a diagram shows an interaction "leaving" particle 1 and "arriving" at particle 2 some finite time later. Physically it therefore corresponds to a retarded interaction. If the particles do not undergo considerable bare propagation on the time scale of the interaction, one might assume that these diagrams are negligible

This is the case for graphene, in which the Fermi velocity is much smaller than the speed of light ($\frac{v_f}{c} \approx \frac{1}{300}$). For this reason, we are free to assume that the interaction is instantaneous, and therefore frequency independent. Now let us calculate the exact form of Fig. D.2. We proceed as before, but this time integrating over intermediate frequencies gives

$$\frac{i}{2\pi}\int_{-\infty}^{\infty} G_1(\epsilon)G_2(\epsilon+\omega-\Omega-\Omega')d\epsilon, \tag{D.17}$$

the integrand of which has two poles in the complex ϵ-plane:

$$\begin{aligned}\epsilon_1 &= E_{1,\lambda} - E_f - i\delta_{\lambda}^{(1)} \\ \epsilon_2 &= \Omega + \Omega' + E_{2,\lambda'} - E_f - \omega - i\delta_{\lambda'}^{(2)}.\end{aligned} \tag{D.18}$$

For the electron-electron case, when $\delta_{\lambda}^{(1)} = \delta_{\lambda'}^{(2)} = \delta$, the poles are in the same half-plane and the integral vanishes exactly for every value of λ and λ'. We therefore omit all diagrams with crossed interaction lines from our analysis.

Bibliography

[1] J. Sabio, F. Sols, and F. Guinea. Two-body problem in graphene. *Physical Review B*, **81**:045428, 2010.

[2] M. I. Katsnelson. *Graphene: carbon in two dimensions*. Cambridge University Press, Cambdridge, 2012.

[3] P. Y. Bruice. *Organic chemistry*. Pearson, Essex, 2010.

[4] J. D. Bernal. The structure of graphite. *Proceedings of the Royal Society A*, **106**:749, 1924.

[5] O. Hassel and H. Mark. Über die kristallstruktur des graphits. *Zeitschrift für Physik*, **25**:317, 1924.

[6] K. S. Novoselov, D. Jiang, F. Schedin, T. J. Booth, V. V. Khotkevich, S. V. Morozov, and A. K. Geim. Two-dimensional atomic crystals. *Proceedings of the National Academy of Sciences of the United States of America*, **102**:10451, 2005.

[7] A. H. Castro Neto, F. Guinea, N. M. R. Peres, K. S. Novoselov, and A. K. Geim. The electronic properties of graphene. *Reviews of Modern Physics*, **81**:109, 2009.

[8] J.R. Oppenheimer. Note on light quanta and the electromagnetic field. *Physical Review*, **38**:725, 1931.

[9] R. Winkler. *Spin-orbit coupling effects in two-dimensional electron and hole systems*. Springer, New York, 2003.

[10] Y.A. Bychkov and Rashba. Properties of a 2d electron gas with lifted spectral degeneracy. *Journal of Experimental and Theoretical Physics Letters*, **39**:78, 1984.

[11] M.Z. Hasan and C.L. Kane. Colloquium: topological insulators. *Reviews of Modern Physics*, **82**:3045, 2010.

[12] D. Hsieh, D. Qian, L. Wray, Y. Xia, Y.S. Hor, R.J. Cava, and M.Z. Hasan. A topological Dirac insulator in a quantum spin Hall phase. *Nature*, **452**:970, 2008.

[13] S-Y. Xu, I. Belopolski, N. Alidoust, M. Neupane, G. Bian, C. Zhang, R. Sankar, G. Chang, Z. Yuan, C-C. Lee, S-M. Huang, H. Zheng, J. Ma, D.S. Sanchez, B. Wang, A. Bansil, F. Chou, P.P. Shibayev, H. Lin, S. Jia, and M.Z. Hasan. Discovery of Weyl fermion semimetal and topological Fermi arcs. *Science*, **349**:613, 2015.

[14] D. Ciudad. Weyl fermions: massless yet real. *Nature Materials*, **14**:863, 2015.

[15] M. I. Katsnelson, K. S. Novoselov, and A. K. Geim. Chiral tunnelling and the Klein paradox in graphene. *Nature Physics*, **2**:620, 2006.

[16] A. V. Shytov, M. I. Katsnelson, and L. S. Levitov. Atomic collapse and quasi-rydberg states in graphene. *Physical Review Letters*, **99**:246802, 2007.

[17] Y. Wang, D. Wong, A.V. Shytov, V.W. Brar, S. Choi, Q. Wu, H-Z. Tsai, W. Regan, A. Zettl, R.K. Kawakami, S.G. Louie, L.S. Levitov, and M.F. Crommie. Observing atomic collapse resonances in artificial nuclei on graphene. *Science*, **340**:734, 2013.

[18] P.R. Wallace. The band theory of graphite. *Physical Review*, **71**:662, 1947.

[19] N.W. Ashcroft and N.D. Mermin. *Solid state physics*. Thomson Learning, Boston, 1976.

[20] C. Hwang, D. Siegel, S-K. Mo, W. Regan, A. Ismach, Y. Zhang, A. Zettl, and A. Lanzara. Fermi velocity engineering in graphene by substrate modification. *Scientific Reports*, **2**:590, 2012.

[21] J. Avila, I. Razado, S. Lorcy, R. Fleurier, E. Pichonat, D. Vignaud, X. Wallart, and M. Asensio. Exploring electronic structure of one-atom thick polycrystalline graphene films: A nano angle resolved photoemission study. *Scientific Reports*, **3**:2439, 2013.

[22] D.C. Elias, R.V. Gorbachev, A.S. Mayorov, S.V. Morozov, A.A. Zhukov, P. Blake, L.A. Ponomarenko, I.V. Grigorieva, K.S. Novoselov, F. Guinea, and A.K. Geim. Dirac cones reshaped by interaction effects in suspended graphene. *Nature Physics*, **7**:701, 2011.

[23] S. Reich, J. Maultzsch, C. Thomsen, and P. Ordejon. Tight-binding description of graphene. *Physical Review B*, **66**:35412, 2002.

[24] R.S. Deacon, K.-C. Chuang, R.J. Nicholas, K.S. Novoselov, and A.K. Geim. Cyclotron resonance study of the electron and hole velocity in graphene monolayers. *Physical Review B*, **76**:081406, 2007.

[25] A. Kretinin, G.L. Yu, R. Jalil, Y. Cao, F. Withers, A. Mischenko, M.I. Katsnelson, K.S. Novoselov, A.K. Geim, and F. Guinea. Quantum capacitance measurements of electron-hole asymmetry and next-nearest-neighbour hopping in graphene. *Physical Review B*, **88**:165427, 2013.

[26] M. Kühne, C. Faugeras, P. Kossacki, A.A.L. Nicolet, M. Orlita, Y.I. Latyshev, and M. Potemski. Polarization-resolved magneto-Raman scattering of graphenelike domains on natural graphite. *Physical Review B*, **85**:195406, 2012.

[27] R. Winkler and Zülicke. Discrete symmetries of low-dimensional Dirac models: a selective review with a focus on condensed-matter realizations. *Australia and New Zealand Industrial and Applied Mathematics Journal*, **57**:3, 2015.

[28] L. Van Hove. The occurence of singularities in the elastic frequency distribution of a crystal. *Physical Review*, **89**:1189, 1953.

[29] E. McCann, K. Kechedzhi, V.I. Falko, H. Suzuura, T. Ando, and B.L. Altshuler. Weak-localization magnetoresistance and valley symmetry in graphene. *Physical Review Letters*, **97**:146805, 2006.

[30] R.V. Gorbachev, A.K. Geim, M.I. Katsnelson, K.S. Novoselov, T. Tudorovskiy, I.V. Grigorieva, A.H. MacDonald, S.V. Morozov, K. Watanabe, T. Taniguchi, and L.A. Ponomarenko. Strong Coulomb drag and broken symmetry in double-layer graphene. *Nature Physics*, **8**:896, 2012.

[31] H. Min, R. Bistritzer, J. Su, and A.H. MacDonald. Room–temperature superfluidity in graphene bilayers. *Physical Review B*, **78**:121401(R), 2008.

[32] C.-H. Zhang and Y.N. Joglekar. Excitonic condensation of massless fermions in graphene bilayers. *Physical Review B*, **77**:233405, 2008.

[33] D.S.L. Abergel, M. Rodriguez-Vega, E. Rossi, and S. Das Sarma. Interlayer excitonic superfluidity in graphene. *Physical Review B*, **88**:235402, 2013.

[34] S. Kim, I. Jo, J. Nah, Z. Yao, S.K. Banerjee, and E. Tutuc. Coulomb drag of massless fermions in graphene. *Physical Review B*, **83**:161401(R), 2011.

[35] R. N. Lee, A. I. Milstein, and I. S. Terekhov. Quasilocalized states in a model of electron-electron interaction in graphene. *Physical Review B*, **86**:035425, 2012.

[36] M.M. Mahmoodian and M.V. Entin. Moving zero-gap Wannier-Mott excitons in graphene. *Europhysics Letters*, **102**:37012, 2013.

[37] L.L. Marnham and A.V. Shytov. Metastable electron-electron states in double-layer graphene structures. *Physical Review B*, **92**:085409, 2015.

[38] C.A. Downing and M.E. Portnoi. Bielectron vortices in gated graphene. *arXiv:1506.04425*, submitted 2015.

[39] G. Morandi, P. Sodano, A. Tagliacozzo, and V. Tognetti. *Field Theories for Low-Dimensional Condensed Matter Systems*. Springer, New York, 2000.

[40] L.D. Landau and E.M. Lifshitz. *Quantum Mechanics (Non–relativistic Theory)*. Permagon Press, Oxford, 1977.

[41] B. Zaslow and E. Zandler. Two-dimensional analog to the hydrogen atom. *American Journal of Physics*, **35**:1118, 1967.

[42] E.H. Hwang and S. Das Sarma. Dielectric function, screening, and plasmons in two-dimensional graphene. *Physical Review B*, **75**:205418, 2007.

[43] A. K. Geim and K. S. Novoselov. The rise of graphene. *Nature Materials*, **6**:183, 2007.

[44] L. Britnell, R. V. Gorbachev, R. Jalil, B. D. Belle, F. Schedin, M. I. Katsnelson, L. Eaves, S. V. Morozov, A. S. Mayorov, N. M. R. Peres, A. H. Castro Neto, J. Leist, A. K. Geim, L. A. Ponomarenko, and K. S. Novoselov. Electron tunneling through ultrathin boron nitride crystalline barriers. *Nano Letters*, **12**:1707, 2012.

[45] K.I. Bolotin, K.J. Sikes, J. Hone, H.L. Stormer, and P. Kim. Temperature dependent transport in suspended graphene. *Physical Review Letters*, **101**:096802, 2008.

[46] K. Winkler, G. Thalhammer, F. Lang, R. Grimm, J. Hecker Denschlag, A.J. Daley, A. Kantian, H.P. Büchler, and P. Zoller. Repulsively bound atom pairs in an optical lattice. *Nature Letters*, **441**:853, 2006.

[47] E.F. Gross, V.I. Perel, and R.I. Shekhmametev. Inverse hydrogen-like series in optical excitation of light charged particles in a bismuth iodide (BiI_3) crystal. *Journal of Experimental and Theoretical Physics Letters*, **13**:229, 1971.

[48] S.M. Mahajan and A. Thyagaraja. Exact two-body bound states with Coulomb repulsion in a periodic potential. *Journal of Physics A: Mathematical and General*, **39**:L667, 2006.

[49] D. Souza and F. Claro. Paired states of interacting electrons in a two-dimensional lattice. *Physical Review B*, **82**:205437, 2010.

[50] D.L. Huber. Coulomb pairing and photo-double-ionization in benzene and other aromatic molecules. *Physical Review A*, **89**:051403, 2014.

[51] D. Bohm and D. Pines. A collective description of electron interactions. I: Magnetic interactions. *Physical Review*, **82**:625, 1951.

[52] D. Bohm and D. Pines. A collective description of electron interactions. II: Collective vs individual particle aspects of the interactions. *Physical Review*, **85**:338, 1952.

[53] D. Bohm and D. Pines. A collective description of electron interactions. III: Coulomb interactions in a degenerate electron gas. *Physical Review*, **92**:609, 1953.

[54] D. Bohm and D. Pines. A collective description of electron interactions. IV: Electron interactions in metals. *Physical Review*, **92**:626, 1953.

[55] M. Gell-Mann and K.A. Brueckner. Correlation energy of an electron gas at high density. *Physical Review*, **106**:364, 1956.

[56] V.N. Kotov, B. Uchoa, V.M. Pereira, F. Guinea, and A.H. Castro Neto. Electron-electron interactions in graphene: current status and perspectives. *Reviews of Modern Physics*, **84**:1067, 2012.

[57] B. Wunsch, T. Stauber, F. Sols, and F. Guinea. Dynamical polarization of graphene at finite doping. *New Journal of Physics*, **8**:318, 2006.

[58] K.W-K. Shung. Dielectric function and plasmon structure of stage-1 intercalated graphite. *Physical Review B*, **34**:979, 1986.

[59] S. Das Sarma, E.H. Hwang, and W.-K. Tse. Many-body interaction effects in doped and undoped graphene: Fermi liquid versus non-Fermi liquid. *Physical Review B*, **75**:121406, 2007.

[60] R.A. Jishi. *Feynman diagram techniques in condensed matter physics*. Cambridge University Press, Cambridge, 2013.

[61] Badalyan S.M. and F.M. Peeters. Effect of nonhomogeneous dielectric background on the plasmon modes in graphene double-layer structures at finite temperatures. *Physical Review B*, **85**:195444, 2013.

[62] K. Hosono and K. Wakabayashi. Theory of carrier transport in graphene double-layer structure with carrier imbalance. *Japanese Journal of Applied Physics*, **53**:06JD07, 2014.

[63] R.E.V. Profumo, R. Asgari, M. Polini, and A.H. MacDonald. Double-layer graphene and topological insulator thin-film plasmons. *Physical Review B*, **85**:085443, 2012.

[64] R.E.V. Profumo, M. Polini, R. Asgari, R. Fazio, and A.H. MacDonald. Electron-electron interactions in decoupled graphene bilayers. *Physical Review B*, **82**:085443, 2010.

[65] M.Y. Kharitonov and K.B. Efetov. Electron screening and excitonic condensation in double-layer graphene systems. *Physical Review B*, **78**:241401, 2008.

[66] J. Heras. The Galilean limits of Maxwell's equations. *American Journal of Physics*, **78**:1048, 2010.

[67] G. Giuliani and G. Vignale. *Quantum theory of the electron liquid*. Cambridge University Press, Cambridge, 2005.

[68] L.L. Marnham and A.V. Shytov. Bielectrons in the Dirac sea in graphene: the role of many-body effects. *arXiv:1512.02953*, submitted 2015.

[69] D.J. Griffiths. *Introduction to Quantum Mechanics*. Prentice Hall, New Jersey, 2005.

[70] L.N. Cooper. Bound electron pairs in a degenerate Fermi gas. *Physical Review*, **104**:1189, 1956.

[71] A.L. Fetter and J.D. Walecka. *Quantum theory of many-particle systems*. Dover, New York, 1971.

[72] R.D. Mattuck. *A guide to Feynman diagrams in the many-body problem*. Dover, New York, 1967.

[73] A. Kamenev. *Field theory of non-equillibrium systems*. Cambridge University Press, Cambridge, 2011.

[74] G. Stefanucci and R. van Leeuwen. *Nonequilibrium many-body theory of quantum systems*. Cambridge University Press, Cambridge, 2013.

[75] V.N. Kotov, B. Uchoa, and A.H. Castro Neta. Electron-electron interactions in the vacuum polarization of graphene. *Physical Review B*, **78**:035119, 2008.

[76] K.I. Bolotin, K.J. Sikes, Z. Jiang, M. Klima, G. Fudenberg, J. Hone, P. Kim, and H.L. Stormer. Ultrahigh electron mobility in suspended graphene. *Solid State Communications*, **146**:351, 2008.

[77] J.S. Bunch, A.M. van der Zande, S.S. Verbridge, I.W. Frank, D.M. Tanenbaum, J.M. Parpia, H.G. Craighead, and P.L. McEuen. Electromechanical resonators from graphene sheets. *Science*, **315**:490, 2007.

[78] M.M. Fogler, F. Guinea, and M.I. Katsnelson. Pseudomagnetic fields and ballistic transport in a suspended graphene sheet. *Physical Review Letters*, **101**:226804, 2008.

[79] C. Ojeda-Aristizabal, M. Ferrier, S. Guron, and H. Bouchiat. Tuning the proximity effect in a superconductor-graphene- superconductor junction. *Physical Review B*, **79**:165436, 2009.

[80] X. Du, I. Skachko, and E.Y. Andrei. Josephson current and multiple Andreev reflections in graphene SNS junctions. *Physical Review B*, **77**:184507, 2009.

[81] K. Komatsu, C. Li, S. Autier-Laurent, H. Bouchiat, and S. Guron. Superconducting proximity effect in long superconductor/graphene/superconductor junctions: from specular Andreev reflection at zero field to the quantum Hall regime. *Physical Review B*, **86**:115412, 2012.

[82] I.V. Borzenets, Y. Shimazaki, G.F. Jones, M.F. Craciun, S. Russo, M. Yamamoto, and S. Tarucha. High efficiency CVD graphene-lead (Pb) Cooper pair splitter. *Scientific Reports*, **6**:23051, 2016.

[83] D.J. Chadi and M.L. Cohen. Special points in the brillouin zone. *Physical Review B*, **8**:5747, 1973.